DISSERTATION

PRECISION BOUNDS IN LOCALIZATION MICROSCOPY

Submitted by

Maxine X. Varughese

School of Engineering

Department of Electrical and Computer Engineering

In partial fulfillment of the requirements

For the Degree of Doctor of Philosophy

Colorado State University

Fort Collins, Colorado

Summer 2025

Doctoral Committee:

Advisor: Ali Pezeshki
Co-Advisor: Randy Bartels

Edwin Chong
Christopher Peterson

ABSTRACT

This thesis presents two independent studies in theoretical and experimental optical imaging. The first part investigates the theoretical limits and simulation of Single-Pixel Localization Microscopy (SPLM), a computational imaging technique that employs spatio-temporally modulated (STM) illumination to enable sub-diffraction localization with a single-pixel detector. To quantitatively assess the performance of SPLM, we analyze the localization precision limit using the Cramér-Rao Lower Bound (CRLB) under shot-noise-limited conditions. To account for discrepancies between the assumed and actual imaging models —– such as those caused by optical aberrations —– we further introduce the Misspecified Cramér-Rao Bound (MCRB), which quantifies changes in estimation precision limit under model mismatch. These theoretical tools establish performance limits and characterize the robustness of SPLM to experimental imperfections. Following these analyses, we simulate photon detection from fluorescent emitters via Binomial point processes and perform localization on a discrete grid using Fast Iterative Shrinkage-Thresholding Algorithm (FISTA), with further refinement via a BFGS-based line search method, assuming an accurate forward model.

The second part of the thesis reports the experimental development of Quantitative Scattering Microscopy (QSCAT), a label-free phase imaging technique designed for in situ materials characterization. The system employs a digital light processing (DLP) device and LED illumination to project half pupil patterns onto the back aperture of an objective, enabling differential phase contrast imaging. The recorded intensity measurements are inverted to recover the quantitative phase of the sample, providing optical susceptibility information. We demonstrate the utility of QSCAT by measuring the height of chromium features on a USAF resolution target. Additionally, we incorporate a convolutional neural network (CNN) for phase retrieval, representing a novel integration of learning-based reconstruction into scattering-based microscopy.

ACKNOWLEDGEMENTS

I would like to express my deepest gratitude to my advisors, Prof. Ali Pezeshki and Prof. Randy Bartels, for their invaluable guidance, support, and patience throughout my graduate studies. Their insight, rigor, and encouragement have shaped both my research and my development as a researcher.

I am also grateful to my thesis committee — Prof. Edwin Chong and Prof. Christopher Peterson — for their kind support at various stages of this work.

I thank my collaborators, Prof. Jeff Squier, Prof. Olivier Pinaud and Dr. Jeff Field, and colleagues in Bartels' Lab and Sambur's Lab, especially Gabe Murray, Yusef Farrah, Lang Wang, Patrick Stockton, Olivier Bernard, and Juniper Morales, for their technical help, insightful conversations, and the camaraderie that made the research process enjoyable.

Finally, I want to thank my family and friends for their unwavering support and encouragement. Their belief in me kept me grounded and motivated through the challenges of this journey.

DEDICATION

I would like to dedicate this thesis to my husband, Siju, whose patience, encouragement, and belief in me carried me through every step of this journey.

TABLE OF CONTENTS

LIST OF TABLES

LIST OF FIGURES

Chapter 1

Intorduction

The rise of fluorescence microscopy has played a pivotal role in biological and biomedical imaging due to its non-invasive and chemically specific contrast mechanisms. Conventional widefield fluorescence microscopy, however, remains limited by diffraction, yielding a resolution of roughly 230 nm for green light under high numerical aperture (NA) objectives. To access sub-diffraction structural information, a suite of super-resolution (SR) techniques has been developed, including structured illumination microscopy (SIM) [3,4], single-molecule localization microscopy (SMLM) [5–8], and single-pixel or point-scanning approaches like STED [9, 10].

These methods have proven indispensable for many imaging applications, yet they face several practical challenges. Most widefield SR techniques suffer from limited depth of field (DOF), poor performance under scattering conditions, and low temporal resolution due to scanning or sequential acquisition. Moreover, the reliance on pixelated detectors such as CCDs or CMOS arrays introduces constraints on dynamic range, photon throughput, and speed.

In this thesis, we introduce a novel localization microscopy method—Single-Pixel Localization Microscopy (SPLM) that combines spatio-temporally modulated (STM) illumination, inspired by CHIRPT microscopy [11, 12], with single-pixel detection. By modulating the illumination across time and space, SPLM encodes spatial information of sparse emitters into a temporal signal recorded by a fast photodetector. This imaging strategy eliminates the need for spatial scanning or a camera, offering improved acquisition speed, DOF, and robustness to scattering [13, 14]. Critically, SPLM allows for the estimation of 2D or 3D fluorophore positions from compact temporal data streams.

To rigorously evaluate SPLM's performance, we derive the Fisher Information (FI) and the corresponding Cramér–Rao Lower Bound (CRLB) under a Poisson noise model. These metrics provide the theoretical precision limits of unbiased estimators and reveal how illumination design affects localization performance. We compare SPLM's CRLB to those of existing camera-based

SMLM methods, such as multi-plane microscopy (MUM) and engineered PSF approaches. Our analysis shows that SPLM can achieve competitive localization precision across a large imaging volume, especially for sparse samples.

However, the standard CRLB assumes perfect knowledge of the measurement model, an idealization that is often violated in practice due to calibration errors, optical aberrations, or misalignment. To address this issue, we extend our analysis to include the Misspecified Cramér–Rao Bound (MCRB), which accounts for performance degradation under model mismatch. Originally developed under Gaussian noise assumptions [15–20], the MCRB characterizes the estimation error of any estimator that is unbiased with respect to the "pseudo-true" parameters —— those to which the estimator converges when operating on data generated by a misspecified model.

This thesis extends the MCRB framework to a Poisson noise model, which more accurately captures photon-limited optical measurements. We apply the MCRB to both SPLM and SMLM and analyze how localization precision degrades in the presence of mismatched aberration powers. These mismatches represent errors in the point spread function (PSF) for SMLM and in the temporally modulated illumination for SPLM, specifically first- and second-order aberrations. For tractability, we focus on the single-emitter case, since the effects of low-order aberration mismatch are separable across emitters. We show that under realistic aberration magnitudes, the MCRB predicts significant degradation in localization accuracy if such mismatches are ignored.

To quantify this effect, we compute both the MCRB and the mean squared error lower bound (MSELB) for estimators under the mismatched model and compare them to the standard CRLB computed under the true aberrated and the ideal aberration-free models. These comparisons allow us to understand and quantify the precision loss resulting from model mismatch and to establish performance expectations in practical, imperfect systems. The results demonstrate the necessity of including aberration correction in both experimental design and computational modeling when implementing SPLM or SMLM under realistic conditions.

It is important to note that while the notations used in the CRLB and MCRB analyses may differ, these choices are made because each of contribution are mathematically involved and to

preserve internal consistency within each theoretical framework for clarify and convenience. The distinctions reflect differences in statistical assumptions and parameter dependencies, and are intended to clarify derivations and emphasize the underlying structure of each model.

To complement the theoretical analyses, we simulate signal generation in SPLM and implement computationally efficient localization pipeline that incorporates Fourier-domain analysis and gradient-based optimization to extract emitter positions from noisy temporal data. The simulations include cases with and without model mismatch to illustrate the empirical impact of aberrations on localization precision. This approach enables us to assess localization performance under realistic photon budgets. Additionally, we simulate cases with intentionally introduced model mismatches, such as uncorrected optical aberrations, and evaluate their impact on localization accuracy. The results demonstrate the practicality of SPLM for transverse localization and highlight its robustness and scalability, especially when aberration-aware modeling is incorporated.

While fluorescence-based imaging is widely used due to its molecular specificity, it does not capture the full optical response of biological or material samples. Traditional brightfield microscopy, on the other hand, only measures light intensity, providing information primarily about the absorptive characteristics of the specimen. However, many transparent or weakly absorbing samples, such as unstained cells, thin films, or polymers, primarily alter the phase of transmitted light rather than its amplitude. These phase shifts arise from variations in the refractive index or physical thickness and are closely related to the sample's morphology, density, or internal structure. As a result, quantitative phase imaging (QPI) techniques have emerged as powerful tools to visualize scattering contrast and extract label-free structural or compositional information.

In the last part of the thesis, we describe the development and implementation of Quantitative Scattering Contrast Microscopy (QSCAT), a compact and flexible differential phase contrast (DPC) system built around a digital micromirror device (DLP). Unlike traditional DPC systems with fixed-shaped masks, QSCAT uses the DLP to generate arbitrary half-pupil patterns, which are relayed to the objective's back focal plane via a 4f system. The DLP is treated as an array of

spatially incoherent sources, and calibration procedures are developed to ensure accurate mapping of patterns to pupil coordinates.

We briefly describe the QSCAT imaging model and the associated phase retrieval algorithm, which reconstructs quantitative optical path length differences from a small number of intensity measurements. Preliminary experiments using a chrome-on-glass USAF resolution target confirm the accuracy of phase measurements and validate the system's optical calibration. By leveraging programmable pupil-space illumination, QSCAT opens new opportunities for label-free imaging of biological and material samples, particularly in applications where scattering-based contrast is more informative than fluorescence intensity or absorption.

In summary, this thesis contributes two major innovations: (1) the theoretical analysis of SPLM as a novel fluorescence-based localization microscopy method using STM illumination and single-pixel detection; and (2) the implementation of QSCAT for high-precision, label-free phase imaging using DLP-generated pupil masks. These systems provide new tools for both biological and materials imaging with improved speed, precision, and configurability.

Chapter 2

Fisher Information (FI) and Cramér-Rao Lower Bound (CRLB) in Single Pixel Localization Microscopy (SPLM) with Spatio-temporally Modulated (STM) Illumination

2.1 Introduction

This chapter is based on work previously published in the Journal of the Optical Society of America A (JOSA A): "Fisher information and the Cramér–Rao lower bound in single-pixel localization microscopy with spatiotemporally modulated illumination" by Maxine Xiu et al.

Single-pixel imaging is a compelling computational imaging framework in which spatial information is indirectly captured using a single-element detector and structured illumination. This approach offers practical advantages in cost, speed, and data volume, particularly when spatial resolution is encoded through carefully designed illumination patterns. While traditional implementations of single-pixel imaging are generally constrained by the diffraction limit, recent advances have explored its potential for super-resolution, including the precise localization of point emitters.

In this chapter, we investigate the feasibility of a new imaging modality termed Single-Pixel Localization Microscopy (SPLM), which leverages spatio-temporally modulated (STM) structured illumination to enable sub-diffraction localization using a single-pixel detector. The core idea is to exploit the spatial information implicitly encoded in temporally varying illumination patterns to infer emitter locations with high precision. This approach is conceptually motivated by Coherent Holographic Image Reconstruction by Phase Transfer (CHIRPT) microscopy, a single-pixel technique that uses STM patterns to assign distinct temporal signatures to spatial locations within an illumination volume. Fluorescent emitters excited under such modulation schemes emit light that

retains the temporal structure of the excitation, allowing localization through demodulation and model-based inference.

To evaluate the theoretical limits of localization precision in SPLM, we adopt a statistical estimation framework centered around the Fisher Information (FI) and the Cramér-Rao Lower Bound (CRLB). These quantities provide rigorous, quantitative metrics for assessing how experimental design choices —– such as illumination pattern, emitter position, and emitter density —– affect the achievable localization precision. By analyzing the FI and CRLB under shot-noise-limited conditions and various illumination configurations, we establish performance bounds that offer insight into the fundamental capabilities and constraints of SPLM.

In particular, we show that the temporal encoding introduced by STM illumination results in unique features compared to conventional camera-based single-molecule localization microscopy (SMLM). Notably, SPLM achieves relatively uniform localization precision across a large axial range, and in 3D imaging scenarios, the coupling between transverse and axial modulations leads to enhanced information content and improved axial localization precision.

This chapter presents the mathematical formulation of the FI and CRLB for single-emitter localization using SPLM, followed by numerical evaluations of the bound under various experimental parameters. The results demonstrate that SPLM, while fundamentally different from camera-based systems, offers complementary advantages and reveals new opportunities for high-precision, low-data imaging in resource-constrained or volumetrically extended environments.

2.2 Background

This section provides the theoretical background and foundational concepts underlying SPLM with STM illumination, inspired by CHIRPT microscopy. We begin by describing the prototypical experimental setup, in which structured illumination patterns are introduced via a modulator and image-relayed onto the object plane. Unlike methods that require tightly focused beams, the SPLM configuration uses a broader illumination profile, resulting in a significantly extended depth of field

(DOF). This increased DOF is particularly advantageous for volumetric imaging and facilitates the localization of emitters over a larger axial range.

Assuming a Gaussian illumination beam, we derive an analytical expression for the effective DOF in SPLM with STM illumination. This theoretical result serves as a basis for numerical simulations used to evaluate localization performance across the imaging volume.

We then present a detailed derivation of the FI and the corresponding CRLB with a general probabilistic model and for estimating emitter positions in SPLM. One of the central questions addressed in addition to the CRLB analysis is: under what experimental conditions do the location parameters of a single emitter or multiple emitters remain weakly correlated? This condition allows the bound on the error variance of each parameter to be well-approximated by the inverse of the corresponding diagonal element of the Fisher Information Matrix (FIM). To answer this, we examine the Hadamard ratio of the FIM [21, 22] and a geometric measure of information localization derived from the curvature of the FI manifold [23].

2.2.1 Prototypical Experiment Setup

The STM illumination in CHIRPT microscopy is achieved via a rotating modulation disk that is designed such that the local transverse spatial frequencies in the x- or y-dimensions are linearly swept with time [11]. The single spatially modulated illumination beam incident to the disk is then diffracted into multiple beams. The zeroth- and one of the first-order diffracted beams for each modulation x- or y-direction are selected with a Fourier spatial filter in a high magnification 4-f imaging illumination microscope. This illumination imaging system images the two filtered beams into the object region containing fluorphores to be studied. As the beams propagate through the object space, they interfere with each other to create the intensity pattern that excites the fluorescent emitters. The time-varying spatial frequencies diffracted by the modulation mask define the angle between the beams in the focal region. As the modulation disk completes a full rotation, the diffracted beam completes a full scan in the back aperture, and thus, sampling the full NA of the illumination objective, while the undiffracted beam remains centered in the focal region. Conse-

quently, a temporally modulated illumination pattern is created, consisting of unique time-varying projections of spatial frequencies at each location of the object region.

To utilize this STM illumination strategy for LM, we may generalize the generation of the diffracted beams from any modulator, either a spinning modulation disk or an SLM. For two-dimensional SPLM, modulation masks are designed so that the first-order diffracted beams scan from one end of the illumination objective to the other. When using an SLM, a set of temporally modulated binary gratings, as demonstrated in Fig.2.1, will be uploaded to the SLM. For three-dimensional SPLM, the same modulation masks can be used for the second transverse axis with a 90° rotation and a faster temporal modulation rate. When using a SLM, two copies of the same binary gratings that are orthogonal to each other will either be summed for the rotated method or multiplied for the cascaded method. A prototypical experiment setup for SPLM with SLM illumination is shown in Fig. 2.1.

Note that for simulation purposes, we assume that the time for the beam to focus on all the phase masks, which is referred to as the scan time, is exactly the same as the time for the diffracted beam to complete a full scan in the back aperture, which is referred to as the cutoff time, $2\,t_c$. These times will also be referred to as the signal duration. Since the time for the diffracted beam to complete a full scan depends on the objective lens NA, the temporal modulation rate of the phase masks, the maximal spatial frequency on the mask, and the magnification of the optical system while the temporal modulation rate of the phase masks determines the duration for all the phase masks to be scanned through, the highest density of the printed pattern on the mask and the magnification of the optical system must be designed to ensure that the full NA of the illumination objective is spanned. For the purposes of localization, the key parameter scales as the product of the photon emission rate of the fluorophore and the scan time.

2.2.2 Depth of Field (DOF) with Gaussian Beams

The DOF in SPLM with STM illumination is determined by the region where the illumination modulation is non-zero. Due to the fact that the illumination beam is brought to a tight focus in the

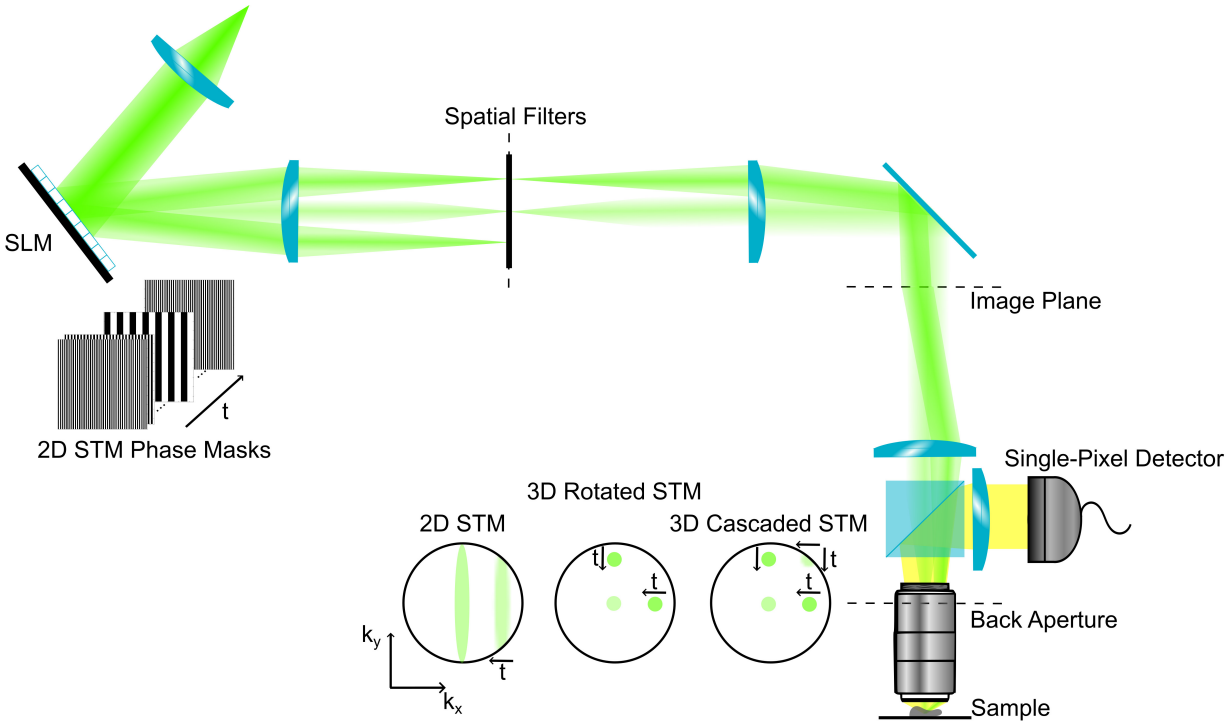

Figure 2.1: Prototypical experiment setup for SPLM with SLM illumination via a SLM. The laser beam is expanded and not so tightly focused onto the SLM, to which a set of temporally modulated binary gratings have been uploaded. The beam is then diffracted into zeroth- and first-order beams. A spatial filter or a set of spatial filters are placed in the Fourier plane conjugated to the back aperture of the objective to filter out one of the first-order diffracted beams. The two beams are then focused onto the sample with a set of lens and an illumination objective with a high numerical aperture (NA). When the detection is set up in the epi direction, the illumination objective will also be the collection objective and a dichroic is needed to filtered out the incident beam so that the fluorescent signal at a different wavelength than the incident can be detected by a single-pixel detector via a tube lens. When using a spinning disk, the beam will be tightly focused onto the disk to generate the same STM illumination patterns in the object region.

Fourier plane and thus, illuminates only a small region of the illumination objective pupil plane after diffraction, the DOF is large.

To see this, we assume that the illumination beam has a Gaussian profile in the transverse plane and is collimated in the axial direction. The incident field with zero center spatial frequencies propagating along the optical axis with Fresnel approximation, normalized by the field spatial maximum, can be expressed as

$$u_0(\vec{\rho}, z) = \frac{E_0(\vec{\rho}, z)}{E_{0,\max}} \approx \frac{M^2\, w_0^2}{M^2\, w_0^2 + i\frac{\lambda_{ex}\, z}{\pi}} \exp\left(i\, k\, z\right) \exp\left(-\frac{\rho^2}{M^2\, w_0^2 + i\frac{\lambda_{ex}\, z}{\pi}}\right), \tag{2.1}$$

where $\overrightarrow{\rho} = x$ in two-dimensional localization while $\overrightarrow{\rho} = (x, y)$ in three-dimensional localization, M is the magnification of the 4f-system from the modulator to the object region, w_0 is the width of the Gaussian distribution, λ_{ex} is the wavelength and $\hbar = 2\,\pi/\lambda_{\text{ex}}$ is the angular wavenumber of the space that the field propagates in. We can further define the propagating incident field with zero center spatial frequencies in terms of its amplitude and phase as

$$\begin{aligned} u_0(\overrightarrow{\rho}, z) \approx \zeta_0(\overrightarrow{\rho}, z)\, e^{i\,\varphi_0(\overrightarrow{\rho}, z)} = \frac{M^2\, w_0^2}{\sqrt{M^4\, w_0^4 + \frac{z^2\, \lambda_{\text{ex}}^2}{\pi^2}}} \exp\left(-\frac{M^2\, w_0^2\, \rho^2}{M^4\, w_0^4 + \frac{z^2\, \lambda_{\text{ex}}^2}{\pi^2}}\right) \\ \times \exp\left(i\,\left(\arctan\left(-\frac{\lambda_{\text{ex}}\, z}{M^2\, w_0^2\, \pi}\right)\right) + \hbar\, z + \frac{\lambda_{\text{ex}}\, \rho^2\, z}{\pi\, M^4\, w_0^4 + \frac{\lambda_{\text{ex}}^2\, z^2}{\pi}}\right). \end{aligned} \tag{2.2}$$

The incident field with shifted center radial spatial frequencies $\overrightarrow{\hbar}_{\perp}(t) = (\hbar_x(t), \hbar_y(t)) = 2\,\pi\ (f_x(t), f_y(t))$, on the other hand, normalized in both time and space can also be written in terms of its amplitude and phase as $u_1(\overrightarrow{\rho}, z, t) = E_1(\overrightarrow{\rho}, z, t)/E_{1,\max} \approx\ \zeta_1(\overrightarrow{\rho}, z, t)\, e^{i\,\varphi_1(\overrightarrow{\rho}, z, t)}$ with its amplitude term expressed as

$$\begin{aligned} \zeta_1(\overrightarrow{\rho}, z, t) = \left|\frac{M\, w_0}{\sqrt{M^2\, w_0^2 + i\,\frac{2\,\hbar_{\perp}^2(t)\, z}{\hbar_z^3(t)}}}\right| \\ \times \exp\left(-\frac{M^2\, w_0^2\, \left|\overrightarrow{\rho} - \overrightarrow{\rho}_s\right|^2 + \frac{4\,\hbar_{\perp}^2(t)\, z^2}{M^2\, w_0^2\, \hbar_z^3(t)}\left|\left(\overrightarrow{\rho} - \overrightarrow{\rho}_s\right)\cdot\left(-\frac{\hbar_y(t)}{\hbar_z^{3/2}(t)}, \frac{\hbar_x(t)}{\hbar_z^{3/2}(t)}\right)\right|^2}{M^4\, w_0^4 + \frac{4\,\hbar_{\perp}^4(t)\, z^2}{\hbar_z^6(t)}}\right), \end{aligned} \tag{2.3}$$

and the phase term can be expressed as

$$\begin{aligned} \varphi_1(\overrightarrow{\rho}, z, t) = \angle\frac{M\, w_0}{\sqrt{M^2\, w_0^2 + i\frac{2\,\hbar_{\perp}^2(t)\, z}{\hbar_z^3(t)}}} + z\left(\hbar_z(t) + \frac{\hbar_{\perp}^2(t)}{\hbar_z(t)} - \frac{\hbar^2\,\hbar_{\perp}^2(t)}{2\,\hbar_z^3(t)}\right) \\ + \frac{\frac{2\,\hbar_{\perp}^2(t)\, z}{\hbar_z^3(t)}\left|\overrightarrow{\rho} - \overrightarrow{\rho}_s\right|^2 - z\left|\left(\overrightarrow{\rho} - \overrightarrow{\rho}_s\right)\cdot\left(-\frac{\hbar_y(t)}{\hbar_z^{3/2}(t)}, \frac{\hbar_x(t)}{\hbar_z^{3/2}(t)}\right)\right|^2}{M^4\, w_0^4 + \frac{4\,\hbar_{\perp}^4(t)\, z^2}{\hbar_z^6(t)}}, \end{aligned} \tag{2.4}$$

where $\hbar_z(t) = \sqrt{\hbar^2 - \hbar_\perp^2(t)}$ denotes the radial spatial frequency along the direction of propagation, which coincides with the first-order Taylor expansion term of the axial spatial frequency in the angular spectral propagator when expanded around $\vec{\hbar}_\perp(t)$, and $\vec{\rho}_s = z\big(- \vec{\hbar}_\perp(t)/\hbar_z(t) + \hbar^2 \vec{\hbar}_\perp(t)/\hbar_z^3(t)\big)$ denotes the shift in propagated beam center that depends on the center transverse spatial frequency.

The DOF is dictated by the overlapping region between the undiffracted and first-order diffracted beams. Thus, solving for the full width at half max (FWHM) of the following envelopes gives the DOF,

$$\Lambda(x, z, t)^{\mathrm{2D}} = \zeta_0(x, z)\, \zeta_{1,x}(x, z, t), \tag{2.5}$$

$$\Lambda(\vec{\rho}, z, t)^{+} = \zeta_0(\vec{\rho}, z)\, \zeta_{1,x}(\vec{\rho}, z, t) \text{ or } \zeta_0(\vec{\rho}, z)\, \zeta_{1,y}(\vec{\rho}, z, t) \tag{2.6}$$

and

$$\Lambda(\vec{\rho}, z, t)^{\times} = \zeta_{1,x}(\vec{\rho}, z, t)\, \zeta_{1,y}(\vec{\rho}, z, t), \tag{2.7}$$

where $\zeta_{1,p}$ denotes the amplitude of the first-order diffracted beam from p-dimension modulation, $p = x, y$, with the center spatial frequency of the first-order beam evaluated at $\vec{f}_\perp(t) = (f_x(t), 0)$ for $p = x$ or $(0, f_y(t))$ for $p = y$.

Note that the amplitude envelope of the SPLM signal varies as a function of time due to the angle of the first-order diffracted beam. Its limiting condition is set by NA when the shift of the spatial frequency is at its maximum, $f_{x,\max} = \mathrm{NA}/\lambda$ in two-dimensional localization and $f_{x,\max} = f_{y,\max} = \mathrm{NA}/\lambda$ in three-dimensional localization. With an excitation wavelength of $500\,\mathrm{nm}$, an illumination objective NA of 1.40 (RI of 1.518), Gaussian width of $56.84\,\mu$m in the object region under a total magnification of 77, the FWHM at the limiting condition is calculated to be approximately $536.6\,\mu$m in two-dimensional localization and three-dimensional localization using the rotated illumination method, and $379.4\,\mu$m using the cascaded illumination method. Note that this is the depth for the full spatial frequency support.

However, the SPLM signal still carries information about emitters outside of the region with full spatial frequency support. The amount of information as compared to the in-focus emitter is

smaller and approximately scaled by the ratio between the illumination pattern intensity envelope evaluated at the emitter position and the origin integrated over time,

$$\Lambda_t(\vec{\rho}, z) = \frac{\int_{-t_c}^{t_c} \Lambda(\vec{\rho}, z, t)dt}{\int_{-t_c}^{t_c} \Lambda(\mathbf{0}, 0, t)dt}. \tag{2.8}$$

Though the center of the localization volume varies slightly with position in the object region, the DOF is approximately the same and thus, can be numerically evaluated along the optical axis, i.e. $x = 0$ in two-dimensional localization and $x = y = 0$ in three-dimensional localization. The DOF, therefore, should be solved by calculating the FWHM of Eq. (2.8) at $\vec{\rho} = \mathbf{0}$. Under the same experimental parameter values as above, the DOF is calculated to be approximately $33.96\,\text{mm}$ regardless of the illumination method in SPLM with SLM illumination.

The interference between two beams also contributes additional phase terms to the SPLM signal, adding some shear to the illumination pattern. These phase terms are time-varying, location-dependent, and can be written with Fresnel approximating as $\varphi_{1,p}(\vec{\rho}, z, t) - \varphi_0(\vec{\rho}, z)$ for modulation along p-dimension, $p = x, y$. with the center spatial frequency of the first-order beam evaluated at $\vec{f}_{\perp}(t) = (f_x(t), 0)$ for $p = x$ or $(0, f_y(t))$ for $p = y$.

2.2.3 General Signal Model

Under CW light excitation, the SPLM signal generated from each fluorescent molecule is treated as a scaled nonlinear function of the excitation illumination. The modulation rate of the spatio-temporal illumination is slow enough so that the excited state population, $e(\boldsymbol{r}, t)$, adiabatically follows the steady-state population that is given by [24],

$$e(\boldsymbol{r}, t) = \frac{I_{\max} I(\boldsymbol{r}, t)}{I_{\text{sat}} + I_{\max} I(\boldsymbol{r}, t)} \equiv \frac{\alpha_{\text{sat}} I(\boldsymbol{r}, t)}{1 + \alpha_{\text{sat}} I(\boldsymbol{r}, t)}. \tag{2.9}$$

We define a peak saturation parameter $\alpha_{\text{sat}} = I_{\max}/I_{\text{sat}}$ that is the ratio of the maximum illumination intensity and the fluorophore saturation intensity, I_{sat}. When α_{sat} is sufficiently small,

the excited state population is approximately linearly proportional to the normalized illumination intensity $I(\boldsymbol{r}, t)$ scaled by α_{sat}. When $\alpha_{\mathrm{sat}} \to \infty$, the excited state population approaches 1.

The SPLM signal intensity at time t is determined by the instantaneous emitted photon flux given by the product of the excited state population $e(\boldsymbol{r}, t)$ and the maximum fluorescence emission rate Γ_0, which is the upper bound of the fluorescence emission rate when $\alpha \to \infty$.

Since LM is concerned with a sparse set of discrete fluorescent objects (e.g., molecules or quantum dots) and we seek to estimate the locations of these individual emitters from the total recorded signal, the expected rate of photons detected from SPLM can be expressed as a continuous function of time,

$$S(t) = \eta_t \, \Gamma_0 \sum_j e(\boldsymbol{r}_j, t) = \eta_r \Gamma_0 \sum_j \frac{\alpha_{\mathrm{sat}} \, I(\boldsymbol{r}_j, t)}{1 + \alpha_{\mathrm{sat}} \, I(\boldsymbol{r}_j, t)}, \tag{2.10}$$

where $\eta_t = \eta_{\mathrm{d}} \, \eta_{\mathrm{op}} \, \eta_{\mathrm{c}}$ is the total detection efficiency of the optical system. Each excited emitter located at $\boldsymbol{r}_j$ is assumed to emit photons at a rate of $\Gamma_0 \, e(\boldsymbol{r}_j, t)$ over the entire 4π solid angle. We will refer to $\phi^j_{\mathrm{em}}(t) = \Gamma_0 \, e(\boldsymbol{r}_j, t)$ as the fluorescent photon emission rate for the j^{th} emitter and $\phi^j_{\mathrm{det}}(t) = \eta_t \, \phi^j_{\mathrm{em}}(t)$ as the fluorescent photon detection rate for the j^{th} emitter. The peak fluorescence emission rate can then be defined as $\phi_{\mathrm{em,peak}} = \Gamma_0 \, \alpha_{\mathrm{sat}}/(1 + \alpha_{\mathrm{sat}})$ while the peak fluorescence detection rate is $\phi_{\mathrm{det,peak}} = \eta_t \, \phi_{\mathrm{em,peak}}$. Note that unlike in a conventional microscope focus, the SPLM illumination peak intensity does not change with NA when the incident power is held fixed. This is because the intensity is set by the relatively large beam size in the object region, which is set by the size of the same beam in the spatial frequency plane (i.e., the pupil plane) of the illumination objective. Thus, for a particular input power, the peak intensity is invariant with respect to the NA of the objective. The caveat is that here we assume that the optical transmission does not change if objectives are changed.

In an experimental data acquisition process, the SPLM signal is measured at a constant sample rate, $1/\Delta t$, to allow for integration, the duration of which is Δt. Thus, the expected rate of photons

detected from SPLM signal at sample time $t_m = m\,\Delta t$ becomes,

$$S[m] = \eta_t\,\Gamma_0 \sum_j e(\boldsymbol{r}_j, t_m) = \eta_t\,\Gamma_0 \sum_j \frac{\alpha_{\rm sat}\,I(\boldsymbol{r}_j, t_m)}{1 + \alpha_{\rm sat}\,I(\boldsymbol{r}_j, t_m)}. \tag{2.11}$$

Considering that the total emitted power from multiple fluorescent molecules is the incoherent sum of the emitted power of each, the expected total number of photoelectrons detected at sample time t_m in SPLM signal is $N_e[m] = \eta_t\,\Gamma_0 \int_{m\,t+\Delta t}^{m\,t-\Delta t} \sum_j e(\boldsymbol{r}_j, \tau) d\tau \approx \eta_t\,\Gamma_0\,\Delta t \sum_j e(\boldsymbol{r}_j, t_m)$. Over a signal duration of $[-t_c, t_c]$, the fluorescence count detected from a single emitter is then bounded from above by $\eta_t\,\mathscr{N}_0 = \eta_t\,(2\,t_c\,\Gamma_0)$ as $\Delta t \to 0$. We will denote this upper bound by $\mathscr{N}_m$.

The total detection efficiency, η_t, is determined by experimental details since the the emitted fluorescent light is collected through a series of optical devices with some objective lens and a detector. We need to take into consideration not only the detection efficiency η_d determined by the responsivity of the detector used but also the throughput efficiency $\eta_{\rm op}$ for all of the optical elements, such as filters and lenses, to account the total power loss. In addition, we account for the collection efficiency determined by the objective lens, $\eta_{\rm c} = \Omega_o/4\pi$, where

$$\Omega_{\rm o} = 2\,\pi \left(1 - \sqrt{1 - (\mathrm{NA}/\mathrm{RI})^2}\right) \tag{2.12}$$

denotes the collection solid angle because only a fraction of the total emitted power from the full 4π solid angle falls onto the detector surface. Here, RI is the refractive index for the medium in which the objective lens is immersed.

For simulation purposes, the detection efficiency, $\eta_{\rm d}$, is set to $40\,\%$ that is typical for a PMT. The loss coefficient for each optical element is $2\,\%$ and with five optical elements in a typical CHIRPT setup, the throughput efficient, $\eta_{\rm op}$, becomes $(98\%)^5$. We assume that the emitted photons are detected at a peak wavelength of $500\,$nm from Atto 488 dye and its maximum fluorescence emission rate, Γ_0, is typically around $200\,/\mu$s according to Table 2.1. For reference, Table 2.1 also lists the maximum fluorescence emission rates, the peak excitation wavelength, and the saturation intensity under peak excitation wavelength of some commonly used fluorophores. Lastly, the

Fluorophore	λ_{ex} **(nm)**	Γ_0 **(/μs)**	I_{sat} **(MW/cm^2)**	$\phi_{\text{em, peak}}$ **(/μs)**	$\phi_{\text{det, peak}}$ **(/μs)**
Atto 488	500	195.12	0.54	126.70	39.62
Atto 532	532	236.84	0.25	153.79	48.09
Atto Rho6G	557	219.51	0.23	142.54	44.57
Rhodamine B	546	184.52	2.35	119.82	37.47
Cy5	651	37.50	2.15	24.35	7.61

Table 2.1: Properties of Some Common Fluorescence Dyes in Water [1, 2]. λ_{ex} denotes the peak excitation wavelength. Γ_0 denotes the maximum fluorescence emission rate. I_{sat} denotes the saturation intensity under the corresponding peak fluorescence excitation wavelength. $\phi_{\text{em,peak}}$ denotes the peak emission rate with an average irrdiance of 1 MW/cm^2 from the laser or $\alpha_{\text{sat}} = 1.85$. $\phi_{\text{det,peak}}$ denotes the corresponding peak fluorescence detection rate with an objective lens NA of 1.40.

collection efficiency, η_{c}, ranges from 6.70% to 34.39% with a dry objective lens of a NA from 0.50 to 0.95 and $\text{RI} = 1.00$, from 10.06% to 28.44% with a water immersion objective lens of a NA from 0.80 to 1.20 and $\text{RI} = 1.33$, and from 13.17% to 30.67% with an oil immersion objective lens of a NA from 1.00 to 1.40 and $\text{RI} = 1.518$.

Illumination Pattern for Two-dimensional Localization

Two-dimensional (x-z) localization in SPLM is achieved by focusing the illumination beam to a line, which extends to a light sheet illumination exactly like CHIRPT microscopy [11–13, 25–27], on a modulation disk or a spatial light modulator (SLM). Since the modulated illumination does not extend along the y-dimension, there is no localization out of the $x-z$ plane. The sheet illumination, on the other hand, lights up a large DOF due to the use of subaperture at the illumination objective pupil plane.

Following the general SPLM signal model, the expected rate of photons detected from SPLM signal at time t is determined by the steady-state population, which is characterized mainly by

the illumination intensity dependent on the technique employed to modulate spatial frequencies. When using a CHIRPT mask, the illumination pattern for the j^{th} emitter at location $\boldsymbol{r}_j = (x_j, z_j)$ is mathematically formulated, assuming no aberrations, as

$$\begin{aligned} I_{\text{2D}}(\boldsymbol{r}_j, t) = a_0^2\, \zeta_0(\boldsymbol{r}_j) + a_1^2\, \mu^2(t)\, \zeta_{1,x}(\boldsymbol{r}_j, t) \\ + 2\, a_0\, a_1\, \mu(t)\, \zeta_0(\boldsymbol{r}_j)\, \zeta_{1,x}(\boldsymbol{r}_j, t) \cos\left(\Delta\Phi_x(\boldsymbol{r}_j, t) + \varphi_{1,x}(\boldsymbol{r}_j, t) - \varphi_0(\boldsymbol{r}_j)\right). \end{aligned} \tag{2.13}$$

Note that a_0 and a_1 are normalized real coefficients so that the maximum intensity of the illumination pattern is 1 over time and space, $\mu(t) \leq 1$ is a real-valued function describing the apodization of energy within a full sweep of the projected spatial frequencies due to the extended beam in y-dimension, and ν_c denotes the modulation carrier frequency. For simplicity, we denote the phase term inside the cosine function as $\Delta\Phi_p(\boldsymbol{r}_j, t)$ for the j^{th} emitter induced by the spatial frequency modulation along p-dimension (e.g. $p = x$ for two-dimensional SPLM). It can be written as

$$\Delta\Phi_p(\boldsymbol{r}_j, t) = 2\,\pi\left(\nu_{c,p}\, t + f_p(t)\, p_j + f_{z,p}(t)\, z_j\right), \tag{2.14}$$

where $f_p(t)$ and $f_{z,p}(t)$ are the time-varying spatial frequencies along the p- and z-axis. These spatial frequencies are proportional to the illumination wavelength and the illumination objective NA as $f_x(t) = (\text{NA}\, t)\,/(\lambda_{\text{ex}}\, t_c)$ and $f_{z,x}(t) = \sqrt{(n/\lambda_{\text{ex}})^2 - (f_x(t))^2} - n/\lambda_{\text{ex}}$ [11], where t_c denotes half of the SPLM signal duration. When specifying a Gaussian model for the excitation beam profile, ζ_0 and $\zeta_{1,p}$ describe the spatial variations in amplitudes for the zeroth- and first-order diffracted beams along the p-dimension, which are normalized so that $|\max(\zeta_0, \zeta_{1,p})| = 1$ over space and time. In two-dimensional CHIRPT illumination, the Gaussian distribution is assumed to be one-dimensional along the x-axis. Following this assumption, the interference illumination pattern results from Gaussian distributions that are centered about $(0, 0)$ and $(f_x(t), 0)$ with their amplitude functions, ζ_0 and $\zeta_{1,x}$, which consequently determine the DOF. In addition to the amplitude functions, there is a location-dependent time-varying phase term, $\varphi_{1,p}(\boldsymbol{r}_j, t) - \varphi_0(\boldsymbol{r}_j)$, under the excitation of a Gaussian beam.

Illumination Pattern for Three-dimensional Localization

Three-dimensional localization in SPLM can be achieved by modulating the excitation beam along two orthogonal axes that are then combined incoherently or sequentially. These STM illumination patterns are inspired by CHIRPT microscopy.

The first method uses the incoherent combination of the modulated waves. Hence, the illumination pattern is an incoherent sum of two two-dimensional modulation patterns expanded to three-dimension, rather than a light sheet focused to a line [28]. In order to distinguish between the two axes, the system is designed to scan at distinct modulation rates along the orthogonal modulation axes. Thus, the aberration-free excitation illumination for the j^{th} emitter when using a CHIRPT mask via this rotated method can be expressed as a sum,

$$\begin{aligned} I^{+}_{\text{3D}}(\boldsymbol{r}_j, t) = 2\, a_0^2\, \zeta_0^2(\boldsymbol{r}_j) + {a_1}^2\, \left(\zeta^2_{1,x}(\boldsymbol{r}_j, t) + \zeta^2_{1,y}(\boldsymbol{r}_j, t)\right) \\ +2\, a_0\, a_1\, \zeta_0(\boldsymbol{r}_j)\, \zeta_{1,x}(\boldsymbol{r}_j, t)\, \cos\left(\Delta\Phi^{+}_x(\boldsymbol{r}_j, t) + \varphi_{1,x}(\boldsymbol{r}_j, t) - \varphi_0(\boldsymbol{r}_j)\right) \\ + 2\, a_0\, a_1\, \zeta_0(\boldsymbol{r}_j)\, \zeta_{1,y}(\boldsymbol{r}_j, t) \cos\left(\Delta\Phi^{+}_y(\boldsymbol{r}_j, t) + \varphi_{1,y}(\boldsymbol{r}_j, t) - \varphi_0(\boldsymbol{r}_j)\right). \end{aligned} \tag{2.15}$$

We have arrived at this form by assuming that the coefficients a_0 and a_1 are identical for modulation along x and y directions. Such approximation is based on the assumption that the interference illumination results from small two-dimensional normal or Gaussian-like distributions centered about $(0, 0)$ and $(f_x(t), 0)$ from the spatial frequency modulation along x-dimension or $(0, f_y(t))$ from the spatial frequency modulation along y-dimension.

The phase terms $\Delta\Phi^{+}_x(\boldsymbol{r}_j, t)$ and $\Delta\Phi^{+}_y(\boldsymbol{r}_j, t)$ take similar forms as Eq. (2.14), with an unique temporal carrier frequency and a unique temporal spatial frequency modulation rate for each modulation direction via shifts in the focused beams away from the center of the modulator. In addition, the modulation is designed such that one complete sweep of spatial frequencies along y-direction is k times faster than that along x-direction, i.e. $\Delta\phi^{+}_y(\boldsymbol{r}_j y, t) = 2\,\pi\,(\nu_{c,y}\, t + f_y(t)\, y_j + f_{z.y}(t)\, z_j) \circledast \text{III}(t/T_y)$, where T_y is $1/k$-th of that along x-direction. An illustration of the three-dimensional STM illumination in the object region using this method at different times is shown in Fig. 2.2.

The second method uses the product of two modulations patterns along the x and y directions. Instead of passing two separate beams through the same modulator as in the rotated incoherent sum method described above, here the beam is first modulated along the x-direction, then along the y direction, so that the modulation pattern is cascaded [29]. The SPLM excitation illumination can then be expressed as a product of the two two-dimensional modulation patterns. When using CHIRPT masks, the aberration-free excitation illumination for the j^{th} emitter via this cascaded

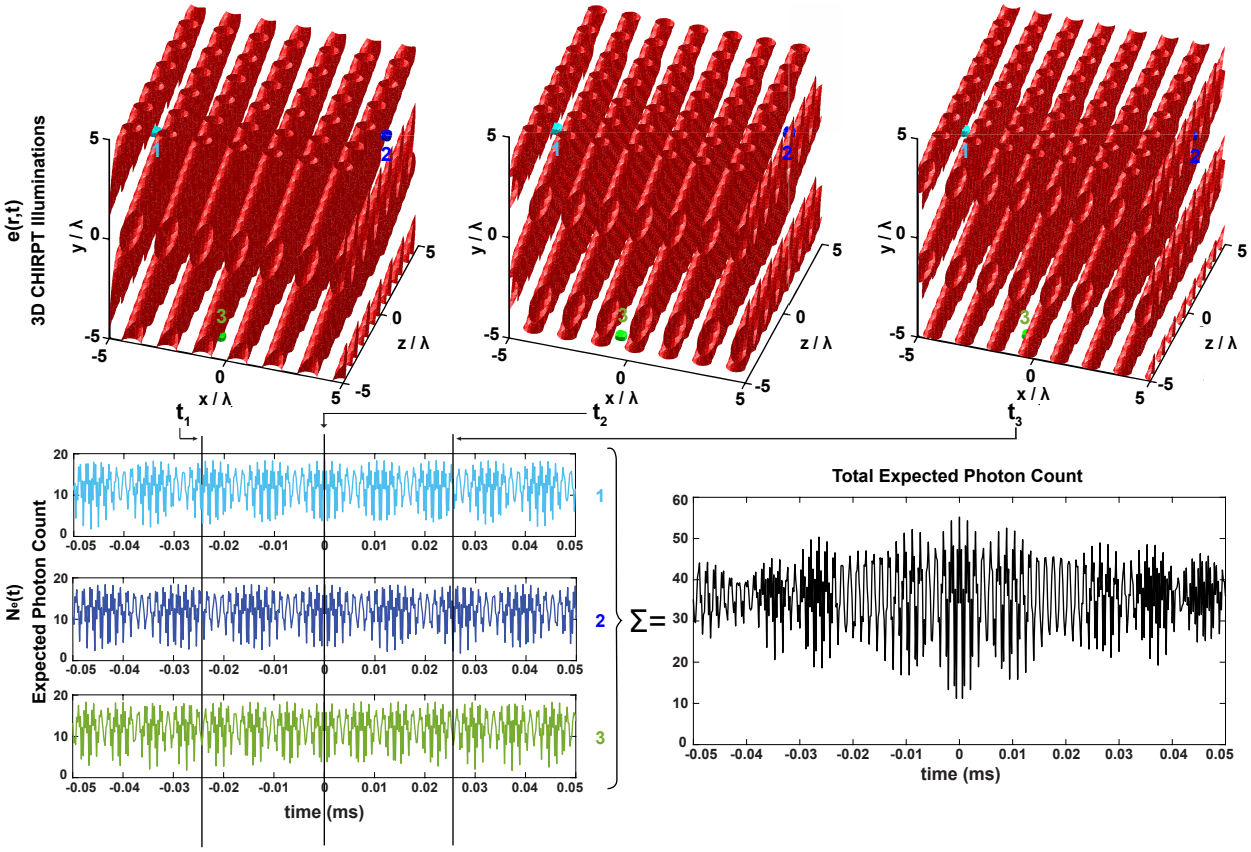

Figure 2.2: Illustrations of the 3D STM illumination in the object region using the rotated method at three different times and the generation of SPLM signal at three different locations. As the diffracted beam scans across the aperture, a STM illumination pattern is created such that the SPLM signal generated from such illumination has a different temporal profile at different locations, which can be used for localization.

method can be expressed as a product,

$$
\begin{aligned}
I^{\times}_{\mathrm{3D}}(\boldsymbol{r}_j,t) = \Bigg(& a_0^2\,\zeta_0^2(\boldsymbol{r}_j) + a_1^2\,\zeta_{1,x}^2(\boldsymbol{r}_j,t) \\
& + 2\,a_0\,a_1\,\zeta_0(\boldsymbol{r}_j)\,\zeta_{1,x}(\boldsymbol{r}_j,t)\,\cos\left(\Delta\Phi_x^{\times}(\boldsymbol{r}_j,t) + \varphi_{1,x}(\boldsymbol{r}_j,t) - \varphi_0(\boldsymbol{r}_j)\right)\Bigg) \\
\times \Bigg(& a_0^2\,\zeta_0^2(\boldsymbol{r}_j) + a_1^2\zeta_{1,y}^2(\boldsymbol{r}_j,t) \\
& + 2\,a_0\,a_1\,\zeta_0(\boldsymbol{r}_j)\,\zeta_{1,y}(\boldsymbol{r}_j,t)\,\cos\left(\Delta\Phi_y^{\times}(\boldsymbol{r}_j,t) + \varphi_{1,y}(\boldsymbol{r}_j,t) - \varphi_0(\boldsymbol{r}_j)\right)\Bigg),
\end{aligned}
\tag{2.16}
$$

where $\Delta\Phi_x^{\times}(\boldsymbol{r}_j,t)$ is the same STM phase along x-axis as the two-dimensional case and $\Delta\Phi_y^{\times}(\boldsymbol{r}_j,t)$ is the same STM phase along y-axis as the rotated method with a carrier frequency centered on the modulator. As the illumination beam propagates through both modulators, the information about the two transverse $x-y$ axes is coupled.

It is important to point out that the cascaded method can be implemented with a single modulator to avoid additional distortions in measured signal. A mask for each modulation axis will be printed on or uploaded to a different region of the modulator for the illumination beam to focus to. The mask for y-direction modulation will be repeated k times for a faster carrier frequency and spatial frequency modulation rate.

Regardless of the illumination patterns, the DOF in three-dimensional SPLM with STM illumination is dictated by the overlapping area between the two first-order diffracted beams instead of the zeroth- and first-order beams as in the two-dimensional case. The spatial frequencies along each transverse direction extends along the axial direction due to diffraction of the spatially coherent modulated beams. In comparison, camera-based SMLM in 3D requires a modified point spread function (PSF) that breaks the axial symmetry [30], such as an astigmatic focus [31, 32], simultaneous imaging of multiple planes [33, 34], or an engineered PSF that rotates with variation in emitter depth (helical, etc.) [35–38], for the widefield imaging system to increase the depth discrimination. These methods are still limited in their imaging DOF because they use the full transverse spatial frequency support of the imaging objective lens for each measurement.

2.2.4 General Formulation of FI and CRLB

Consider that there are multiple parameters to be estimated, for example, the location coordinates for multiple fluorescent molecules. The gradient of the log-likelihood function with respect to the parameters to be estimated, which is also referred to as the Fisher Score, indicates the sensitivity to infinitesimal changes to the parameter values. With any given distribution, $\mathrm{P}(\cdot;\boldsymbol{\theta})$ with Y being a random variable or $\boldsymbol{Y}$ being a random vector, its Fisher Score is defined as

$$\boldsymbol{v}(\cdot;\boldsymbol{\theta}) = \nabla_{\boldsymbol{\theta}}\ell(\cdot;\boldsymbol{\theta}) = \begin{bmatrix} \dfrac{\partial}{\partial\theta_1}\ell(Y;\boldsymbol{\theta}) \\ \vdots \\ \dfrac{\partial}{\partial\theta_N}\ell(Y;\boldsymbol{\theta}) \end{bmatrix} \text{ or } \begin{bmatrix} \dfrac{\partial}{\partial\theta_1}\ell(\boldsymbol{Y};\boldsymbol{\theta}) \\ \vdots \\ \dfrac{\partial}{\partial\theta_N}\ell(\boldsymbol{Y};\boldsymbol{\theta}) \end{bmatrix}, \tag{2.17}$$

where $\ell(\cdot;\boldsymbol{\theta})$ denotes the log of $P(\cdot;\boldsymbol{\theta})$ and θ_i denotes the i^{th} parameter to be estimated.

Note that the expected value of Fisher Score is always zero when some regularity conditions are met. These conditions may include the likelihood function being continuously differential if its support over the measured data is infinite and the integral of the likelihood function with respect to the measured data converges uniformly for all values of parameters to be estimated.

With zero expected value vector, the covariance of Fisher Score, which is also referred to as the FI, is then $\boldsymbol{J}(\cdot;\boldsymbol{\theta}) = \mathrm{E}\left[\boldsymbol{v}(\cdot;\boldsymbol{\theta})\,\boldsymbol{v}^T(\cdot;\boldsymbol{\theta})\right]$, where the expectation is taken with respect to the random variable Y or the random vector $\boldsymbol{Y}$. With multiple parameters to be estimated, the FI is a matrix and thus, we can write the ij^{th} element of the FIM as

$$[\boldsymbol{J}(Y;\boldsymbol{\theta})]_{ij} = \sum_{y=-\infty}^{\infty} \mathrm{P}(Y=y;\boldsymbol{\theta})\,\frac{\partial}{\partial\theta_i}\ell(Y=y;\boldsymbol{\theta})\,\frac{\partial}{\partial\theta_j}\ell(Y=y;\boldsymbol{\theta}), \tag{2.18}$$

or with a random vector,

$$[\boldsymbol{J}(\boldsymbol{Y};\boldsymbol{\theta})]_{ij} = \sum_{m=-M}^{M}\sum_{y_m=-\infty}^{\infty} \mathrm{P}(Y_m=y_m;\boldsymbol{\theta})\,\frac{\partial}{\partial\theta_i}\ell(Y_m=y_m;\boldsymbol{\theta})\,\frac{\partial}{\partial\theta_j}\ell(Y_m=y_m;\boldsymbol{\theta}) \tag{2.19}$$

when the given distribution is discrete. When the given distribution is continuous, the summation simply becomes an integration.

Let $\hat{\theta}_i$ be an unbiased estimator of θ_i, the i^{th} parameter to be estimated. The CRLB states that the error variance of $\hat{\theta}_i$ from its true value θ_i is bounded by the i^{th} diagonal element in the inverse of the FI as

$$\text{var}(\hat{\theta}_i) \geq \left[\boldsymbol{J}^{-1}(Y;\boldsymbol{\theta})\right]_{ii} \text{ or } \left[\boldsymbol{J}^{-1}(\boldsymbol{Y};\boldsymbol{\theta})\right]_{ii}. \tag{2.20}$$

Therefore, the lower bound on the error standard deviation (LBEStd) for an unbiased estimator $\hat{\theta}_i$ of the i^{th} parameter of interest is $\sqrt{\left[\boldsymbol{J}^{-1}(Y;\boldsymbol{\theta})\right]_{ii}}$ or $\sqrt{\left[\boldsymbol{J}^{-1}(\boldsymbol{Y};\boldsymbol{\theta})\right]_{ii}}$.

2.2.5 Background-free Poisson Measurement Model

To quantify the capability of SPLM with STM illumination via CRLB, we first need to understand the randomness in the data and how the values of the parameters to be estimated affect the distribution of the measured data. We assume that the measurement of SPLM signal in photon counts is shot-noise-limited as other noises produced by electronic devices in detection and digitization are considered negligible.

The number of photons in the SPLM experiment can be considered as an observable random variable, Y, which is Poisson distributed given when the photons are detected. The parameters of interest here, denoted by $\boldsymbol{\theta}$, are the location coordinates of the tagged fluorescent molecules, which are considered as point emitters, to be localized. The rate of the Poisson distribution equals to the total photon count expected to be detected, i.e. $Y \mid \boldsymbol{T} \sim \text{Poisson}\left(\int_{-t_c}^{t_c} S_{\boldsymbol{\theta}}(t)dt\right)$, where $\boldsymbol{T}$ denotes the times when photons are detected and is assumed to be uniformly distributed over the range characterized by the photon emission rate function, $[S_{\boldsymbol{\theta}}(-t_c), S_{\boldsymbol{\theta}}(t_c]$. This is under the assumption that no background noise is detected.

Consider that the actual number of photons detected by the single-pixel detector is y. Under the assumption of a continuous measurement, it is almost surely that the arrival time of each photon is distinct from each other. Thus, following the Poisson process that describes the emission of each photon, the joint probability of y photons detected at time $\{t_1, \cdots, t_y\}$ is a product of

individual Poisson distributions as $P(\boldsymbol{Y} = y, \boldsymbol{T} = \{t_1, \cdots, t_y\}; \boldsymbol{\theta}) = \exp\left(-\int_{-t_c}^{t_c} S_{\boldsymbol{\theta}}(t)dt\right)/y! \times \prod_{k=1}^{y} \int_{t_{k-}}^{t_k} S_{\boldsymbol{\theta}}(t)\, dt$, where $[t_{k-}, t_k]$ denotes the duration between when the last and current photon are detected.

To determine the FI of an observable random variable, the natural logarithm of the likelihood function, which is known as the log-likelihood function, is often used for the convenience of computation [39]. The log-likelihood function of y photons detected is simply

$$\ell(Y = y, \boldsymbol{T} = \{t_1, \cdots, t_y\}; \boldsymbol{\theta}) = \int_{-t_c}^{t_c} S_{\boldsymbol{\theta}}(t)dt - \ln y! + \sum_{k=1}^{y} \ln\left(\int_{t_{k-}}^{t_k} S_{\boldsymbol{\theta}}(t)\, dt\right). \tag{2.21}$$

In the discrete-time case, assume that there are $2\,M$ samples taken over the SPLM signal duration with uniform sampling such that $\Delta t = t_c/M$. The number of photons detected at each measurement then becomes an element of the random vector, $\boldsymbol{Y} = [Y_{-M}, \cdots, Y_M]^T$, that is independent and identically distributed. At any m-th sample, the random variable Y_m is Poisson distributed with a rate equals to the expected detected photon count within the integration interval, i.e. $Y_m \sim$Poisson$(\Delta t\, S_{\boldsymbol{\theta}}[m])$. Similar to the continuous-time model, the probability when each photon is detected also needs to be accounted for and it is indeed taken into consideration through the i.i.d. Poisson distributions with different rates in the discrete-time model. Thus, the joint probability of a sequence of photon counts, $\{y_{-M}, \cdots, y_M\}$, detected at their corresponding intervals is P$(\boldsymbol{Y} = \{y_{-M}, \cdots, y_M\}; \boldsymbol{\theta}) = \exp\left(-\sum_{m=-M}^{M} \Delta t\, S_{\boldsymbol{\theta}}[m]\right) \prod_{m=-M}^{M} (\Delta t\, S_{\boldsymbol{\theta}}[m])^{y_m}/y_m!$.

The discrete-time likelihood converges to that of the continuous-time when $\Delta t \to 0$ and $S_{\boldsymbol{\theta}}[n] \to S_{\boldsymbol{\theta}}(t)$. The log-likelihood for the discrete-time model is then

$$\ell(\boldsymbol{Y} = \{y_{-M}, \cdots, y_M\}; \boldsymbol{\theta}) = \sum_{m=-M}^{M} \left(-\Delta t\, S_{\boldsymbol{\theta}}[m] - \ln(y_m!) + y_m \ln(\Delta t\, S_{\boldsymbol{\theta}}[m])\right). \tag{2.22}$$

The probabilities above describe the relative likelihood of a particular set of values for the location coordinates of the fluorescent emitters given that the random variable Y or random vector $\boldsymbol{Y}$ is realized by the measurement y or $\{y_{-M}, \cdots, y_M\}$. That is to say given a particular sequence of photon counts detected, the probability varies with respect to the emitter locations, $\boldsymbol{\theta}$. Thus,

the notation $\mathrm{P}(\cdot;\boldsymbol{\theta})$ indicates that our interest is to measure the goodness of a fit for the detected photon count to $\boldsymbol{\theta}$ and is oftentimes referred to as the likelihood function.

The likelihood functions establish mathematical descriptions from which the parameters of interest can be estimated. The parameter set that yields the maximum likelihood given the data collected is believed to be the best choice and such set is called the maximum likelihood estimate. Other statistics derived from the log-likelihood functions are introduced in the next section to reveal different information characterizing a given model.

2.2.6 Detailed FI Derivation

FI indicates how well a parameter can be estimated in terms of how distinguishable the FI value is in relative to changes in the parameter. The greater the variation of FI with respect to a relatively small amount of change in the parameter, the better the lower bound on error variance for estimating such a parameter.

Mathematically, the FI is defined as the curvature of the log-likelihood function, or the covariance of the Fisher score, which reveals the sensitivity in a given random process to the infinitesimal changes of parameter values. Following the derivation of FI with its ij^{th} element expressed as (2.18) or (2.19) with the expectation now taken with respect to two random variables, the number of photons detected Y or $\boldsymbol{Y}$ as well as the times when photons are detected $\boldsymbol{T}$, and the log-likelihood functions given by (2.21) or (2.22), the ij^{th} element of the FIM can then be written as

$$[\boldsymbol{J}[Y;\boldsymbol{\theta}]]_{ij} = \int_{-t_c}^{t_c} \frac{1}{S_{\boldsymbol{\theta}}(t)} \frac{\partial}{\partial \theta_u} S_{\boldsymbol{\theta}}(t) \frac{\partial}{\partial \theta_v} S_{\boldsymbol{\theta}}(t) dt, \tag{2.23}$$

and in the discrete-time case,

$$[\boldsymbol{J}(\boldsymbol{Y};\boldsymbol{\theta})]_{ij} = \sum_{m=-M}^{M} \frac{\Delta t}{S_{\boldsymbol{\theta}}[m]} \frac{\partial}{\partial \theta_u} S_{\boldsymbol{\theta}}[m] \frac{\partial}{\partial \theta_v} S_{\boldsymbol{\theta}}[m]. \tag{2.24}$$

As $\Delta t \to 0$, $[\boldsymbol{J}(\boldsymbol{Y};\boldsymbol{\theta})]_{ij} \to [\boldsymbol{J}[Y;\boldsymbol{\theta}]]_{ij}$ $(\forall)$ i, j. Note that the indexes i and j correspond to the indexes $n\ (l-1)+u$ and $n\ (s-1)+v$ respectively for the location parameter along u^{th}

direction for the l emitter and the location parameter along v^{th} direction for the s^{th} emitter in the n-dimensional localization.

To see how the total number of photons detected from SPLM signal effects the localization precision more clearly, we consider each FI element as a function of SPLM signal with its intensity normalized to unity multiplied by the upper bound of the fluorescence count detected from a single emitter over the measured SPLM signal duration,

$$[\boldsymbol{J}(\boldsymbol{Y};\boldsymbol{\theta})]_{ij} = \frac{\mathscr{N}_m}{2}\,\overline{J}_{uv} = \frac{\mathscr{N}_m}{2}\int_{-1}^{1}\frac{1}{\overline{S}_{\boldsymbol{\theta}}(\tau)}\frac{\partial}{\partial\theta_i}\overline{S}_{\boldsymbol{\theta}}(\tau)\frac{\partial}{\partial\theta_j}\overline{S}_{\boldsymbol{\theta}}(\tau)d\tau, \tag{2.25}$$

where $\mathscr{N}_m = \eta_t\,\mathscr{N}_0 = \eta_t\,(2\,t_c\,\Gamma_0)$ denotes the upper bound of the fluorescence count detected from a single emitter, $\overline{J}_{ij}$ denotes the ij-th element of the normalized FI by $\mathscr{N}_m$ with respect to the normalized time variable $\tau = t/t_c$ so that the FI elements remain proportional to the maximal spatial frequency projected, and $\overline{S}_{\boldsymbol{\theta}}$ denotes the SPLM signal normalized by the product of the total detection efficiency η_t and the maximum fluorescence emission rate Γ_0. In the discrete-time model, the same normalization applies to the summation over $2\,M$ samples and the normalized time variable τ becomes $m\,\Delta\tau = m\,\Delta t/t_c$ at m-th sample. Thus, the ij^{th} element of the FI in the discrete-time model can be written as

$$[\boldsymbol{J}(\boldsymbol{Y};\boldsymbol{\theta})]_{ij} = \frac{\mathscr{N}_m}{2}\sum_{m=-M}^{M}\frac{\Delta\tau}{\overline{S}_{\boldsymbol{\theta}}[m]}\frac{\partial}{\partial\theta_i}\overline{S}_{\boldsymbol{\theta}}[m]\frac{\partial}{\partial\theta_j}\overline{S}_{\boldsymbol{\theta}}[m]. \tag{2.26}$$

Note that the value of each FI element depends on the sensitivities of the measured data about the corresponding parameters of interest, which is quantified by the partial derivative of the SPLM signal with respect to the location parameters that is dependent on the technique employed to modulate spatial frequencies. Its generalized expression for any transverse coordinate of the l^{th} emitter is given by

$$\begin{aligned}\frac{\partial}{\partial q_l}\overline{S}_{\boldsymbol{\theta}}(\tau) = -\frac{4\,\pi\,a_0\,a_1\,\mu(\tau)\,\zeta_0(\boldsymbol{r}_l)\,\zeta_{1,x}(\boldsymbol{r}_l,\tau)\,f_q(\tau)\,\alpha_{\text{sat}}\,K_{q^c}(\tau)}{\left(1+\alpha_{\text{sat}}\,I(\boldsymbol{r}_l,\tau)\right)^2}\\ \times\sin\left(\Delta\Phi_q(\boldsymbol{r}_l,\tau)+\varphi_{1,q}(\boldsymbol{r}_l,\tau)-\varphi_0(\boldsymbol{r}_l)\right),\end{aligned} \tag{2.27}$$

where q^c denotes the compliment transverse coordinate direction, i.e. if $q = x$, then $q^c = y$ and vice versa, and K_{p^c} is the coefficient function describing this information coupling between the transverse axes. With 2D and 3D rotated illumination methods, $K_{p^c}^{+} = 1$ as the transverse information is uncoupled. With 3D cascaded illumination method, $K_{p^c}^{\times}(\tau) = a_0^2 + a_1^2 + 2\, a_0\, a_1\, \cos\left[\Delta\Phi_{p^c}^{\times}(\boldsymbol{r}_j, \tau)\right]$.

For the axial coordinate of the l^{th} emitter, the amount of information SPLM signal is proportional to the partial derivation of the signal with respect to z_l as

$$\begin{aligned}\frac{\partial}{\partial z_l}\overline{S}_{\boldsymbol{\theta}}(\tau) = &-\frac{4\,\pi\, a_0\, a_1\, \mu(\tau)\, \zeta_0(\boldsymbol{r}_l)\, \alpha_{\text{sat}}}{\left(1 + \alpha_{\text{sat}}\, I(\boldsymbol{r}_l, \tau)\right)^2} \\ &\times \sum_{p=x,y} \zeta_{1,q}(\boldsymbol{r}_l, \tau)\; f_{p,z}(\tau) K_{p^c}(\tau) \sin\left(\Delta\Phi_p(\boldsymbol{r}_l, \tau) + \varphi_{1,p}(\boldsymbol{r}_l, \tau) - \varphi_0(\boldsymbol{r}_l)\right).\end{aligned} \tag{2.28}$$

In 2D, since there is no information about the y-dimension, $q = x$, and thus, the information about the emitter axial location is approximately half of that in the 3D case.

To write the Fisher information elements in a more concise expression, we denote the part of the partial derivative that depends on the specific STM illumination pattern employed as $\beta_u(\boldsymbol{r}_l, \tau)$, where u denotes the q-dimension of which the partial derivative is taken for the l^{th} emitter. That is

$$\beta_u(\boldsymbol{r}_l, \tau) = 4\,\pi\, a_0\, a_1\, \zeta_0(\boldsymbol{r}_l) \begin{cases} \zeta_{1,q}(\boldsymbol{r}_l, \tau)\, f_{q(\tau)}\, K_{q^c}(\tau) & , \quad q = x, y \\ \qquad \times \sin\left(\Delta\Phi_q(\boldsymbol{r}_l, \tau) + \psi_{1,q}(\boldsymbol{r}_l, \tau) - \psi_0(\tau)\right) & \\ \sum\limits_{p=x,y} \zeta_{1,q}(\boldsymbol{r}_l, \tau)\, f_{p(\tau)}\, K_{p^c}(\tau) & , \quad q = z. \\ \qquad \times \sin\left(\Delta\Phi_p(\boldsymbol{r}_l, \tau) + \psi_{1,p}(\boldsymbol{r}_l, \tau) - \psi_0(\tau)\right) & \end{cases} \tag{2.29}$$

2.2.7 Analysis of Parameter Correlations via the Hadamard Ratio of Fisher Information Matrix (FIM)

The expressions of the FI elements associated with the emitter location parameters in SPLM with CHIRPT illumination are rather complicated as shown above. In order to build meaningful physical interpretations of the CRLB with respect to the experimental parameters, it is essential for the FIM to be nearly diagonal so that the CRLB for unbiasedly estimating each location parameter can

be approximated by the inverse of its corresponding diagonal element in the FIM, i.e. $\sigma^2_{\hat{q}_l} \geq \mathscr{N}_m \, \overline{J}_{(n\,(l-1)+u)(n\,(l-1)+u)}/2$.

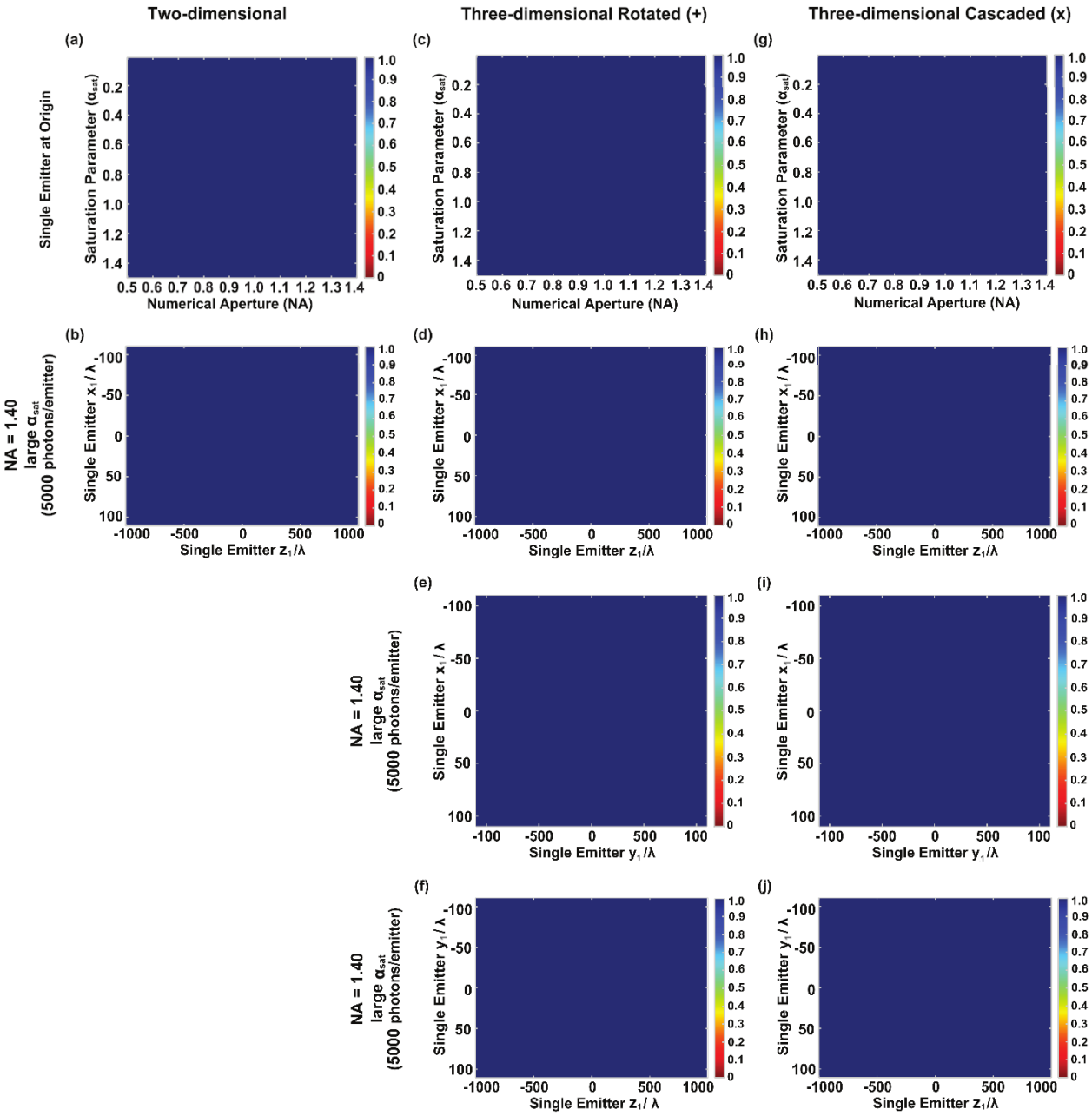

Figure 2.3: Hadamard ratio of the FIM for a single emitter localization via SPLM ($\lambda_{\text{ex}} = 500\,\text{nm}$, $t_c = 1\,\text{ms}$). (a), (c), (g) With respect to the objective lens NA from 0.50 to 1.40 and the saturation level α_{sat} from 0.01 to 1.50 with a single emitter at the origin. (b), (d), (h) With respect to the emitter location in $x-z$ plane at an objective lens NA of 1.40 and a saturation level α_{sat} corresponding to an expected photon detection count of 5000. (e), (i) With respect to the emitter location in $x-y$ plane under same NA and saturation levels. (f), (j) With respect to the emitter location in $y-z$ plane under same NA and saturation levels.

To determine if a FIM for emitter(s) localization via SPLM with STM illumination is nearly diagonal, we rely on Hadamard ratio, which is closely related to Hadamard's inequality [21]. Hadamard's inequality states that the absolute value of the determinant of a real-valued matrix $\boldsymbol{A}$ is bounded from above by the product of the Euclidean norms of the row or column vectors of the matrix $\boldsymbol{a}_i$, i.e. $|\det(\boldsymbol{A})| \leq \prod_i \|\boldsymbol{a}_i\|$, and equality is achieved if and only if the vectors are orthogonal [22]. In the case of FIM that is positive semi-definite, the right side of Hadamard's inequality can be simplified to the product of the diagonal elements, i.e. $\det(\boldsymbol{J}) \leq \prod_i J_{ii}$ [23]. Thus, the Hadamard's ratio for the FIM can be defined as the ratio between its determinant and the product of its diagonal elements [21],

$$h(\boldsymbol{J}) = \frac{\det(\boldsymbol{J})}{\prod_i J_{ii}}. \tag{2.30}$$

The closer the Hadamard ratio of the FIM is to 1, the more diagonally dominant the matrix is.

First, we examine the diagonality of the FIM for the localization of a single emitter. The Hadamard ratio of the FIM is plotted against the objective lens NA from 0.50 to 1.40 and the saturation parameter α_{sat} from 0.01 to 1.50 with the emitter assumed to be located at the origin in Fig. 2.3. Also plotted are the Hadamard ratio against the emitter location along the coordinate plane(s) within the STM illumination volume with full spatial frequency support at a large NA and a relatively large α_{sat} level to reflect a realistic experimental setting. With any STM illumination pattern used in and inspired by CHIRPT microscopy, the FIM for the localization of a single emitter has a Hadamard ratio of nearly 1 and thus, is nearly diagonal, under all the assumed ranges of the experimental parameters.

For the localization of multiple emitters, we study the dynamic of a pair of emitters as the correlations among multiple emitters can be considered pairwise. The top two rows in Fig. 2.4 are the Hadamard ratio of FIM for two emitter localization with respect to the objective lens NA and the saturation level α_{sat}. It is averaged over 100 random positions of the second emitter that is $0.1\,\lambda_{\mathrm{ex}}$ or λ_{ex} away from the first emitter that is fixed at the origin. The smaller distance chosen

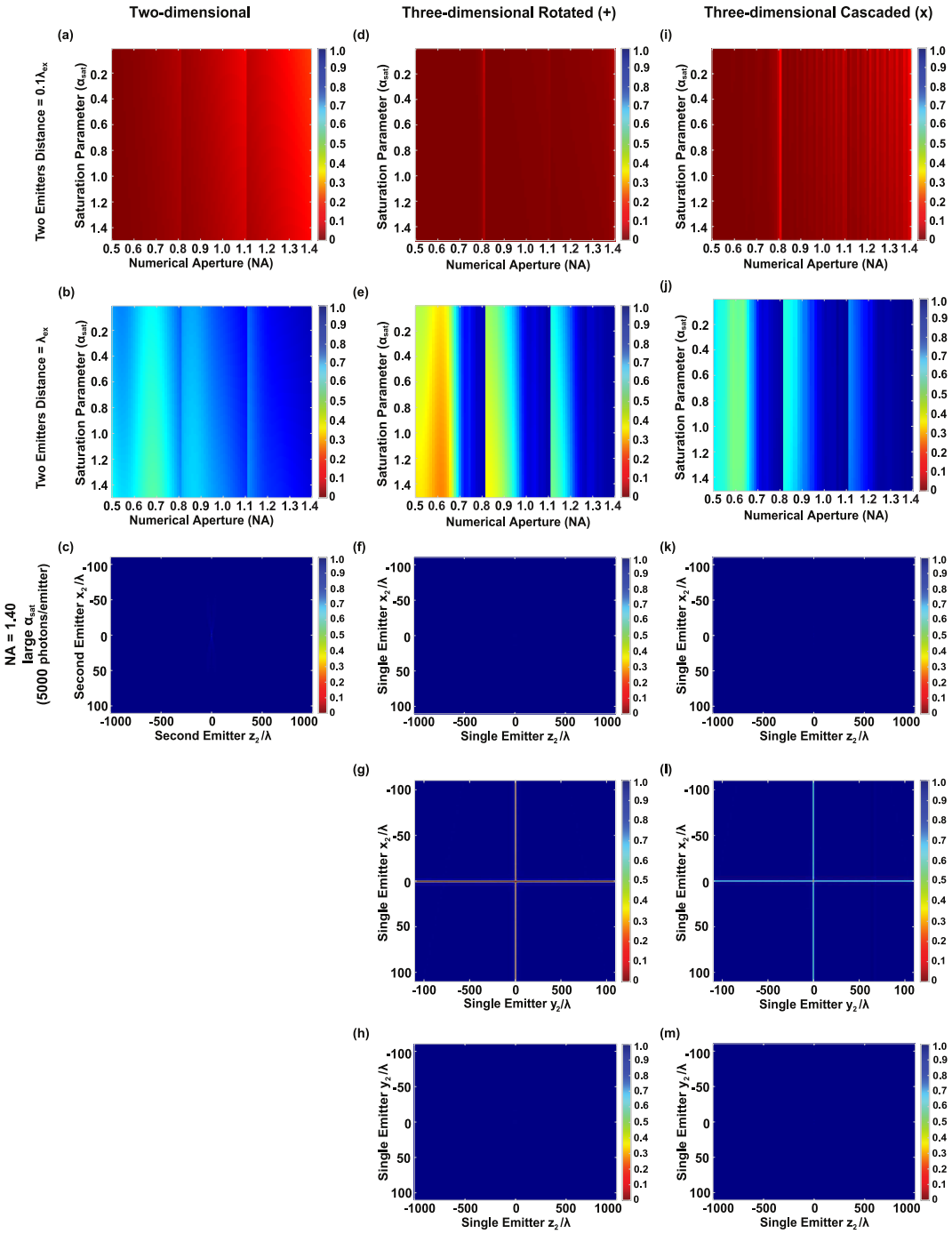

Figure 2.4: Hadamard ratio of the FIM for two emitter localization via SPLM with respect to the objective lens NA from 0.50 to 1.40 and the saturation level α_{sat} from 0.01 to 1.50 with one emitter at the origin and the other at (a), (d), (i) $0.1\ \lambda_{\mathrm{ex}}$ (b), (e), (j) λ_{ex}. With respect to the emitter location in (c), (f), (k) $x-z$ plane (g), (l) $x-y$ plane (h), (m) $y-z$ plane at an objective lens NA of 1.40 and a saturation level α_{sat} yielding an expected photon detection count of 5000.

represents a denser molar density. Under all NA and saturation values, the Hadamard ratio is nearly 0 regardless of the illumination pattern, indicating large correlations between location parameters, giving rise to large off-diagonal elements in the FIM correspondingly. It is important to point out that although the Hadamard ratio is close to 0, the LBEStd for estimating the emitter locations unbiasedly are still in the sub-$10\,$nm regime and therefore, when the Hamdamard ratio becomes degenerate, its value does not necessarily indicate the absolute degradation in the CRLB.

On the other hand, the larger distance chosen is the minimum distance such that the correlation between the two emitter locations should be negligible. This is to say that the corresponding FIM is nearly diagonal and thus, the localization CRLB becomes invariant to the emitter locations, which occurs when the distance between the two emitters is approximately greater than λ_{ex}. The Hadmard ratio is significantly larger as compared to the $0.1\,\lambda_{\text{ex}}$ under all NAs and all saturation levels, indicating that the FIM for the localization of two emitters is more diagonally dominated. In general, the larger the ratio between the objective lens NA and the refractive index (RI) it is immersed in, the more diagonally dominated the FIM becomes. This confirms the finding on a larger effect of NA on the localization CRLB than the saturation parameter. When the emitters are separated far enough from each other, the FIM is nearly diagonal if the ratio between numerical aperture and the objective immersion refractive index is large enough (e.g. $\text{NA}/\text{RI} \gtrsim 0.9$).

Also plotted in Fig. 2.4 are the Hadamard ratio with respect to the second emitter's location in the coordinate plane(s) within the STM illumination volume with full spatial frequency support when the first emitter is fixed at the origin under a large NA and a relatively high saturation level (total expected photon count $= 5000\,$emitters). The plots suggest that the FI becomes less diagonally dominated as the two emitters approach each other and there exists a strong correlation between their locations along the modulation axes with three-dimensional STM illumination, especially via the rotated method.

2.2.8 Geometric Interpretation of FIM

To further understand the correlation between any two location coordinates from two different emitters, we introduce one of the geometrical properties in the FI. That is the angle between a given sensitivity vector and the linear subspace spanned by the rest of the sensitivity vectors. When the angle approaches 90°, the given sensitivity vector becomes orthogonal to the subspace, suggesting that it is not collinear with any of the rest of the sensitivity vectors. Thus, when assessing its associated CRLB, it is expected to be comparable to the CRLB when the corresponding parameter of is the only parameter of interest since it should be more easily isolated for estimation. In the case of two emitter localization, the associated CRLB value should be twice as that in the single emitter localization case due to the increase in total shot noise. When the angles for all the sensitivity vectors approach 90°, the FIM is then nearly orthogonal and the parameter associated with the given sensitivity vector can be isolated for estimation with higher precision [40].

To calculate the angles, we view the FIM as a Gramian constructed from the sensitivity vectors,

$$\boldsymbol{J}[\boldsymbol{Y};\boldsymbol{\theta}] = \boldsymbol{G}^T\boldsymbol{G}, \tag{2.31}$$

where $\boldsymbol{G} = [\boldsymbol{g}_1, \cdots, \boldsymbol{g}_N]$ consists of sensitivity vectors as its columns. In the SPLM case, the i^{th} sensitivity can be expressed as $\boldsymbol{g}_i = 2\,\partial\sqrt{\boldsymbol{S}_{\boldsymbol{\theta}}}/\partial\theta_i$ and $\sqrt{\boldsymbol{S}_{\boldsymbol{\theta}}}$ denotes the element-wise square root of the mean photon count vector. To find the CRLB for the i^{th} parameter to be estimated, we can pull out the i^{th} sensitivity vector, $\boldsymbol{g}_i$ and rewrite the FIM as

$$\boldsymbol{J}(\boldsymbol{Y};\boldsymbol{\theta}) = \begin{bmatrix} \boldsymbol{g}_i^T\boldsymbol{g}_i & \boldsymbol{g}_i^T\boldsymbol{G}_i \\ \\ \boldsymbol{G}_i^T\boldsymbol{g}_i & \boldsymbol{G}_i^T\boldsymbol{G}_i \end{bmatrix}, \tag{2.32}$$

where $\boldsymbol{G}_i = \left[\cdots, \partial 2\sqrt{\boldsymbol{S}_{\boldsymbol{\theta}}}/\partial\theta_{i-1}, \partial 2\sqrt{\boldsymbol{S}_{\boldsymbol{\theta}}}/\partial\theta_{i+1}, \cdots\right]$ is a $2M \times (N-1)$ matrix with the column vector g_i removed. Then the inverse of the FI can be written as

$$\boldsymbol{J}^{-1}(\boldsymbol{Y};\boldsymbol{\theta}) = \begin{bmatrix} \dfrac{1}{\boldsymbol{g}_i^T(\boldsymbol{I}-\boldsymbol{P}_{\boldsymbol{G}_i})\boldsymbol{g}_i} & * \\ * & \dfrac{1}{\boldsymbol{G}_i^T(\boldsymbol{I}-\boldsymbol{P}_{\boldsymbol{g}_i})\boldsymbol{G}_i} \end{bmatrix}, \tag{2.33}$$

where $\boldsymbol{P}_{\boldsymbol{G}_i} = \boldsymbol{G}_i\left(\boldsymbol{G}_i^T\boldsymbol{G}_i\right)^{-1}\boldsymbol{G}_i^T$ is the projection matrix onto the $(N-1)$-dimensional subspace spanned by $\boldsymbol{G}_i$, denoted as $\langle \boldsymbol{G}_i \rangle$, and $\boldsymbol{P}_{\boldsymbol{g}_i} = \boldsymbol{g}_i(\boldsymbol{g}_i^T\boldsymbol{g}_i)^{-1}\boldsymbol{g}_i^T$ is the projection matrix onto the vector $\boldsymbol{g}_i$. It is clear that the CRLB for an unbiased estimator for the i^{th} parameter of interest, $\hat{\theta}_i$, is

$$\text{var}\left(\hat{\theta}_i\right) \geq \frac{1}{\boldsymbol{g}_i^T\left(\boldsymbol{I}-\boldsymbol{P}_{\boldsymbol{G}_i}\right)\boldsymbol{g}_i}, \tag{2.34}$$

which is the inverse of the squared Euclidean norm of the i^{th} sensitivity vector $\boldsymbol{g}_i$ projected onto the orthogonal complement of $\langle \boldsymbol{G}_i \rangle$, denoted as $\langle \boldsymbol{G}_i \rangle^{\perp}$. Therefore, the more orthogonal $\boldsymbol{g}_i$ is to $\langle \boldsymbol{G}_i \rangle$, the smaller the lower bound on error variance is in unbiasedly estimating θ_i, which indicates that the parameter associated with the given sensitivity vector can be isolated for estimation with high precision [40]. The angle between a sensitivity vector and the subspace spanned by the rest of the sensitivity vectors, thus, qualitatively determines the value of the LBEStd, which can be expressed as

$$\Psi_{\boldsymbol{g}_i} = \arccos\left(\frac{\boldsymbol{g}_i \cdot (\boldsymbol{P}_{\boldsymbol{G}_i}\boldsymbol{g}_i)}{\|\boldsymbol{g}_i\|\,\|\boldsymbol{P}_{\boldsymbol{G}_i}\boldsymbol{g}_i\|}\right) \tag{2.35}$$

for each sensitivity vector $\boldsymbol{g}_i$.

The presence and values of off-diagonal elements in the FI play an important role in determining the expressions and values of the LBEStd for unbiased localization using SPLM with STM Illumination as they indicate the level of correlation among parameters of interest. Their values can be probed via one of the geometric properties of the FI, the angle between the partial derivative $\boldsymbol{g}_i$ and the subspace the rest of the partial derivatives span. As mentioned above, such angle indicates the orthogonality of the FIM because $\boldsymbol{g}_i^T\boldsymbol{G}_i \to \boldsymbol{0}$ as $\Psi_{\boldsymbol{g}_i} \to \pi/2$ so that the off-diagonal elements

can be considered as negligible and the FIM is nearly diagonal. Therefore, we plot the angles between the sensitivity vectors of two fluorescent molecules and their subspace under various system parameter values.

For simplicity, one emitter is located at the origin while the other varies its location in one of the three coordinate planes over the STM illumination volume with full spatial frequency support, $220\,\lambda_{\text{ex}} \times 220\,\lambda_{\text{ex}} \times 2000\,\lambda_{\text{ex}}$, assuming a Gaussian beam with width $57\,\mu$m with wavelength of $500\,$nm.

Two-dimensional Localization

Angles between partial derivatives with respect to the position-varying emitter and their corresponding subspace are plotted in Fig. 2.5 with different sets of illumination objectives NA values and saturation levels.

There exist crisscross structures in the $x - z$ plane centered about the origin, similar to that observed in the plot of the Hadmard ratio of the FI in Fig. 2.4, where the sensitivity vectors become more collinear to their corresponding subspace. Consequently, when the second emitter is at one of these locations, even if the two emitters are far apart from one other, the lower bounds on error variance for jointly estimating each location parameter of emitters worsen due to the degeneracy in the FIM. The closer the angle is to 0, the higher the CRLB is evaluated from 2 times the CRLB in the single emitter case and eventually approaches infinity. As an example, when the two emitters are separated along the spatial frequency modulation x-axis within λ_{ex} of each other, Ψ_{x_2} and Ψ_{z_2} both exhibit a decrease followed by an increase before they start to approach 0. This behavior is reversed when it comes to the LBEStd, which should initially increase and then decrease before it approaches infinity.

Moreover, the collinearity structures change mainly with respect to the illumination objective NA due to its larger impact on the illumination pattern that is mainly determined by the spatial frequencies projected. Therefore, when two emitters are spaced on the order of λ_{ex} away from each other with a sufficiently large ratio between the objective numerical aperture and the objec-

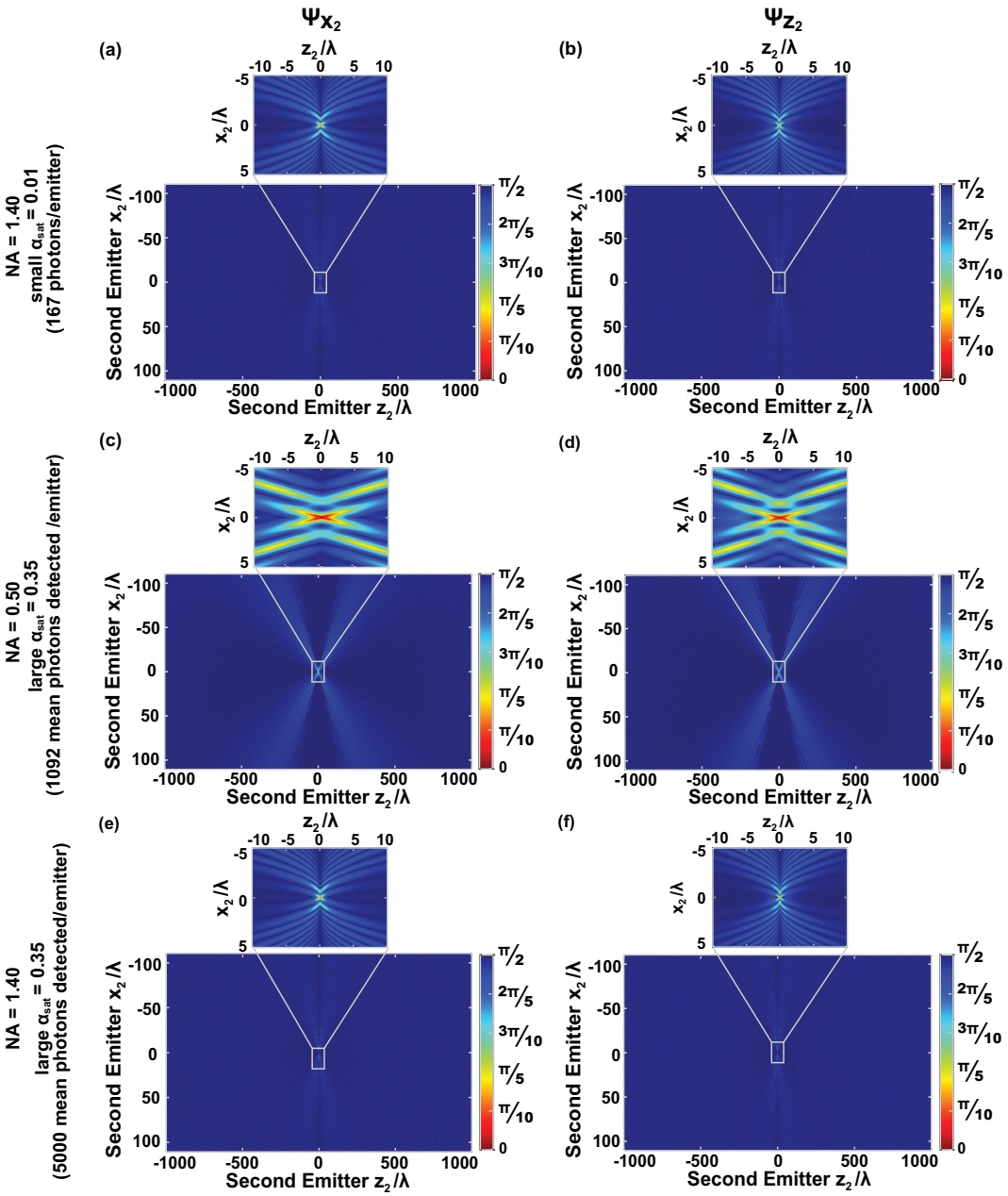

Figure 2.5: Angle between the partial derivative with respect to x_2 (left column) or z_2 (right column) and its corresponding subspace for 2D SPLM ($\lambda_{\text{ex}} = 500\,\text{nm}$, $t_c = 1.0\,\text{ms}$) with STM illumination used in CHIRPT microscopy as a function of the second emitter location. The corresponding subspace is spanned by the rest of the partial derivatives. Both emitters are assumed to be stationary during the signal acquisition process, with one located at the origin and the other varying its location. The illumination objective NA is fixed at 1.40 (RI of 1.518) with $\alpha_{\text{sat}} = 0.01$ (top row) as well as $\alpha_{\text{sat}} = 0.35$ (bottom row), and then at 0.50 (RI of 1.00) with $\alpha_{sat} = 0.35$ (middle row).

tive immersion refractive index (e.g. $\mathrm{NA}/\mathrm{RI} \gtrsim 0.90$), the correlation between the two emitter locations are low enough that the FIM is nearly diagonal.

Three-dimensional Localization

A subset of angles between partial derivative and their corresponding subspace is plotted for localization of two emitters are plotted as a function of the second emitter position in Fig. 2.6 using the rotated illumination method of three-dimensional SPLM with STM illumination and Fig. 2.7 using the cascaded illumination method. The subset of angles is chosen such that they demonstrate their general trend and dependence on the experimental parameters.

Due to the information coupling between the transverse axes in SPLM via saturation or via a specific illumination technique such as the cascaded method, the locations where the two emitter positions become more correlated are not exactly the same as the 2D SPLM. Similar to 2D, however, both 3D STM illumination patterns depend mainly on the objective NA. Thus, the larger the ratio between the objective NA and objective immersion RI, the less likely the second emitter is strongly correlated with the first one in the FOV.

With the rotated illumination method, when the two emitters are located along either spatial frequency modulation x- or y- axis, the emitter coordinate along that transverse axis becomes strongly correlated, especially at a low objective NA, with the same coordinate shared with the second emitter. Consequentially, the transverse LBEStd along that direction for both emitters increases. The much higher LBEStd correspond to the angle Ψ_{x_2} or Ψ_{y_2} approaching 0 as shown in Fig. 2.6. In addition, as the second emitter approaches the first emitter at the origin along either transverse x- or $y-$ axis, there is also a sinusoidal-like behavior in Ψ_{y_2} or Ψ_{x_2} and Ψ_{z_2} with an overall envelope that is approximately negative exponential. This should result in oscillations with an overall increase in the transverse and axial LBEStd. Finally, we note that similar to 2D SPLM, a sufficiently large ratio between the objective NA and objective immersion RI (e.g., NA/RI$\gtrsim 0.90$) and a sufficiently large separation distance (on the order of λ_{ex}) is necessary for the FIM of two emitter localization to be nearly diagonal. However, in practice, the minimum distance among emitters may be much smaller, e.g., on the order of $0.1\ \lambda_{\mathrm{ex}}$, for acceptable limits of precision.

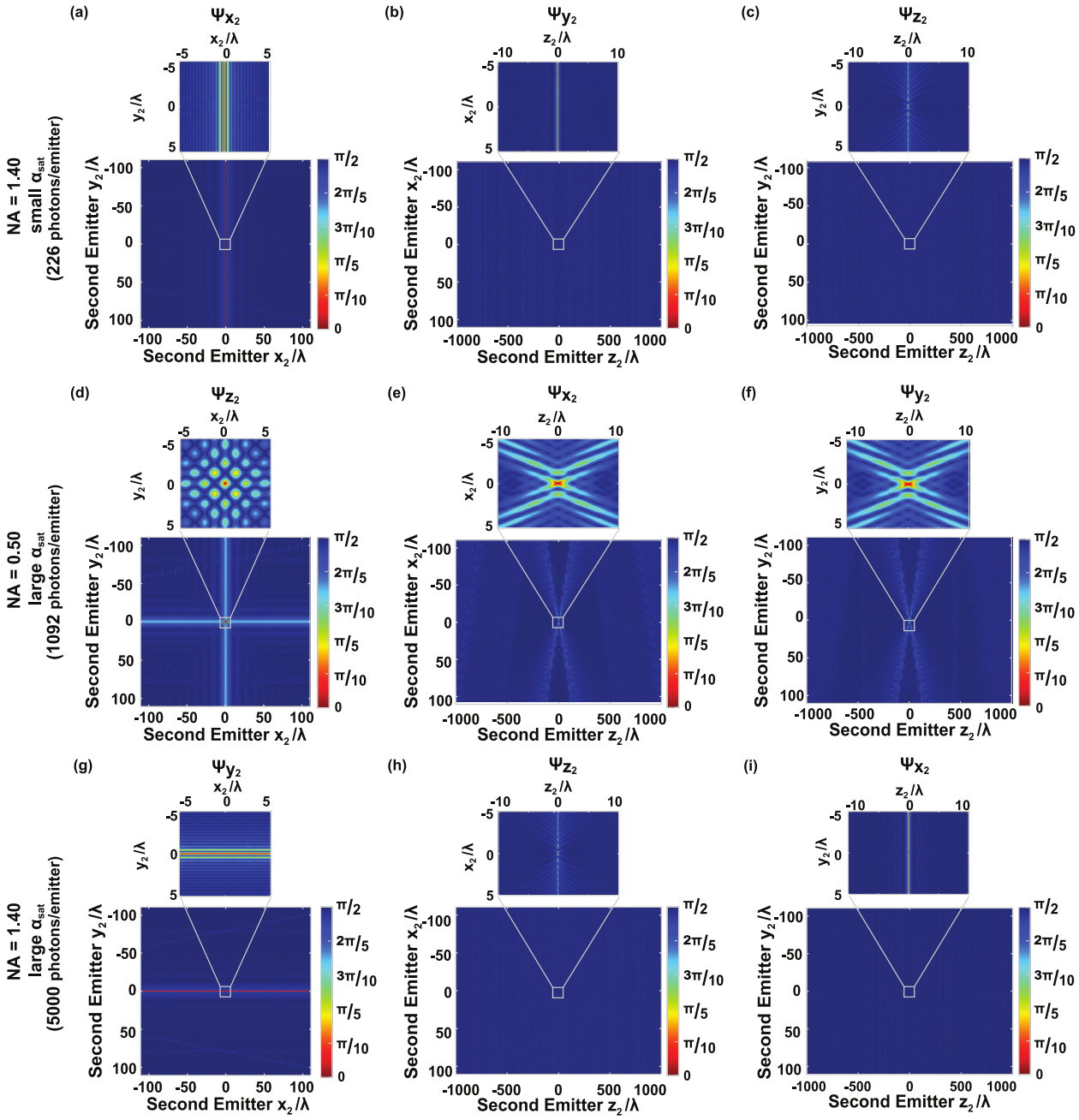

Figure 2.6: Angle between the partial derivative with respect to x_2 (a, f, h), y_2 (b, d, i), or z_2 (c, e, g) and its corresponding subspace for 3D SPLM ($\lambda_{\text{ex}} = 500\,\text{nm}$, $t_c = 1.0\,\text{ms}$) with STM illumination inspired by CHIRPT microscopy using rotated (+) method as a function of the second emitter location. The corresponding subspace is spanned by the rest of the partial derivatives. Both emitters are assumed to be stationary, with one located at the origin and the other varying its location. The illumination objective NA is first fixed at 1.40 (RI of 1.518) with $\alpha_{\text{sat}} = 0.01$ (top row) as well as $\alpha_{\text{sat}} = 0.26$ (bottom row) and then at 0.50 (RI of 1.00) with $\alpha_{\text{sat}} = 0.26$ (middle row).

With the cascaded illumination method, we find similarities in how the second emitter position becomes more correlated with the first emitter at the origin as compared to the rotated method. When the emitters are located along either spatial frequency modulation x- or y-axis, the transverse lower bounds on error variance for unbiasedly estimating the emitter locations along that direction is elevated regardless how far apart the emitters are from each other. The elevation in the transverse lower bounds on error variance, however, is much less than that using the rotated method as indicated by a larger Ψ_{x_2} or Ψ_{y_2}. This is due to the coupling of information between the transverse axes from the simultaneous modulation of both axes such that the information about the emitters along one axis helps distinguish the locations of the emitters along the other transverse axis. It indicates that the coupling not only increases the diagonal elements corresponding to the transverse coordinates in the FIM but also keeps the off-diagonal elements low.

Figs.2.6 and 2.7 not only give insights to localization precision dynamic for two emitters but also provide guidelines for localizing multiple emitters so that the associated FIM is diagonally dominated. These conditions include that emitters shall be separated by a sufficiently large distance (on the order of λ_{ex}), which is not along or parallel to either spatial frequency modulation axis, and a sufficiently large ratio between the objective lens NA and its immersion medium RI (e.g., $\mathrm{NA}/\mathrm{RI} \gtrsim 0.90$). However, these conditions do not necessarily guarantee the FIM to be nearly diagonal, especially when the number of emitters is large as the correlations among all the emitters are rather complicated. Under these conditions, however, the elevations in CRLB for estimating multiple emitter locations unbiasedly caused by correlations are kept at a relatively low level.

2.3 FI and CRLB Approximation for Single Emitter

In the context of LM, a lower CRLB indicates that there may exist an unbiased location estimator with a lower mean squared error, or in other words, a higher precision, from its true value. We define the $(n\,(l-1)+u)^{\mathrm{th}}$ parameter of interest as the location coordinate of the l^{th} emitter along the u^{th} dimension in n-dimensional SPLM, $n = 2, 3$. For two-dimensional localization, $u = 1, 2$

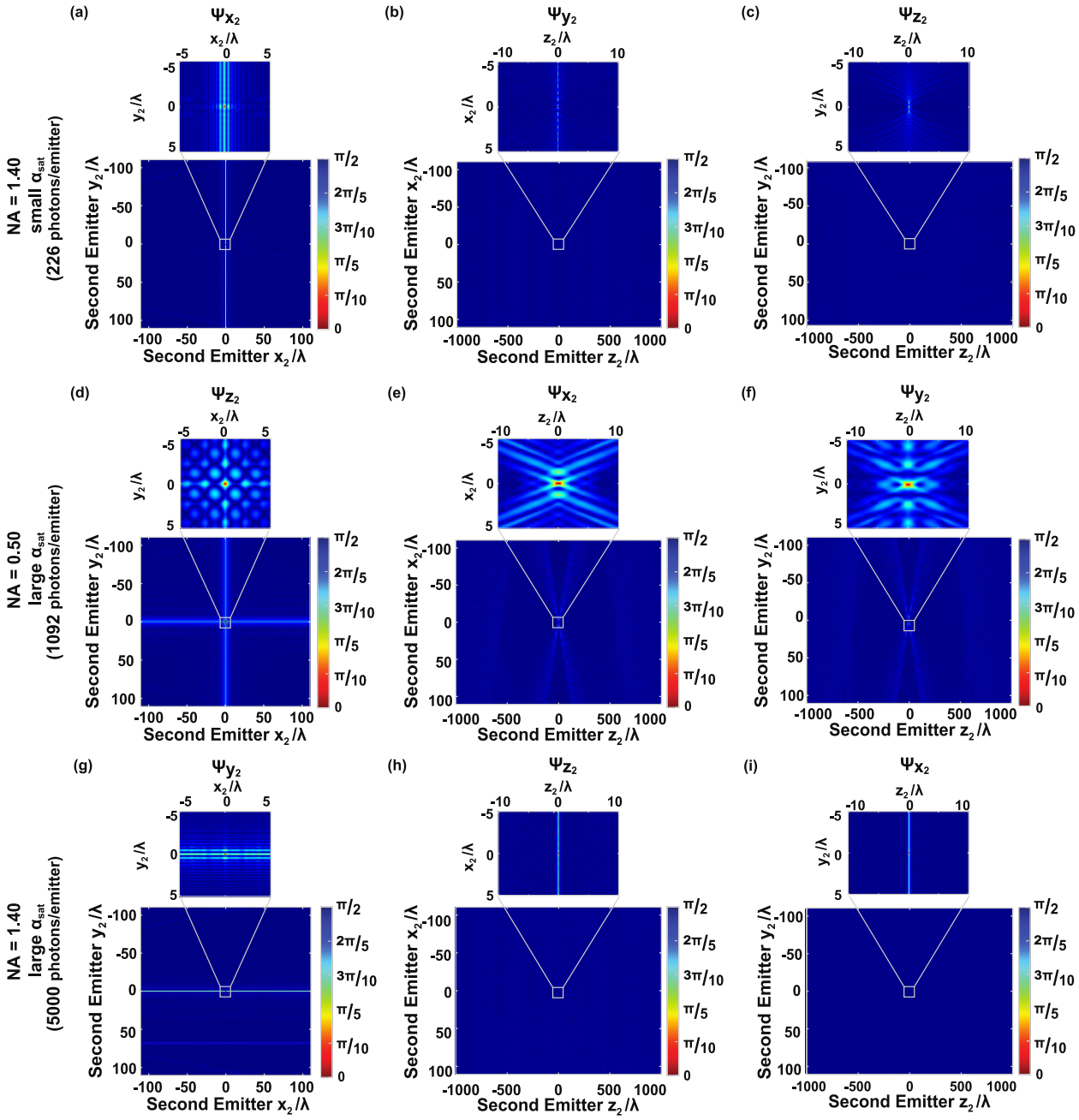

Figure 2.7: Angle between the partial derivative with respect to x_2 (a,f,h), y_2 (b,d,i), or z_2 (c,e,g) and its corresponding subspace for 3D SPLM ($\lambda_{\text{ex}} = 500\,\text{nm}$, $t_c = 1.0\,\text{ms}$) with STM illumination inspired by CHIRPT microscopy using cascaded ($\times$) illumination method as a function of the second emitter location. The corresponding subspace is spanned by the rest of the partial derivatives. Both emitters are assumed to be stationary with one located at the origin and the other varying its location. The illumination objective NA is first fixed at 1.40 (RI = 1.518) with $\alpha_{sat} = 0.019$ (top row) as well as $\alpha_{\text{sat}} = 0.53$ (bottom row), and then at 0.50 (RI = 1.00) with $\alpha_{\text{sat}} = 0.53$ (middle row).

correspond to the x- and z-dimension respectively. For three-dimensional localization, $u = 1, 2, 3$ correspond to the x-, y-, and z-dimension respectively.

The associated FI and CRLB are calculated from the likelihood function of the measured SPLM signal, which follows a Poisson distribution. The rate of the Poisson distribution is the expected number of photons measured within the integration time, i.e. SPLM signal duration $2\,t_c$ for the continuous-time model or the sample time Δt in the discrete-time model. The discrete-time model is assumed to be uniformly sampled such that $2\,M = 2\,t_c/\Delta t$ samples would be acquired. Thus, the FIM for N emitters to be localized in n-dimensional SPLM, $n = 2, 3$, can be expressed as

$$\boldsymbol{J}(\boldsymbol{\theta}) = \left[\frac{\mathscr{N}_m}{2}\,\overline{J}_{(n(l-1)+u)(n(s-1)+v)}\right]_{n\,N\times n\,N}, \tag{2.36}$$

where $\mathscr{N}_m = \eta_t\,(2\,t_c\,\Gamma_0)$ is the upper bound of the fluorescence count detected from a single emitter, $\overline{J}$ denotes the FI normalized by the product of the total detection efficiency η_t and the maximum fluorescence emission rate Γ_0, u, v index dimensions x, y, z, and l, s index the emitters to be localized.

To convert the FIM between the continuous-time and discrete-time models, the integral in the continuous-time model is replaced by an summation with respect to the sample index, $d\tau$ is replaced by Δt assuming that $S(t_m)$ is approximately constant over the integration time Δt, and the time variable t is replaced by $m\,\Delta t$. Since the conversion is straight-forward, expressions of the FIM elements as well as the CRLB are written in terms of the continuous-time model. This is also to help us study the dependence of CRLB on experimental parameters as when the integrands in the FIM are applied with appropriate approximations, their integrals can be evaluated to more concise forms, making evaluation of experimental parameters simpler.

Note that the diagonal elements in the above FIM depend the integral of a product between the sensitivities with respect to the same location coordinate while the off-diagonal elements depend the integral of a product between the sensitivities with respect to different location coordinates. Assuming that there is no background signal, their generalized expression, the $(n\,(l-1)+$

$u)(n\,(s-1)+v)^{\text{th}}$ element of the FI $\overline{J}$, can be written as

$$\overline{J}_{(n\,(i-1)+u)(n\,(j-1)+v)} = \alpha_{\text{sat}}^2 \int_{-1}^{1} \frac{1}{\sum\limits_{j} \dfrac{\alpha_{\text{sat}}\, I(\boldsymbol{r}_j,\tau)}{1+\alpha_{\text{sat}}\, I(\boldsymbol{r}_j,\tau)}} \frac{\beta_u(\boldsymbol{r}_l,\tau)\,\beta_v(\boldsymbol{r}_s,\tau)}{\left(1+\alpha_{\text{sat}}\, I(\boldsymbol{r}_l,\tau)\right)^2\left(1+\alpha_{\text{sat}}\, I(\boldsymbol{r}_s,\tau)\right)^2} d\tau, \tag{2.37}$$

where $\tau = t/t_c$ denotes the normalized time variable and $\beta_u(\boldsymbol{r}_l,\tau) = \left(\nabla_u\, I(\boldsymbol{r},\tau)\right)\big|_{\boldsymbol{r}=\boldsymbol{r}_l}$ denotes the partial derivative specific to the illumination pattern used in SPLM with respect to the $(n\,(l-1)+u)^{\text{th}}$ parameter evaluated at the true position of the l^{th} emitter. The integral in Eq. (2.37) depends primarily on the overall product between the spatial frequency projected along the u^{th} dimension at l^{th} emitter location and the spatial frequency projected along the v^{th} dimension at s^{th} emitter location.

In spite of the lack of concise closed-form expressions in terms of the experimental parameters for the derived FI, the general expression of the lower bound on error standard deviation (LBEStd) for estimating the u^{th} location coordinate of the l^{th} emitter unbiasedly can be compactly written as

$$\sigma_{\hat{q}_l} \geq \sqrt{\frac{2\,\det\left(\overline{M}_{(n\,(l-1)+u)(n\,(l-1)+u)}\right)}{\mathscr{N}_m\,\overline{D}_{\boldsymbol{\theta}}}} = C_{q_l}, \tag{2.38}$$

where $\hat{q}_l$ denotes any unbiased estimator for the l^{th} emitter location parameter along the u^{th} dimension, $\overline{M}_{(n\,(l-1)+u)(n\,(l-1)+u)}$ denotes the minor of the FIM associated with its $(n\,(l-1)+u)^{\text{th}}$ diagonal element, and $\overline{D}_{\boldsymbol{\theta}}$ is the determinant of the FIM. Here, the LBEStd for the parameter q_l is defined as the square root of the $(n\,(l-1)+u)^{\text{th}}$ diagonal element of the CRLB for estimating the location along u^{th} dimension for the l^{th} emitter. For simplicity, we adopt the notations C_{q_l} as the LBEStd for the parameter q_l.

When the FIM is nearly diagonal, the CRLB for unbiasedly estimating the location coordinate of the l^{th} emitter along the u^{th} dimension can be well represented by the formula

$$\sigma_{\hat{q}_l}^2 \geq \left(\frac{\mathscr{N}_m}{2}\,\overline{J}_{(n\,(l-1)+u)(n\,(l-1)+u)}\right)^{-1}. \tag{2.39}$$

For the localization of a single stationary emitter, its location coordinates are almost surely uncorrelated from each other for the ranges of experimental parameter values that SPLM is assumed to be operated under in our analyses, i.e. $0.50 \leq \mathrm{NA} \leq 1.40$ and $0.01 \leq \alpha_{\mathrm{sat}} \leq 1.50$. This implies that the FIM is nearly diagonal, which is validated through the evaluation of the Hadamard ratio in Fig. 2.3. Thus, we can first analytically study the dependence of the lower bound on error variance for unbiasedly estimating single emitter location parameters on the experimental parameters via its approximated form given by Eq. (2.39) in the continuous-time model.

2.3.1 Two-dimensional Localization

According to Eq. (2.39), the localization CRLB is approximately dependent on the maximal detected photon and the corresponding diagonal element in the FIM. For a given fluorophore, we first notice the maximal detected photon count $\mathscr{N}_m$ only depends on two of the experimental parameters, NA and RI. The higher the ratio between NA and RI, which can never exceed 1, the greater the maximum detected photon count for a given fluorescent label.

On the other hand, each diagonal element in the FIM, $\bar{\boldsymbol{J}}_{uu}$, exhibits a dependence on NA, RI, and saturation level in a more complicated way as shown in Eq. (2.37). To simplify the discussion, we will set the fringe visibility in the two-dimensional STM illumination, specified by Eq. (2.13), to unity, i.e. $\mu(t) \to 1$, and the normalized amplitude functions for the zeroth- and first-order diffracted beams to unity, i.e. $\{\zeta_0(\boldsymbol{r}_1), \zeta_1(\boldsymbol{r}_1, t)\} \to 1$. Since the diagonal elements $\bar{J}_{uu}$'s are scaled by the same denominator within their integrals for the same emitter, their values are determined by the partial derivatives of the SPLM signal with respect to the parameters of interest in the numerator. With STM illumination, each scaled partial derivative, $\overline{\beta}_u(\boldsymbol{r}_1, \tau) = f_q(\tau)\, \sin\left(\Delta\Phi_x(\boldsymbol{r}_1, \tau) + \psi_1(\boldsymbol{r}_1, \tau) - \psi_0(\boldsymbol{r}_1)\right)$, is approximately dominated by the wavelength-free spatial frequency modulation functions, $f_{\tilde{x}}(\tau) = \mathrm{NA}\, \tau$ for a transverse coordinate and $f_{\tilde{z}}(\tau) = \sqrt{\mathrm{RI}^2 - f_{\tilde{x}}^2(\tau)} - \mathrm{RI}$ for an axial coordinate when using a CHIRPT mask. Here, $\tilde{x} = x/\lambda_{\mathrm{ex}}$ and $\tilde{z} = z/\lambda_{\mathrm{ex}}$ denote coordinate variables normalized by the excitation wavelength while $\tau = t/t_c$ denotes the time variable normalized by half of the signal duration t_c, which result in $f_{\tilde{x}}(\tau) = \lambda_{\mathrm{ex}}\, f_x(t)$,

$f_{\tilde{z}} = \lambda_{\text{ex}}\, f_z(t)$. Therefore, the dependence of the diagonal elements in the FIM on the objective lens NA, RI, and α_{sat} can be approximated via wavelength-free FI elements, i.e. $\bar{J}_{uu} \propto \int_{-1}^{1} \left(f_{\tilde{q}}(\tau)\right)^2 d\tau$. This leads to a closed-form expression for the approximated ratio between the axial and transverse LBEStd in two-dimensional SPLM with STM illumination as $\int_{-1}^{1} \left(f_{\tilde{x}}(\tau)\right)^2 d\tau / \int_{-1}^{1} \left(f_{\tilde{z}}(\tau)\right)^2 d\tau$, which can be expressed in terms of the experimental parameters, when using a CHIRPT mask, as

$$r_{\sigma,\text{2D}} = \frac{C_{z_1}}{C_{x_1}} \approx \left(-1 + 6 \left(\frac{\text{NA}}{\text{RI}}\right)^{-2} - 3 \left(\frac{\text{NA}}{\text{RI}}\right)^{-2} \sqrt{1 - \left(\frac{\text{NA}}{\text{RI}}\right)^2} - 3 \left(\frac{\text{NA}}{\text{RI}}\right)^{-3} \sin^{-1}\left(\frac{\text{NA}}{\text{RI}}\right) \right)^{-1/2}. \tag{2.40}$$

Using the first three terms in the Taylor series for the integrand of the wavelength-free spatial frequency modulation function along the axial direction, the above ratio can be further simplified as

$$r_{\sigma,\text{2D}} \approx \left(\frac{3\,\text{NA}^2}{20\,\text{RI}^2} + \frac{3\,\text{NA}^4}{56\,\text{RI}^4} + \frac{5\text{NA}^6}{192\,\text{RI}^6} \right)^{-1/2}. \tag{2.41}$$

Moreover, for a low enough saturation ($\alpha_{\text{sat}} < 1.5$) under CW illumination, the dependence of the diagonal elements in the normalized FIM in two-dimensional SPLM with STM illumination via a CHIRPT mask can be approximated as $\bar{J}_{uu} \approx 3.31\,(1 - e^{-1.72\,\alpha_{\text{sat}}}) \int_{-1}^{1} \left(\overline{\beta}_u(\boldsymbol{r}_1, \tau)\right)^2 d\tau$. Taking the dependence of $\mathscr{N}_m$ on NA and RI as well as collection efficiency of the objective into consideration, the CRLB for single emitter localization can be more concisely approximated as

$$C_{x_1,\text{2D}}^2 \approx \left[1.65\,\eta_{\text{d}}\,\eta_{\text{op}}\,\Gamma_0\,t_c\,(1 - e^{-1.72\,\alpha_{\text{sat}}}) \left(1 - \sqrt{1 - \left(\frac{\text{NA}}{\text{RI}}\right)^2}\right) \frac{2}{3} \left(\frac{\text{NA}}{\lambda_{\text{ex}}}\right)^2 \right]^{-1} \tag{2.42}$$

and

$$C_{z_1,\text{2D}}^2 \approx r_{\sigma,\text{2D}}^2\, C_{x_1,\text{2D}}^2. \tag{2.43}$$

Note that $\mathrm{NA}/\lambda_{\mathrm{ex}}$ is also the maximum transverse spatial frequency projected onto the object, which suggests that the localization CRLB in two-dimensional SPLM with STM illumination depends on the maximum spatial frequencies project, i.e. $f_{x,\max}$ and $f_{z,\max}$, when using a CHIRPT mask.

However, the approximated expressions in Eqs. (2.42) and (2.43) do not take into account the time-varying fringe visibility function $\mu(t)$ resulted from a line focus in the two-dimensional STM illumination. $\mu(t)$ reduces the amount of information the observed data carry about the emitter location, resulting in the LBEStd approximately twice the square root of that in Eq. (2.42) for the x-coordinate and three times the square root of that in Eq. (2.43) for the z-coordinate. Thus, values calculated from the approximations should only be used to study the dependence of CRLB on the experimental parameters in SPLM when using the two-dimensional STM method.

2.3.2 Three-dimensional Localization

Following the same method of approximation, for a low enough saturation level ($\alpha_{\mathrm{sat}} < 1.50$), the FIM remains approximately diagonal. However, the approximate dependence of each diagonal element in the FIM, $\bar{J}_{uu}$, on α_{sat} differs slightly due to differences in the STM illuminations. In the rotated method, the diagonal element is given by $\bar{J}^{+}_{uu} \approx 5.87\,(1 - e^{-1.08\,\alpha_{\mathrm{sat}}}) \int_{-1}^{1} \left(\overline{\beta}_u(\boldsymbol{r}_1, \tau)\right)^2 d\tau$ while in the cascaded method, $\bar{J}^{\times}_{uu} \approx 1.22\,(1 - e^{-2.14\,\alpha_{\mathrm{sat}}}) \int_{-1}^{1} \left(\overline{\beta}_u(\boldsymbol{r}_1, \tau)\right)^2 d\tau$.

Like in the two-dimensional case, $\overline{\beta}_u(\boldsymbol{r}_l, \tau)$ here can be approximated by the wavelength-free spatial frequency modulation function, $f_{\tilde{x},\tilde{y}}(\tau) = \mathrm{NA}\,\tau$ for a transverse coordinate and $f_{\tilde{z}}(\tau) = \sum_{p=x,y} \left(\sqrt{\mathrm{RI}^2 - f^2_{\tilde{p}}(\tau)} - \mathrm{RI}\right)$ for an axial coordinate when using masks inspired by CHIRPT microscopy. Thus, the transverse CRLB for the localization of a single stationary fluorescent molecule in three-dimensional SPLM with STM illumination can be approximated by experimental parameters as, for the rotated case (+),

$$
\begin{aligned}
C^2_{x_1,\mathrm{3D},+} &= C^2_{y_1,\mathrm{3D},+} \\
&\approx \left(2.94\,\eta_{\mathrm{d}}\,\eta_{\mathrm{op}}\,\Gamma_0\,t_c\,(1 - e^{-1.08\,\alpha_{\mathrm{sat}}}) \left(1 - \sqrt{1 - \left(\frac{\mathrm{NA}}{\mathrm{RI}}\right)^2}\right) \frac{2}{3} \left(\frac{\mathrm{NA}}{\lambda_{\mathrm{ex}}}\right)^2 \right)^{-1},
\end{aligned}
\tag{2.44}
$$

and for the cascaded case ($\times$),

$$C^2_{x_1,\mathrm{3D},\times} = C^2_{y_1,\mathrm{3D},\times} \approx \left(0.61\,\eta_\mathrm{d}\,\eta_\mathrm{op}\,\Gamma_0\,t_c\,(1-e^{-2.14\,\alpha_\mathrm{sat}}) \left(1-\sqrt{1-\left(\frac{\mathrm{NA}}{\mathrm{RI}}\right)^2}\right) \frac{2}{3}\left(\frac{\mathrm{NA}}{\lambda_\mathrm{ex}}\right)^2 \right)^{-1}. \tag{2.45}$$

The axial LBEStd can be expressed as

$$C^2_{z_1,\mathrm{3D},+/\times} \approx 2\,r^2_{\sigma,\mathrm{2D}}\,C^2_{x_1,\mathrm{3D},+/\times} = 2\,r^2_{\sigma,\mathrm{2D}}\,C^2_{y_1,\mathrm{3D},+/\times}. \tag{2.46}$$

2.4 Numerical Evaluations of CRLB

To more precisely conclude the characteristics of SPLM in terms of its localization precision limit, we shift to a discrete-time model so that the CRLB can be computed numerically. Additional scenarios, such as background emitters and multiple emitters, are included for 3D due to its increased capabilities for practical applications. Again, the STM illumination strategies analyzed here have been used in and are inspired by CHIPRT imaging [11, 12].

2.4.1 Two-dimensional Localization: Single Emitter

We first plot the right-hand side of the inequalities in Eq. (2.38) with a single in-focus emitter at $\boldsymbol{r}_1 = (0,0)$ with respect to reasonable ranges of NA and α_sat to discern the dependence of NA and saturation level on the improvement in localization precision in Fig. 2.8. For plotting purposes, we have chosen $t_c = 1$ ms for a total of a 2 ms measured signal duration.

When plotted as a function of the illumination objective NA with a fixed saturation parameter at three different values, the LBEStd in both transverse and axial directions decreases as NA increases. This is because the sensitivity of the signal with respect to either location parameter is approximately quadratically dependent on the NA and part of sensitivity improvement is contributed by the improved ability of the objective to collect emitted photons at a higher NA. In other words, the product between the maximum spatial frequency projected onto the emitter and the

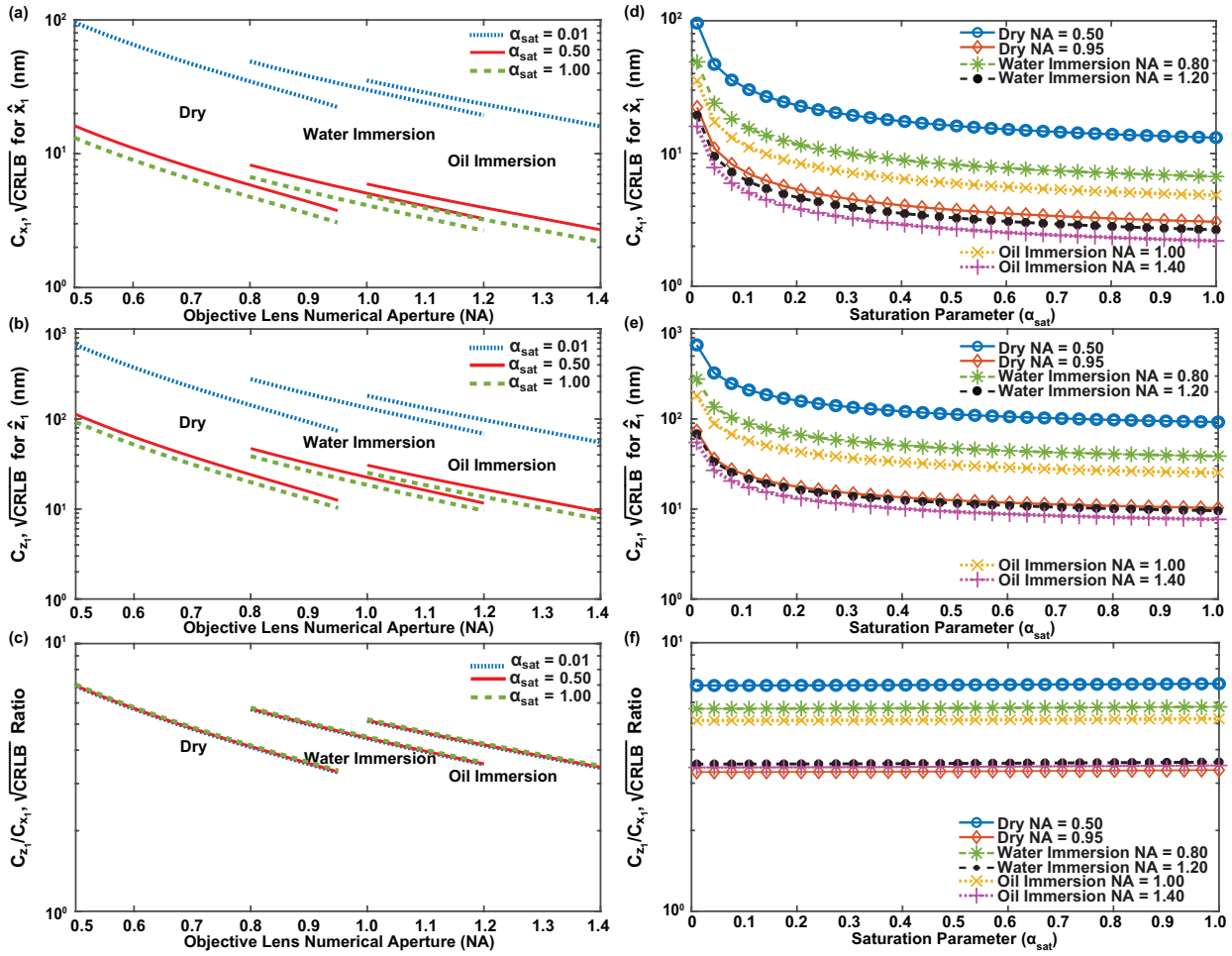

Figure 2.8: LBEStd and ratio between the transverse and axial LBEStd for unbiasedly estimating the location parameters of a stationary in-focus single fluorescent emitter at $(0, 0)$ in two-dimensional background-free SPLM ($\lambda_{\text{ex}} = 500\,\text{nm}$, $t_c = 1\,\text{ms}$) with STM illumination via a CHIRPT mask as a function of NA and α_{sat}. (a), (b) LBEStd with NA under various immersion mediums, dry (RI $= 1.00$), water (RI $= 1.33$), and oil (RI $= 1.518$). Lines correspond to α_{sat} of 0.01 (dotted), 0.50 (solid), 1.00 (dashed). (d), (e) LBEStd curves correspond to NA of 0.50 (solid with $\circ$), 0.95 (solid with $+$), 0.85 (dashed with $*$), 1.20 (dashed with $\cdot$), 1.00 (dotted with $\times$), and 1.40 (dotted with $+$). (c), (f) $r_{\sigma,2\text{D}}$.

square root of the collection efficiency, $f_{x,\max}\sqrt{\eta_c}$ or $f_{z,\max}\sqrt{\eta_c}$, both of which depend on NA, determines the LBEStd when the saturation level is fixed. For example, at a fixed saturation level of 1.00, a water immersion lens of NA $= 1.13$ yields a similar transverse LBEStd at $3.05\,\text{nm}$ as a dry lens of NA $= 0.95$. A dry lens of NA $= 0.95$ has a collection efficiency of 34.39% and collects a maximum transverse spatial frequency of $1.90\,/\mu\text{m}$ while a water-immersion lens of NA $= 1.13$ has a collection efficiency of 21.00% and collects a maximum transverse spatial frequency of $2.46\,/\mu\text{m}$ with a CHIRPT mask, both of which produce a product $f_{x,\max}\sqrt{\eta_c}$ around $1.12\,/\mu\text{m}$.

The LBEStd is also plotted as a function of the saturation parameter under fixed NA values. Since the increase in α_{sat} leads to an increase in the excited state population, e, and thus, leads to an increase in the emitted, and consequently detected photons, the transverse and axial LBEStd decrease. At low values of α_{sat}, where increases in the excited state population respond linearly to an increase in illumination intensity, the LBEStd scales approximately proportional to $1/\sqrt{\alpha_{\mathrm{sat}}}$. Larger values of the saturation parameter, however, provides diminishing gains in the excited state population, and thus, reduces the rate of decrease in the LBEStd until that the saturation is so large that the SPLM signal becomes constant, which leads to decreasing partial derivatives of the observed data with respect to the location parameters as a function of $1/\alpha_{\mathrm{sat}}$. Consequentially, the LBEStd increases at a rate of α_{sat}. This does not occur until the saturation level is extremely high (e.g. $\gtrsim 4.00$ when using a CHIRPT mask).

Plotted last in Fig. 2.8 is the ratio between axial and transverse LBEStd. The dependencies on NA and α_{sat} follows those indicated by Eq. (2.40), where the LBEStd decreases as a function of the ratio between NA and its corresponding RI but does not vary with respect to the saturation parameter.

Aside from understanding the dependence of CRLB on the experimental parameters, one of the most important experimental considerations for LM is to decide what precision may be achieved for a given detected (and thus emitted) photon budget. These relationships are presented in Fig. 2.9. The dotted lines correspond to varying saturation parameter values under fixed NA values while the solid lines correspond to varying NA values under fixed saturation parameter values.

At any fixed saturation level or any fixed illumination objective NA, both transverse and axial LBEStd decrease as the detected photon count increases. This validates that a larger NA and/or a higher saturation level (i.e. a higher illumination intensity) drive the variation of the SPLM intensity to be steeper, or in other words, more sensitive, with respect to the emitter position. On the other hand, as indicated by the approximate expression given in Eqs. (2.42) and (2.43), the rate of decrease in LBEStd is much greater with respect to NA than saturation. However, we note that a higher saturation will allow a given number of photons to be detected in a shorter time period with

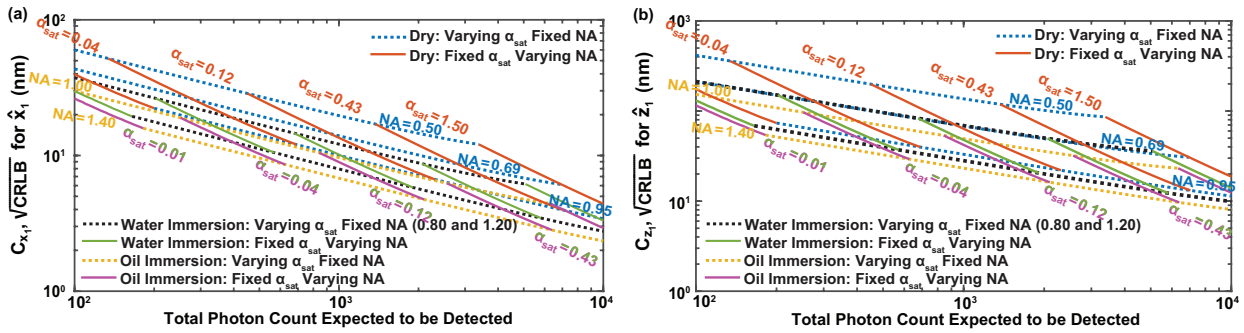

Figure 2.9: LBEStd for unbiasedly estimating the location parameters of a stationary in-focus single fluorescent emitter at $(0, 0)$ in two-dimensional background-free SPLM ($\lambda_{\text{ex}} = 500\,\text{nm}$, $t_c = 1\,\text{ms}$) with STM illumination via a CHIRPT mask as a function of the expected total number of photons. Dotted Lines correspond to fixed NA values under various immersion mediums with a sweep of saturation parameter from 0.01 to 1.50. Solid lines correspond to fixed saturation parameter α_{sat} values at 0.01, 0.13, and 1.50 with a sweep of NA from 0.50 to 0.95 with a dry lens ($\text{RI} = 1.00$), from 0.80 to 1.20 with a water immersion lens ($\text{RI} = 1.33$), and from 1.00 to 1.40 with an oil immersion lens ($\text{RI} = 1.518$).

the same NA and therefore, allows SPLM to achieve a similar localization precision with a lower saturation parameter with a longer signal duration. This could further reduce the data acquisition time.

2.4.2 Two-dimensional Localization: Two Emitters

The simplest case to quantify the joint localization capability of two-dimensional SPLM with STM illumination concerns two fluorescent molecules, which are assumed to share the same photon emission and detection rates, located in the object region at $(-d/2, 0)$ and $(d/2, 0)$ or $(0, -d/2)$ and $(0, d/2)$ without any background emitter. Analyzing the LBEStd for unbiasedly estimating the two emitter locations helps determine the limit in spacing between emitters such that they may still be distinguished as two separate emitters.

Similar to the LBEStd for estimating a single emitter location, the LBEStd for estimating the locations of two emitters can be improved with an increased maximum projected spatial frequency and a greater saturation parameter. To isolate the effect of distance between two emitters, C_{x_1}, C_{x_2}, C_{z_1}, and C_{z_2} are plotted with respect to d in Fig. 2.10 with fixed illumination objective NA of 1.40 and saturation parameter of 0.35 such that the corresponding expected photon detection count is 5000 from each fluorescent molecule.

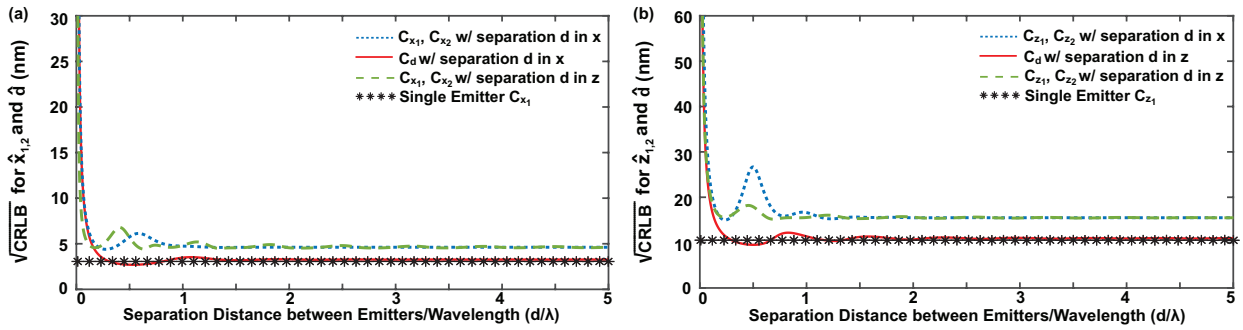

Figure 2.10: LBEStd for unbiasedly estimating the locations of two stationary fluorescent emitter and their separation distance in two-dimensional background-free SPLM ($\lambda_{\text{ex}} = 500\,\text{nm}$, $t_c = 1\,\text{ms}$) with STM illumination via a CHIRPT mask (total expected photon detection count $= 5000/\text{emitter}$) as a function of their separation distance. $C_{x_{1,2}}$ and $C_{z_{1.2}}$ with emitters separated along x- (dotted) and z-dimension (dashed). C_d (solid) with emitters separated along x- and z=dimension respectively. Reference C_{x_1} and C_{z_1} ($*$) under the same experimental parameter values for the localization of a single in-focus stationary emitter.

When the two emitters are separated more than approximately λ_{ex} from each other along either direction, the transverse LBEStd converges to approximately $4.6\,\text{nm}$ while the axial LBEStd converges to approximately $15.6\,\text{nm}$. Each value that the LBEStd converges to is approximately $\sqrt{2}$ times than that in the single emitter case ($3.06\,\text{nm}$ for the x-coordinate and $10.53\,\text{nm}$ for the z-coordinate). Such elevation in the two emitter case is primarily due to an increase in shot noise, which is now contributed by two emitters rather than one. In estimation theory, this phenomenon is well explained via the presence of parameters not of immediate interest, which are referred to as nuisance parameters [39]. Inferring the true values of the location parameters of interest, i.e. location coordinates of one emitter, from the observed data becomes more difficult because the presence of nuisance parameters, i.e. the location coordinates of the second emitter, may cause the data to have similar values as those generated from a different set of values for the parameters of interest.

Additional increase in the LBEStd results from the correlations between emitter locations. From the FIM standpoint, correlations correspond to increased off-diagonal elements and when the correlation is large, the off-diagonal elements become large so that the FIM is less diagonally dominated and consequentially, the CRLB increases. When the distance between the two emitters decreases below approximately $0.07\,\lambda_{\text{ex}}$, two emitter locations become significantly correlated so

that their locations are no longer distinguishable, i.e. $\max\left\{C_{x_{1,2}}, C_{z_{1,2}}\right\} \geq d$. Eventually, the LBEStd diverges to infinity. This behavior is analogous to the Rayleigh criterion for resolution.

Evidentially, the increase in each LBEStd is not monotonic with respect to the separation distance between emitters. It peaks at locations where the corresponding partial derivative is more collinear with the partial derivative(s) with respect to the location parameters of the other emitter. When two of the emitter location parameters become perfectly correlated, the angle between each of the corresponding partial derivatives, known as the sensitivity vectors or the elements in the Fisher score, and their corresponding subspace spanned by the rest of the partial derivatives approach 0. This leads to a loss of rank in the FIM and the CRLB diverging to infinity. Thus, the angles between sensitivity vectors and their subspace can be used to infer the experimental conditions where the corresponding FIM is nearly diagonal and thus, the LBEStd for unbiasedly estimating two emitter locations are approximately scaled from those in the localization of a single emitter by a factor of $\sqrt{2}$. These experimental conditions are determined to be a sufficiently large separation ($d \gtrsim \lambda_{\text{ex}}$) and a sufficiently large ratio between the objective lens NA and its immersion medium RI ($\text{NA}/\text{RI} \gtrsim 0.90$).

These conditions can be extended as a rule of thumb for the case of N emitter localization where the LBEStd is approximated via scaling by $\sqrt{N}$. Note that these conditions do not necessarily guarantee the FIM to be nearly diagonal, especially when the number of emitters is large, as the correlations among a large number of emitters are rather complicated. However, they provide guidelines for potentially lower correlations among emitter locations and reasonable LBEStd.

Instead of estimating locations of both emitters, the distance between the two can be the parameter of interest when the absolute positions hold little value. Since the distance between two emitters exhibits a linear mapping from the original parameters of interest, the LBEstd for the scalar parameter d can also be computed via

$$\boldsymbol{J}(d) = \boldsymbol{A}^T \boldsymbol{J}(\boldsymbol{\theta}) \boldsymbol{A}, \tag{2.47}$$

where $\boldsymbol{A}$ is the Jacobian vector with its i^{th} element being $\partial\theta_i/\partial d$. Using $\boldsymbol{J}(\boldsymbol{\theta})$ evaluated at true emitter locations along one of the axes, the LBEStd for an unbiased estimator for the separation distance, C_d, is plotted as a function of separation distance in Fig. 2.10. Its behavior follows the transverse and axial LBEStd where as the two emitters approach each other, its value diverges to infinity. When the two emitters are far enough apart from each other, C_d approaches the LBEStd for estimating a single emitter location in the corresponding dimension due to the lack of nuisance parameters since the measurement model is characterized by a single parameter, the separation distance d. There are no off-diagonal elements in the FI and thus, the amount of information carried by the measurement about each axis directly contributes to the unbiased estimation of the separation along that direction, just like the case of single emitter localization.

2.4.3 Three-dimensional Localization: Single Emitter

Three-dimensional SPLM with STM illumination requires introducing spatial frequency modulation along the y-dimension with the same mask at a different carrier frequency or a different modulation rate. It is expected to provide the same amount of information regardingthe emitter's y- and z-coordinate as the spatial frequency modulation along x-dimension regarding emitter's x- and z-coordinate respectively. Therefore, both transverse CRLB should be identical and comparable in values to the two-dimensional case, provided that no coupling is introduced between the modulation axes (e.g. with the rotated method under a sufficiently small saturation level). The axial CRLB should improve approximately twice as much as the two-dimensional case due to double the amount of information content contributed by the spatial frequency modulations along the orthogonal transverse $x - y$ axes.

The cascaded method, on the other hand, couples information about the transverse x- and y-coordinates. Unlike the rotated method where the observed data can be approximately split into two equal parts, one for x-dimension and the other for y-dimension, when the saturation level is low enough, the observed data acquired using cascaded method contains information about both transverse dimensions simultaneously. That is the diagonal elements $J_{(3\,(l-1)+u)(3\,(l-1)+u)}$'s

increase in the FIM. In addition, since the information about one transverse axis can be used to distinguish the location of emitters along the other axis and consequently, it lowers the correlation between coordinates. Thus, the transverse and axial CRLB using cascaded method should be lower than those using rotated method under the same experimental parameter values as well as those in the two-dimensional case.

However, the coupling between the transverse $x-y$ dimensions can also result from saturation in the photophysics of fluorescence. As the saturation level increases, the information that the observed three-dimensional SPLM data carry about the transverse dimensions starts to couple, i.e. $J_{(3\,(l-1)+u)(3\,(l-1)+u)}$'s increase. On the contrary, the transverse dimensions also become correlated, where the off-diagonal elements for the same emitter $J_{(3\,(l-1)u)(3\,(l-1)+v)}$'s increase, $u \neq v$. For a reasonable range of saturation level ($\alpha_{\mathrm{sat}} < 1.50$), the increased off-diagonal elements are still negligible as compared to the diagonal elements $J_{(3\,(l-1)+u)(3\,(l-1)+u)}$'s.

To illustrate the information coupling effect between transverse coordinates and understand the dependence of CRLB on the experiment parameters, we plot the LBEStd for localizing a stationary in-focus single emitter with no background signal as a function of the illumination objective NA and the saturation level respectively in Fig. 2.11.

It shows that the general dependence of the transverse and axial LBEStd in three-dimensional localization on the objective lens NA and the saturation parameter α_{sat} follows the two-dimensional case. Compared to the two three-dimensional techniques, on the other hand, the cascaded method improves the transverse and axial LBEStd due to the coupling of information the signal provides between the transverse $x-y$ directions as mentioned above.

Also plotted are the approximate expressions of the LBEStd. All approximate expressions show good agreement with the actual values, suggesting that in the range of the saturation parameter values plotted, the coupling the correlation between the transverse $x-y$ dimensions resulted from saturation are not strong enough for the LBEStd to deviate much. Therefore, the FIM for estimating the single emitter location in three-dimensional SPLM with STM illumination is nearly

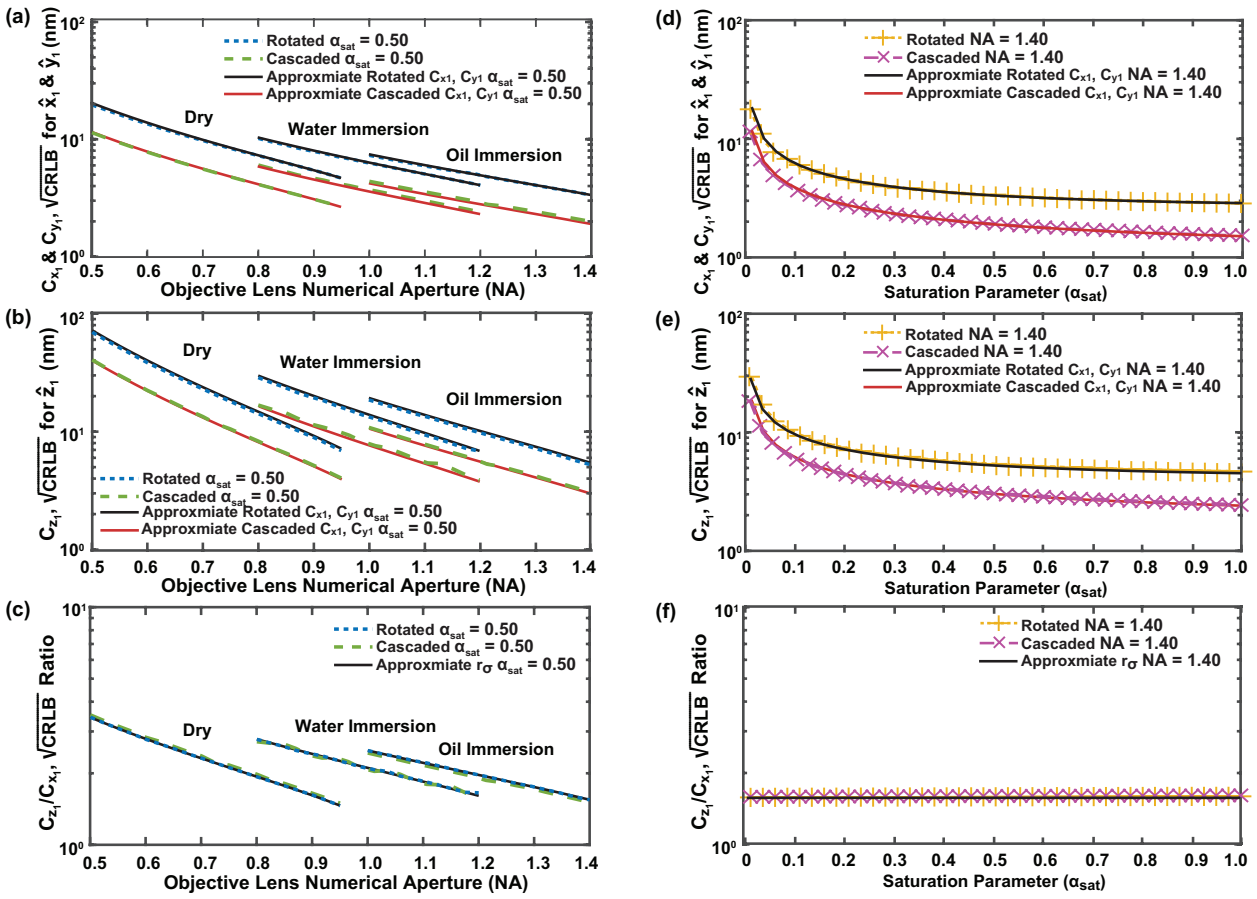

Figure 2.11: LBEStd for unbiasedly estimating the location of a single in-focus stationary fluorescent emitter at $\boldsymbol{r}_1 = (0, 0, 0)$ in three-dimensional background-free SPLM ($\lambda_{\text{ex}} = 500\,\text{nm}$, $t_c = 1\,\text{ms}$) with STM illumination using rotated method (dotted, dotted with $+$) and cascaded method (dashed, dashed with $\times$) as functions of NA ($\alpha_{\text{sat}} = 0.50$) and α_{sat} (NA $= 1.40$). (a), (b) C_{x_1}, C_{z_1} and their approximates (black solid for rotated method and red solid for cascaded method) as functions of NA under various immersion mediums, dry (RI $= 1.00$), water (RI $= 1.33$), and oil (RI $= 1.518$), (d), (e) C_{x_1}, C_{z_1} and their approximates as functions of α_{sat}. (c), (f) $r_{\sigma,\text{3D}}$ and their approximates as functions of NA and α_{sat}.

diagonal regardless of the illumination method under the ranges of experimental values used for plotting purposes.

Since a major advantage of using STM illumination is that the DOF over which LM may be expanded is significantly increased, we plot the LBEStd for unbiasedly estimating the location of a single stationary emitter as functions of the emitter z-position in Fig. 2.12. We assume that the excitation beam has a wavelength of $500\,\text{nm}$ that is Gaussian distributed in space with a width of $57\,\mu\text{m}$ and the total magnification of the imaging system is 77. Within the region of full spatial frequency support, approximately $537\,\mu\text{m}$ full-width-at-half-maximum (FWHM) depth using the

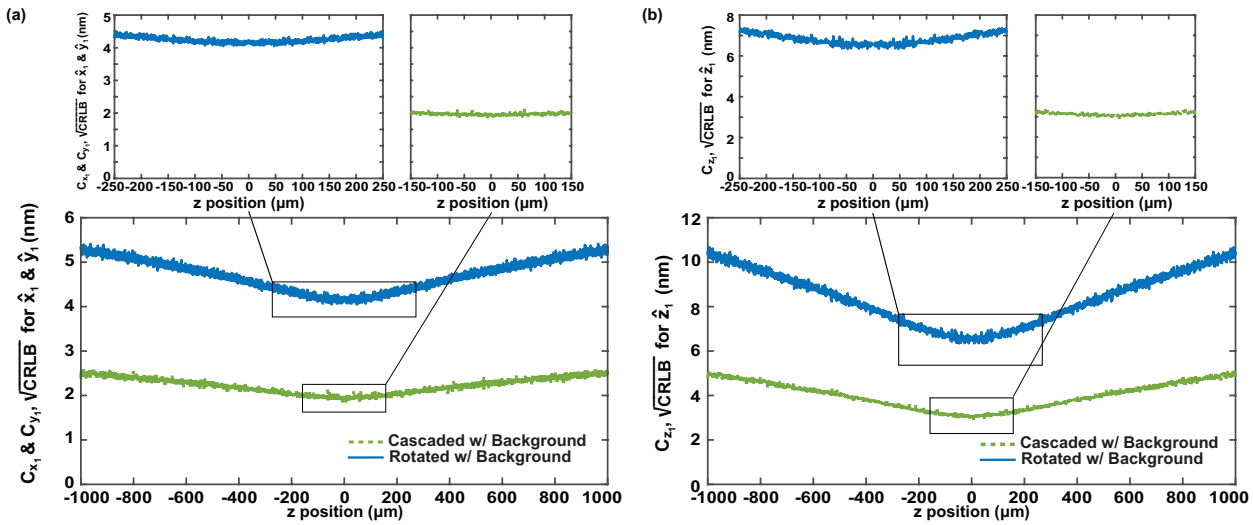

Figure 2.12: LBEStd for unbiasedly estimating the location of a single stationary emitter at $\boldsymbol{r}_1 = (0, 0, z)$ in three-dimensional background-free SPLM ($\lambda_{\text{ex}} = 500\,\text{nm}$, $t_c = 1\,\text{ms}$, $\text{NA} = 1.40$, $\text{RI} = 1.518$) with STM illumination (total expected photon detection count $= 5000$/emitter) using rotated method ($\alpha_{\text{sat}} = 0.53$, solid) and the cascaded method ($\alpha_{\text{sat}} = 0.26$, dashed) as functions of emitter z-position. (a) C_{x_1} and C_{y_1}. (b) C_{z_1}.

rotated method and $380\,\mu$m FWHM depth using the cascaded method, the lower bounds on error standard deviation remain relatively constant with respect to the emitter z-position. This is because the information about the emitter location is purely proportional to the intensity profile of the illumination pattern, which is relatively flat within the full spatial frequency support region. As the emitter moves away from the said region, the LBEStd increases approximately linearly with respect to the emitter z-position as the projected maximum spatial frequency decreases approximately as a linear function of z. Due to such temporal dynamics in the spatial frequency projections, which may equivalently be considered as a time-varying NA, the localization DOF of SPLM with STM illumination is extended to 10's mm.

Background Light Detection

In a realistic experimental setup for SPLM with STM illumination, photons from molecules that are not the targets, e.g., autofluorescence, often cannot be eliminated and therefore, need to be accounted for in calculating the CRLB for localizing fluorescent molecules. Such background flu-

orescent emission increases the overall shot noise in the measured SPLM signal and consequently, increases the uncertainty of localization.

We assume the photons emitted from the background fluorescence to be distributed through the illumination volume within the background medium. As a result, the background fluorescent emission rate follows a Poisson process with a constant rate, B_t, with respect to time. The Fisher information for a given observation then becomes

$$J_{\mathrm{B}}(\boldsymbol{\theta}) = \frac{\mathscr{N}_m}{2} \sum_{m=-M}^{M} \frac{\eta_t \, \Gamma_0 \, \Delta\tau}{\eta_t \, \Gamma_0 \, \overline{S}_{\boldsymbol{\theta}}[m] + B_t} \cdot \left(\frac{\partial}{\partial \boldsymbol{\theta}} \overline{S}_{\boldsymbol{\theta}}[m] \right)^T \frac{\partial}{\partial \boldsymbol{\theta}} \overline{S}_{\boldsymbol{\theta}}[m], \tag{2.48}$$

where $\overline{S}[m]$ denotes the SPLM signal normalized by the upper bound of the photon detection count per emitter $\mathscr{N}_m$ and B_t denotes the background fluorescent signal detection rate that is assumed constant and much smaller as compared to the photon detection $\eta_t \, \Gamma_0$ per fluorescent emitter since background emitters are not likely to emit photons at either excitation or detection wavelength. Here we have adopted the discrete-time model as it reflects the actual data acquisition process and there is no need to derive approximate expressions using the continuous-time model.

To illustrate how LBEStd in SPLM with STM illumination are affected by background noise, they are plotted in Fig. 2.13 as functions of background fluorescent rate B_t as well as signal-to-background rate (SBR) with a stationary in-focus single emitter with a mean photon detection count of 5000 under a fixed NA of 1.40. SBR is defined as the ratio between the expected number of photons detected from the target fluorescent molecule and the expected number of photons detected from the background. As with all other SMLM techniques, the transverse and axial LBEStd using SPLM decreases and approaches the background-free CRLB as the SBR increases, or in other words, the number of photons detected from background decreases. At a high background fluorescent detection rate 250 photons/μs, which yields a SBR of 0.01, the transverse LBEStd is 47.93 nm (rotated) and 20.97 nm (cascaded) while the axial LBEStd is 75.60 nm (rotated) and 33.13 nm (cascaded).

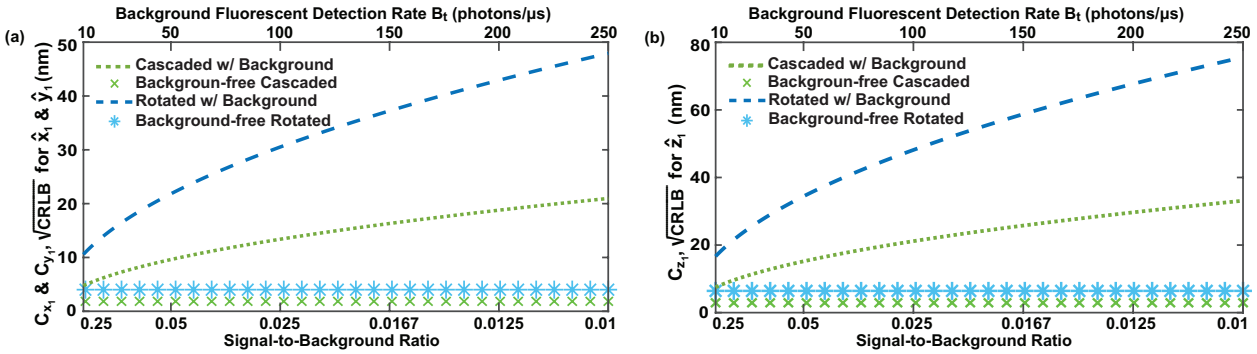

Figure 2.13: Comparing transverse and axial LBEStd for unbiasedly estimating the location of a single in-focus stationary molecule at $\boldsymbol{r}_1 = (0, 0, 0)$ via three-dimensional SPLM ($\lambda_{\text{ex}} = 500\,\text{nm}$. $t_c = 1\,\text{ms}$, $\text{NA} = 1.40$, $\text{RI} = 1.518$) with STM illumination (total expected photon detection count $= 5000/\text{emitter}$) with and without background emitters. Curves are plotted as functions of the background fluorescent detection rate as well as the signal-to-noise ratio (SBR) for the rotated method ($\alpha_{\text{sat}} = 0.26$, dashed for with background and $*$ for without background) and for the cascaded method ($\alpha_{\text{sat}} = 0.53$, dotted for with background and $\times$ for without background) (a) C_{x_1} and C_{y_1}. (b) C_{z_1}.

2.4.4 Three-dimensional Localization: Two Emitters

To determine the limit in spacing between emitters such that they may still be distinguished as two with a relatively high precision, we first consider evaluating the CRLB for unbiasedly estimating the locations of two emitters simultaneously without background. The two emitters are assumed to share the same photon emission and detection rates and located in the object region at $(-d/2, 0, 0)$ and $(d/2, 0, 0)$ or $(0, -d/2, 0)$ and $(0, d/2, 0)$ or $(0, 0, -d/2)$ and $(0, 0, d/2)$.

The general dependence of the CRLB for unbiasedly estimating the separation distance between the two emitters on their distance exactly follows that in the two-dimensional case due to the lack of nuisance parameters as shown in Fig. 2.14. The CRLB for unbiasedly estimating the emitter locations, on the other hand, show similar yet different behaviors due to the coupling and correlation between the transverse $x - y$ axes.

When the two emitters are separated by a sufficiently large distance along either direction, i.e. on the order of λ_{ex}, each LBEStd converges to some value higher than that in the single emitter case. Most of these values are approximately $\sqrt{2}$ times higher due to the increase in total shot noise, resulting in an decrease in the corresponding diagonal elements in the FIM. However, when the two emitters are located along either of the transverse x- or y-axis, the LBEStd for unbias-

edly estimating their y- or x-coordinates further degrades due to an increase in the corresponding off-diagonal elements in the FIM. The degradation of precision is worse when using the rotated STM illumination method due to the almost identical spatial frequency modulation along one of the transverse directions for both emitters, which increases the off-diagonal elements in the FIM, $J_{u(3+u)}$ and $J_{(3+u)u}$, such that they become almost equivalent in values as the diagonal elements, J_{uu} and $J_{(3+u)(3+u)}$. This degeneracy can be mitigated by coupling the transverse $x-y$ information, for example, by increasing the saturation level so that the sensitivity of the observed data about one of the transverse axes in which the emitter locations differ can provide differentiation for

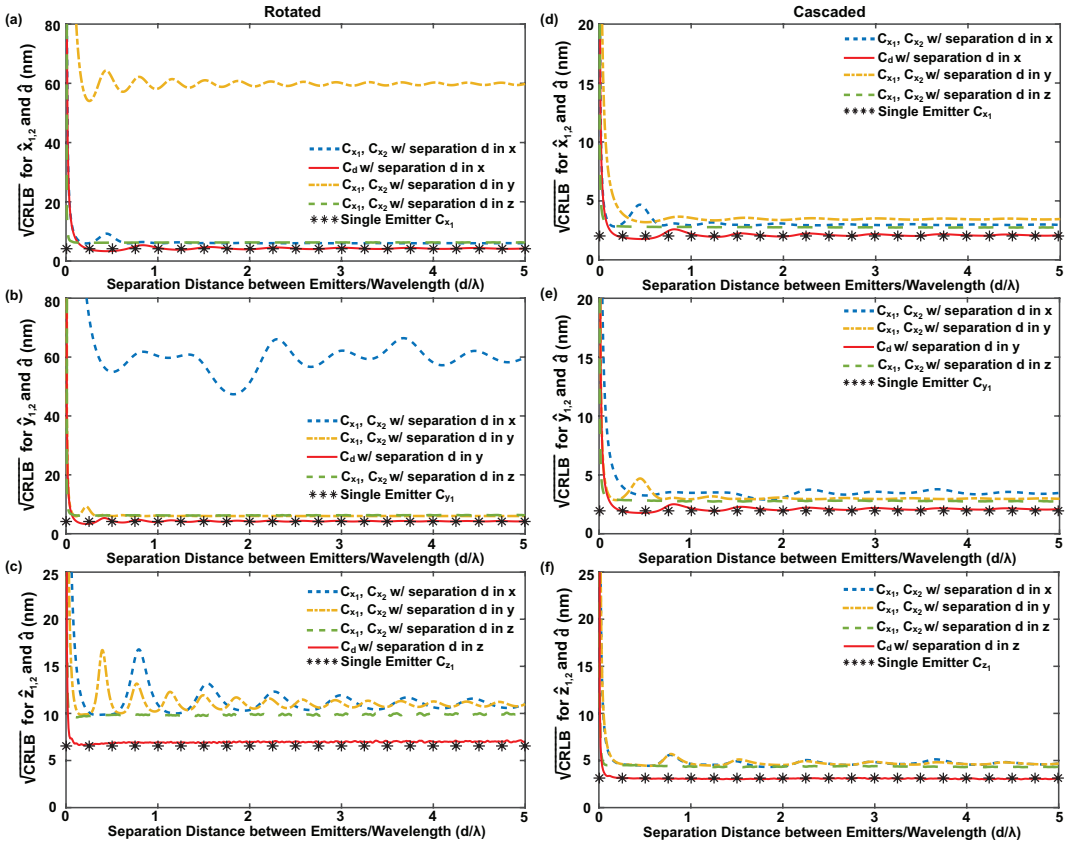

Figure 2.14: LBEStd for unbiasedly estimating the locations of two stationary fluorescent emitter and their separation distance in three-dimensional background-free SPLM ($\lambda_{\text{ex}} = 500\,\text{nm}$, $t_c = 1\,\text{ms}$, $\text{NA} = 1.40$, $\text{RI} = 1.518$) with STM illumination (total expected photon detection count $= 5000/\text{emitter}$) as functions of the separation distance d. (a), (b), (c) $C_{x_{1,2}}$, $C_{y_{1,2}}$, and $C_{z_{1,2}}$ with emitters separated along x- (dotted), y- (dash-dotted), and z-axis (dashed) using rotated method ($\alpha_{\text{sat}} = 0.26$). C_d (solid) with emitters separated along x-, y-, and z-dimension respectively. Reference LBEStd ($*$) under the same experimental parameter values for the location of a single in-focus stationary emitter. (d), (e), (f) Same LBEStd using cascaded method ($\alpha_{\text{sat}} = 0.53$).

the shared emitter coordinates. That is why such increases in the off-diagonal elements when the two emitters are located along the x- or y-axis are much less with the cascaded STM illumination method.

When the separation distance between two emitters is less than approximately $0.05\,\lambda_{\mathrm{ex}}$ with the rotated method or $0.04\,\lambda_{\mathrm{ex}}$ with the cascaded method, the pair of emitters can no longer be differentiated as two individual emitters. Eventually, the LBEStd diverges to infinity.

2.4.5 Three-dimensional Localization: Multiple Emitters

The expanded localization volume SPLM with STM illumination may achieve presents a new challenge from the increase in the number of fluorophores detected simultaneously. While the expanded volume brings additional capabilities, the increased shot noise from more fluorophores of interest will negatively impact the localization precision.

To evaluate LBEStd for many fluorescent emitters unbiasedly localized in a volume, we simulate the locations of a number of fluorescent molecules, N, which are randomly located in an ellipsoid centered at the origin in the object region with a minimum distance of $0.1\,\lambda_{\mathrm{ex}}$. The size of the ellipsoid is determined by the excitation beam width and the DOF that STM illumination may consequently achieve. Assuming a Gaussian profile of the illumination beam with width of $57\,\mu$m in the object region, the principal diameters of the ellipsoid along the transverse $x-y$ axes are equivalent to the Gaussian width while the principal diameter along the axial z-axis is chosen to be $50\,\mu$m, which has full spatial frequency support, to simulate a dense labelling scenario, and $500\,\mu$m to simulate an increased labeling sparsity. Randomization in choosing emitter locations is to ensure an extremely low possibility that any two emitters will share the same coordinate along or parallel to the transverse $x-y$ axes, which may lead to unwanted correlations among location parameters. For each illumination method, we performed 1000 calculations of randomly selected emitter positions to capture a possible range of precision limit that may occur as a result of emitter proximity. The minimum distance ensures that the correlation among location coordinates is kept at a suitable level.

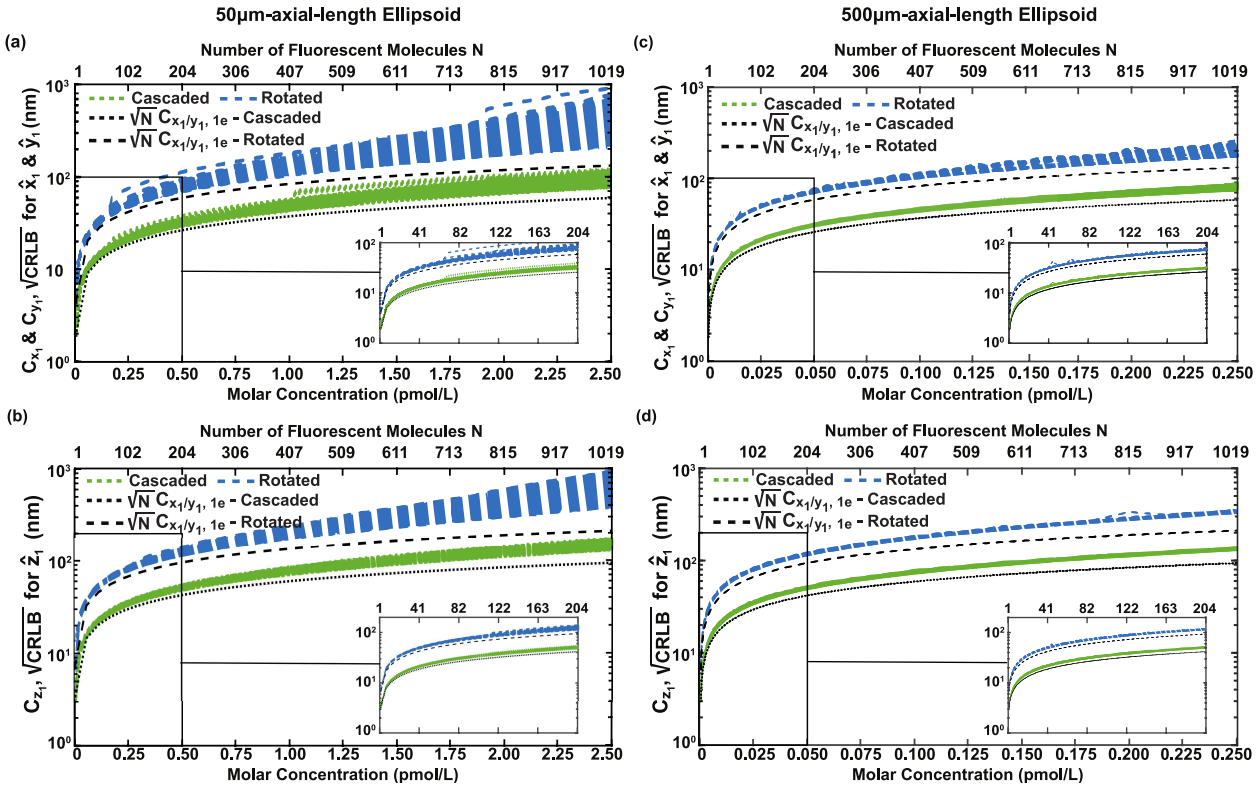

Figure 2.15: LBEStd for simultaneously estimating the locations of multiple emitters in three-dimensional background-free SPLM ($\lambda_{\text{ex}} = 500\,\text{nm}$, $t_c = 1\,\text{ms}$, $\text{NA} = 1.40$, $\text{RI} = 1.518$) with STM illumination (total expected photon detection count $= 5000/\text{emitter}$) using rotated method (dashed) and cascaded method (dotted) as functions of the molar concentration as well as the number of emitters. (a), (b) C_{x,y_1} and C_{z_1} in dense labeling scenario with reference LBEStd (black dashed for rotated and black dotted for cascaded). (c), (d) Same LBEStd in sparse labeling scenario.

The LBEStd are plotted as functions of the the molar concentration and the number of fluorescent molecules in Fig. 2.15 with a mean photon detection count of 5000 photons per emitter. The cascaded method shows advantages over the rotated method in both sparse and dense labeling scenarios as not only the LBEStd are much lower under the same number of emitters due to the information coupling between the transverse $x - y$ plane, but their ranges are much smaller due to a much lower probability of two emitters being strongly correlated in a confined space.

Also plotted are reference curves for LBESTd to localize multiple fluorescent molecules assuming there is no correlation among all emitters, or equivalently, the Fisher information matrix is nearly diagonal. We chose to denote the reference curves as $\sqrt{N}\,C_{q_1,1e}$, where N is the number of fluorescent molecules of interest and $C_{q_1,1e}$ is the LBEStd for unbiasedly estimating the emitter

location along q-dimension for the localization of a single emitter, which is further approximated via Eqs. (2.44), (2.45) ,and (2.46). Compared with the reference curves, the LBEStd mainly depends on the number of fluorescent molecules to be simultaneously estimated. Especially with a relatively low number of emitters, the average LBEStd's between the sparse and dense labelling scenarios are similar in values. As the number of fluorescent molecules increases, the probability that the emitter locations are correlated also increases such that the LBEStd may be raised much higher than the reference curves. This is the reason why the ranges of the LBEStd is greater and the average LBEStd is higher in the dense labeling scenario and/or when using the rotated method.

Moreover, we may infer upper bounds of the molar density for which the FIM can be considered as nearly diagonal by considering that if the average LBEStd for unbiasedly localizing multiple emitters simultaneously are within 15% increase from the reference LBEStd, then they can be roughly approximated by the reference. Thus, when the molar density is less than 15 fmol/L using the rotated method, the resulting increase in the average LBEStd is less than 4 nm from the reference along the transverse directions and 8 nm along the axial direction. When the molar density is less than 30 fmol/L using the cascaded method, the resulting increase in the average LBEStd is less than 3 nm from the reference along the transverse directions and 6 nm along the axial direction.

Regardless of how correlated the emitter locations are, SPLM with STM illumination offers the potential to observe high-speed translational dynamics of the fluorescent probes over a large volume with a relatively high precision. To give a specific example, the average LBEStd for estimating the location of 500 emitters jointly in both sparse and dense labeling scenarios is approximately 80 nm for the transverse coordinates and 140 nm for the axial coordinates when using the cascaded method.

2.4.6 Comparison with Camera-based Methods

Most SMLM methods use camera-based detectors, in which case the localization precision is fundamentally limited by the number of photons detected from the fluorescent molecules of interest, assuming that there is no overlap among their PSFs [41]. It is interesting to compare the CRLB

for localizing a single fluorescent emitter using camera-based LM methods and three-dimensional SPLM with STM illumination.

The camera-based method in comparison in Fig. 2.16 is 2-plane MUM with one focal plane at $0\,\mu$m and the other at $0.5\,\mu$m, which may achieve a DOF of approximately $2.5\,\mu$m [42]. For simulation purposes, we assume no background emitter, an emission wavelength of $520\,$nm, and an effective pixel size of each detector of $100\,$nm. The PSF follows a Gaussian function with an approximated standard deviation [43]. The photon detection rates are assumed equal between the two detectors. The experimental parameters that are not specified have the same values as those in SPLM with STM illumination. The FI using any camera-based method are given by [42, 44, 45],

$$\boldsymbol{J}_{\mathrm{cam}}(\boldsymbol{\theta}) = \sum_{j} \sum_{k=1}^{K} \frac{1}{\mu_{\boldsymbol{\theta},k} + B_k} \cdot \left(\frac{\partial \mu^j_{\boldsymbol{\theta},k}}{\partial \boldsymbol{\theta}} \right)^T \left(\frac{\partial \mu^j_{\boldsymbol{\theta},k}}{\partial \boldsymbol{\theta}} \right), \tag{2.49}$$

where K is the total pixel count of the detector, B_k denotes the mean photon count detected from the background emitters, and $\mu^j_{\boldsymbol{\theta},k}$ denotes the Poisson rate parameter for which the number of photons in the k-th pixel on the j-th detection plane or image is detected. $\mu^j_{\boldsymbol{\theta},k}$ is PSF-dependent and defined for the fluorescent molecule located at (x_1, y_1, z_1) as

$$\mu^j_{\boldsymbol{\theta},k} = \frac{\mathscr{N}_m}{M^2} \int_{G_k} \frac{\left| \mathrm{PSF}_{z_1^j} \left(\sqrt{\left(\frac{x}{M} - x_1^j\right)^2 + \left(\frac{y}{M} - y_1^j\right)^2} \right) \right|^2}{\int_{\mathbb{R}^2} \left| \mathrm{PSF}_{z_1^j} \left(\sqrt{\left(\frac{x}{M} - x_1^j\right)^2 + \left(\frac{y}{M} - y_1^j\right)^2} \right) \right|^2 dx\, dy} dx\, dy, \tag{2.50}$$

where M denotes the total magnification of the imaging system, G_k denotes the area of the k-th pixel, and the PSF varies with respect to the emitter axial position.

According to Fig. 2.16, three-dimensional SPLM with either STM illumination method carries a greater amount of information about the emitter axial coordinate under the same photon budget. When using the cascaded STM illumination method, SPLM demonstrates an advantage in unbiasedly estimating the emitter transverse location as well, especially under a limited photon budget.

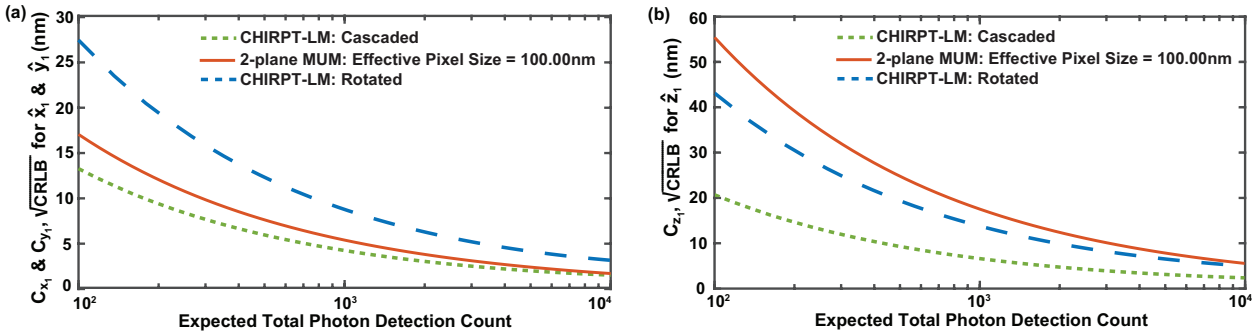

Figure 2.16: LBEStd for unbiasedly estimating the location of a single stationary in-focus fluorescent molecule at $\boldsymbol{r}_1 = (0, 0, 0)$ from three-dimensional SPLM ($\lambda_{\text{ex}} = 500\,\text{nm}$, $t_c = 1\,\text{ms}$, $\text{NA} = 1.40$, $\text{RI} = 1.518$) with STM illumination using rotated method (dashed) and cascaded method (dotted) as compared to 2-plane MUM ($\lambda_{\text{em}} = 520\,\text{nm}$, effective pixel size $= 100\,\text{nm}$) (solid) as functions of the total expected photon detection count. (a) C_{x_1} and C_{y_1}. (b) C_{z_1}.

Moreover, the main advantage of STM illumination is its large DOF, which is 100's μm with full spatial frequency support as compared to $< 10\,\mu$m that is common in MUM. The imaging depth using MUM is partially limited due to the fact that the DOF is gained via the addition of focal planes and thus, the total amount of photons detected is split among multiple detectors. Consequently, the information of emitter locations decreases as the emitter is positioned farther away from the detectors. In comparison, DOF in 3D STM illumination is determined by the overlapping region of the two first-order beams along the modulation axes, which varies with respect to time as the first-order beams scan across the back aperture. This temporal dynamic allows for fractions of the spatial frequency modulations to be projected onto an emitter that is far away from the focal plane and therefore, a much larger DOF on the order of $10\,\text{mm}$ can be achieved with the lower bounds on error standard deviation for unbiasedly estimating the emitter location scaled by its absolute axial position outside of the full spatial frequency support region.

The trade-off between the localization DOF and the lower bounds of precision exist in almost all LM methods. Thus, to further compare the CRLB between SPLM and camera-based SMLM, we plot the transverse and axial LBEStd as functions of a single emitter z-position in Fig. 2.17 with background fluorescent emitters. The camera-based LM method in comparison is the Tetrapod PSF, which is optimized for a DOF of $\pm 3\,\mu$m and $\pm 10\,\mu$m, meaning that the CRLB diverges rapidly outside of its design range [37, 38]. For plotting purposes, we assume 5000 photons are

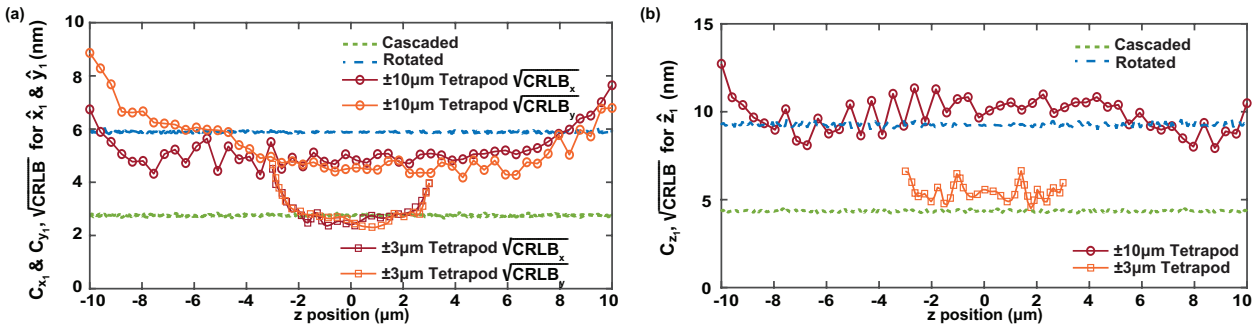

Figure 2.17: Comparison of the LBEStd for unbiasedly estimating the location parameters of a single stationary fluorescent molecule at $\boldsymbol{r}_1 = (0, 0, z)$ using three-dimensional SPLM ($\lambda_{\text{ex}} = 500\,\text{nm}$. $t_c = 1\,\text{ms}$, $\text{NA} = 1.40$, $\text{RI} = 1.518$) with STM illumination (total expected photon detection count $= 5000/\text{emitter}$) via the rotated method (dotted) and the cascaded method (dashed), and the Tetrapod PSF ($\lambda_{\text{em}} = 520\,\text{nm}$, effective pixel size $= 143\,\text{nm}$) with a background fluorescent rate of 20 photons/pixel. The localization CRLB calculations using the Tetrapod PSF were provided by Boris Ferdman at Technion - Israel Intitue of Technology, with masks optimized for a DOF of $\pm 3\,\mu$m (line with $\square$) and $\pm 10\,\mu$m (line with $\circ$). (a) C_{x_1} and C_{y_1}. (b) C_{z_1}.

expected to be detected from the fluorescent molecule. For Tetrapod PSF, the effective pixel size is $143\,\text{nm}$ and the expected background signal per pixel B_p is 20 photons, which can be related to the background fluorescent rate in SPLM as $B_t = N_x\, N_y\, B_p/\Delta t_i$, where N_x and N_y as the numbers of pixels per row and column of the FOV and Δt_i as the camera integration time. To match SPLM, the rest of the experiment parameters are set to be the same. These calculations were provided by Boris Ferdman at Technion - Israel Institute of Technology.

LBEStd via Tetrapod PSF optimized for $\pm 3\,\mu$m is comparable to three-dimensional SPLM with STM illumination using the cascaded method while Tetrapod PSF optimized for $\pm 10\,\mu$m carries a similar amount of information content about the emitter location as compared to three-dimensional SPLM with STM illumination using the rotated method. Certainly, SPLM with STIM illumination has a much larger localization DOF.

Therefore, unlike camera-based LM techniques, such as MUM or engineered PSFs, which rely on the addition of focal planes or distortions of the PSF to gain DOF and consequently, compensate the localization CRLB, the DOF of SPLM with STM illumination does not affect the localization CRLB much within its full spatial frequency support, which extends to 100's μm and thus, is relatively constant.

2.5 Conclusion

By computing CRLB, we have quantified the effects of different experimental parameters, such as the illumination objective lens NA, the fluorescence emission rate, the saturation parameter, the background emitter level, and the number of emitters within the localization volume, on the lower bound on error standard deviation (LBEStd) for the unbiased parameters of the emitter location(s). These analyses reveal the following properties of SPLM. The larger the transverse spatial frequencies in the illumination field, the lower the CRLB and thus, a higher localization precision may be achieved. For a reasonable range of saturation levels ($\alpha_{\mathrm{sat}} < 1.50$), an increase in the saturation level corresponds to an increase in the information due to the increase in the excited state population and consequently, detected photons within the given detection window. In three-dimensional SPLM, an increase in saturation also couples the information between the transverse axe and thus, improves the transverse CRLB. Such coupling in information can extend intrinsically from modulation design, like in the cascaded method where the modulations of spatial frequencies along both transverse x- and y-axes are simultaneous and introduce a much greater information coupling effect as compared to saturation. Not only does it increase the amount of information the signal carries about each of the transverse axes, it also helps reduce the correlation between them.

Moreover, via FIM, we determined the conditions when it can be considered nearly diagonal so that the CRLB for unbiasedly estimating u^{th} location parameter of the l^{th} emitter can be approximated by the inverse of the $\left(n\left(l-1\right)+u\right)^{\mathrm{th}}$ diagonal element of the Fisher information matrix. These conditions, when applying STM illumination patterns used in and inspired by CHIRPT microscopy, include a minimum separation distance between emitters on the order of λ_{ex}, $\mathrm{NA}/\mathrm{RI} \gtrsim 0.9$, as well as a maximum molar density, when it comes to three-dimensional SPLM, of $15\,\mathrm{fmol/L}$ via the rotated method and $30\,\mathrm{fmol/L}$ via the cascaded method. We have reached such conclusions under the assumption that the photon emission and detection rates among emitters are the same. For the localization of a single emitter in three-dimensional SPLM with STM illumination, the CRLB for unbiasedly estimating each location parameter within the full spatial frequency support can be further approximated in terms of the experimental parameters using Eqs.

(2.44), (2.45), and (2.46). These approximate expressions are validated through comparisons to the exact analyses of the corresponding lower bounds on error standard deviation (LBEStd). In two-dimensional SPLM with STM illumination, the dependence of the CRLB on the objective lens NA and the saturation parameter α_{sat} still follows the approximate expressions as specified in Eqs. (2.42) and (2.43). However, these approximate expressions do not take into account of the time-varying fringe visibility function $\mu(t)$ that arises from the energy apodization of the diffracted beam when scanning across the back aperture and therefore, the actual CRLB values slightly deviate. For multiple emitters (N), the localization CRLB of each emitter within the full spatial frequency support region of SPLM with STM illumination can be approximated by scaling the CRLB for the localization of single emitter by N. We have also shown that even when correlations among emitter location parameters exist, the LBEStd for unbiasedly localization hundreds of emitters is expected to be in the 10's and low 100's nm.

Lastly, CRLB also helped us evaluate the information content that SPLM with STM illumination carries across its large DOF. In the region with full spatial frequency support that is 100's μm deep, the LBEStd are limited by the number of photons detected per emitter. Because of the unique temporal dynamic of spatial frequency modulation projected onto the object region when using STM illumination, localization of emitters can be extended beyond the region with full spatial frequency support to 10's mm and the LBEStd is scaled with the emitter's z-position approximately linearly.

Chapter 3

Misspecified Cramér-Rao Bound (MCRB) with Poisson Statistics and its Application in Localization Microscopy (LM)

3.1 Introduction

This chapter is based on work that has been accepted for publication in Optics Letter: "Misspecified Cramér–Rao Lower Bound with Poisson Statistics and its Application in Localization Microscopy" by Maxine Varughese et al.

The CRLB establishes a fundamental limit on the precision of any unbiased estimation and is widely applied in optical measurements, including localization microscopy (LM) [14, 44, 46–49], diffuse optical tomography (DOT) [50, 51], and interferometry such as optical coherence tomography (OCT) [52] and ptychography [53]. It informs high-resolution imaging system design, optical instrument calibration, and material characterization. However, the CRLB assumes perfect knowledge of the data model —— an idealization often violated in practice due to calibration errors, misalignment, or optical aberrations. To account for mismatched models, the Misspecified Cramér-Rao Bound (MCRB) was developed and primarily applied under a Gaussian model [15–20]. It provides a lower bound on the error covariance of any estimator that is unbiased with respect to the "pseudo-true" parameters —— those to which the estimator converges under the misspecified model.

This chapter extends the MCRB formulation to a Poisson noise model, which more accurately reflects the statistics of photon-limited optical measurements. We apply this framework to two LM methods: Single-Pixel Localization Microscopy (SPLM) with Spatio-Temporally Modulated illuminations (STM) [14] and Single Molecule Localization Microscopy (SMLM) [5–8]. We analyze precision changes under mismatched aberration powers —— specifically, first- and second-order

components —– between the presumed and true models of single-emitter signals. These correspond to a mismatch in the point spread function (PSF) for SMLM or in the location-specific temporally modulated illumination patterns for SPLM. We focus on the single-emitter case as the effect of mismatched aberration powers is independent across emitters. Higher-order aberration mismatch is computationally more intensive due to the lack of a closed-form expression for the pseudo-true emitter location.

To evaluate the impact of using an idealized (aberration-free) signal model in the presence of aberrations, we compute the MCRB and the lower bound on the mean squared error (MSELB), and compare them to the CRLB under the aberrated yet fully characterized model as well as the aberration-free scenario. These comparisons quantify the resulting change in localization precision due to model mismatch.

It is important to note that the mathematical notations adopted for the CRLB and MCRB analyses may differ across sections. These differences are intentional and serve several purposes: they preserve internal consistency within each framework that is mathematically involved and reflect the distinct assumptions underlying well-specified versus misspecified models. Where applicable, care is taken to define variables locally and maintain conceptual continuity between the two analyses.

3.2 Background

This section provides the detailed mathematical derivations for the misspecified Cramér-Rao Lower Bound (MCRB) under mismatched Poisson point processes and its application in two types of localization microscope (LM) methods —- Single Pixel Localization Microscope (SPLM) with Spatio-Temporally Modulated illuminations (STM) and Single Molecule Localization Microscopy (SMLM) with mismatched aberration powers in tilt and defocus aberrations.

3.2.1 General MCRB Derivation with Mismatched Poisson Processes

Let $\boldsymbol{N} \in \mathbb{R}^k$ be a random vector, each of its element is independent and identically distributed (i.i.d.) as an observation recorded in the experiment, e.g. photon count detected in one time interval of a single-pixel camera or on one pixel of an array camera. With the shot-noise-limit assumption, the true probability density function (PDF) of the joint process is given by

$$f(\boldsymbol{N};\boldsymbol{\theta}_0) = \prod_k \frac{\nu_k(\boldsymbol{\theta}_0,\boldsymbol{c}_0)^{n_k}}{n_k!} e^{-\nu_k(\boldsymbol{\theta}_0,\boldsymbol{c}_0)}, \tag{3.1}$$

where the Poisson rates are functions of the parameters of interest $\boldsymbol{\theta}$ and the uncertainty parameters $\boldsymbol{c}$ at their true values $\boldsymbol{\theta}_0$ and $\boldsymbol{c}_0$ respectively. The uncertainty parameters capture any incomplete knowledge about the experiment, e.g. aberration powers, besides the parameters of interest.

When the uncertainty parameter values deviate from the true ones in reconstruction or estimation, the data are presumed fitted to a mismatched statistical model, i.e.

$$p(\boldsymbol{N};\boldsymbol{\theta}) = \prod_k \frac{\nu_k(\boldsymbol{\theta},\tilde{\boldsymbol{c}})^{n_k}}{n_k!} e^{-\nu_k(\boldsymbol{\theta},\tilde{\boldsymbol{c}})}, \tag{3.2}$$

where $\tilde{\boldsymbol{c}}_0$ holds different values than $\boldsymbol{c}_0$. Under the assumption that an interior point $\tilde{\boldsymbol{\theta}}_0$ exists in the parameter space such that it gives a unique maximum for $\mathrm{E}_p[\ln f(\boldsymbol{N};\boldsymbol{\theta})]$, it is shown that $\tilde{\boldsymbol{\theta}}_0$ also minimizes the Kullback-Leibler (KL) divergence between the true and presumed PDFs [18,54,55]. Therefore, as a measure to quantify the performance of the maximum likelihood (ML) estimator, the MCRB is defined with respect to misspecified (MS)-unbiased estimators $\tilde{\hat{\boldsymbol{\theta}}}$ and the pseudo-true parameter values $\tilde{\boldsymbol{\theta}}_0$ that they converge to [15, 16, 18],

$$\mathrm{cov}\left(\tilde{\hat{\boldsymbol{\theta}}}, \tilde{\boldsymbol{\theta}}_0\right) \geq \boldsymbol{A}_{\tilde{\boldsymbol{\theta}}_0}^{-1} \boldsymbol{B}_{\tilde{\boldsymbol{\theta}}_0} \boldsymbol{A}_{\tilde{\boldsymbol{\theta}}_0}^{-1} = \mathrm{MCRB}(\tilde{\boldsymbol{\theta}}_0), \tag{3.3}$$

where $\boldsymbol{A}_{\tilde{\boldsymbol{\theta}}_0}$ and $\boldsymbol{B}_{\tilde{\boldsymbol{\theta}}_0}$ are two generalizations of the Fisher information matrices under misspecified models. Each of their entries is given by

$$\begin{aligned}\left[\boldsymbol{A}_{\tilde{\boldsymbol{\theta}}_0}\right]_{ij} = \left\{\mathrm{E}_p\left[\nabla_{\boldsymbol{\theta}}\nabla_{\boldsymbol{\theta}}^T \ln f\left(\boldsymbol{N};\boldsymbol{\theta}\right)\right]\big|_{\boldsymbol{\theta}=\tilde{\boldsymbol{\theta}}_0}\right\}_{ij} = \sum_k \left(\frac{\nu_k(\boldsymbol{\theta}_0,\boldsymbol{c}_0)}{\nu_k(\boldsymbol{\theta},\tilde{\boldsymbol{c}})} - 1\right) \frac{\partial^2}{\partial\theta_i\partial\theta_j}\nu_k(\boldsymbol{\theta},\tilde{\boldsymbol{c}})\bigg|_{\boldsymbol{\theta}=\tilde{\boldsymbol{\theta}}_0} \\ - \sum_k \frac{\nu_k(\overline{\boldsymbol{\theta}}_0,\boldsymbol{c}_0)}{\left(\nu_k(\boldsymbol{\theta},\tilde{\boldsymbol{c}})\right)^2}\frac{\partial}{\partial\theta_i}\nu_k(\boldsymbol{\theta},\tilde{\boldsymbol{c}})\,\frac{\partial}{\partial\theta_j}\nu_k(\boldsymbol{\theta},\tilde{\boldsymbol{c}})\bigg|_{\boldsymbol{\theta}=\tilde{\boldsymbol{\theta}}_0},\end{aligned} \tag{3.4}$$

and

$$\begin{aligned}\left[\boldsymbol{B}_{\boldsymbol{\theta}_0}\right]_{ij} &= \left\{\mathrm{E}_p\left[\nabla_{\boldsymbol{\theta}} \ln f\left(\boldsymbol{N};\boldsymbol{\theta}\right)\nabla_{\boldsymbol{\theta}}^T \ln f\left(\boldsymbol{N};\boldsymbol{\theta}\right)\right]\big|_{\boldsymbol{\theta}=\tilde{\boldsymbol{\theta}}_0}\right\}_{ij} \\ &= \sum_k \frac{\nu_k(\boldsymbol{\theta}_0,\boldsymbol{c}_0) + \left(\nu_k(\boldsymbol{\theta}_0,\boldsymbol{c}_0) - \nu_k(\boldsymbol{\theta},\tilde{\boldsymbol{c}})\right)^2}{\left(\nu_k(\boldsymbol{\theta},\tilde{\boldsymbol{c}})\right)^2}\frac{\partial}{\partial\theta_i}\nu_k(\boldsymbol{\theta},\tilde{\boldsymbol{c}})\frac{\partial}{\partial\theta_j}\nu_k(\boldsymbol{\theta},\tilde{\boldsymbol{c}})\bigg|_{\boldsymbol{\theta}=\tilde{\boldsymbol{\theta}}_0}.\end{aligned} \tag{3.5}$$

Moreover, the pseudo-true parameter, the minimizer of the KL divergence between the true and presumed statistical models, is given by

$$D_{\mathrm{KL}}(p\|f) = \mathrm{E}_p\left[\ln\frac{p(\boldsymbol{N};\boldsymbol{\theta}_0)}{f(\boldsymbol{N};\boldsymbol{\theta})}\right] = \sum_k v_k(\boldsymbol{\theta}_0,\boldsymbol{c}_0)\,\ln\frac{v_k(\boldsymbol{\theta},\tilde{\boldsymbol{c}})}{v_k(\boldsymbol{\theta}_0,\boldsymbol{c}_0)} - v_k(\boldsymbol{\theta}_0,\boldsymbol{c}_0) + v_k(\boldsymbol{\theta},\tilde{\boldsymbol{c}}). \tag{3.6}$$

When the presumed statistical model $p(\boldsymbol{N};\boldsymbol{\theta})$ matches the true PDF, i.e. $v_k(\boldsymbol{\theta}_0,\boldsymbol{c}_0) = v_k(\tilde{\boldsymbol{\theta}}_0,\tilde{\boldsymbol{c}})$ for all measurements, $\boldsymbol{A}_{\tilde{\boldsymbol{\theta}}_0}$ and $\boldsymbol{B}_{\tilde{\boldsymbol{\theta}}_0}$ become the Fisher information matrices in the standard definition. Consequently, the MCRB becomes the conventional CRLB.

3.2.2 Probabilistic Models in SPLM and SMLM Measurements

In SPLM, the expected number of photons detected at time t_k, which is the rate of the k^{th} Poisson point process, $\nu_k(\boldsymbol{\theta},\boldsymbol{c})$, can be expressed by $\mathscr{N}_m\,\overline{I}_{\boldsymbol{\theta}}(t_k,\boldsymbol{c})$, where $\mathscr{N}_m$ denotes the maximal mean photon detection rate for the entire signal and $\overline{I}_{\boldsymbol{\theta}}(\cdot)$ is the illumination intensity normalized to unity

in space an time. The true joint probability of photon detection is then

$$f_{\mathrm{SPLM}}(\boldsymbol{N};\boldsymbol{\theta_0}) = \prod_k \frac{\left(\mathscr{N}_m\,\overline{I}_{\boldsymbol{\theta}_0}(t_k,\boldsymbol{c}_0)\right)^{n_k}}{n_k!} e^{-\mathscr{N}_m\,\overline{I}_{\boldsymbol{\theta}_0}(t_k,\boldsymbol{c}_0)}. \tag{3.7}$$

Under the mismatched condition assuming that there are no aberrations, the presumed joint probability of photon detection becomes

$$p_{\mathrm{SPLM}}(\boldsymbol{N};\boldsymbol{\theta}) = \prod_k \frac{\left(\mathscr{N}_m\,\overline{I}_{\boldsymbol{\theta}}(t_k,\boldsymbol{0})\right)^{n_k}}{n_k!} e^{-\mathscr{N}_m\,\overline{I}_{\boldsymbol{\theta}}(t_k,\boldsymbol{0})}. \tag{3.8}$$

The challenge with the MCRB analyses for any camera-based LM method is that a closed-form expression for the point spread function (PSF) does not always exist, especially with higher-order aberrations. Under the Gaussian beam and Fresnel approximation, the 3D PSF, normalized to unit integral over the transverse image plane, is given by, up to second-order aberrations,

$$\begin{aligned}\overline{\mathrm{PSF}}_{\boldsymbol{\theta}}(\boldsymbol{\rho},\boldsymbol{c}) =& \frac{1}{\pi\sqrt{\left(\frac{1}{4\,\pi^2\,f_c^2}+f_c^2\left(\frac{z_0}{f}-2\,c_2^x\right)^2\right)\left(\frac{1}{4\,\pi^2\,f_c^2}+f_c^2\left(\frac{z_0}{f}-2\,c_2^y\right)^2\right)}} \\ &\times e^{-\left(\frac{(x-x_0-c_1^x)^2}{\frac{1}{4\,\pi^2\,f_c^2}+f_c^2\left(\frac{z_0}{f}-2\,c_2^x\right)^2}+\frac{(y-y_0-c_1^y)^2}{\frac{1}{4\,\pi^2\,f_c^2}+f_c^2\left(\frac{z_0}{f}-2\,c_2^y\right)^2}\right)}.\end{aligned} \tag{3.9}$$

Consequently, the true and presumed joint PDFs of detecting a number of photons across all pixels on a camera take similar forms as Eqs. 3.7 and 3.8,

$$f_{\mathrm{SMLM}}(\boldsymbol{N};\boldsymbol{\theta}) = \prod_k \frac{\left(\mathscr{N}_m^{\mathrm{cam}}\int_{\Delta p}\overline{\mathrm{PSF}}\left([x_k,y_k]+\boldsymbol{d},\boldsymbol{c}_0\right)d^2\boldsymbol{d}\right)^{n_k}}{n_k!} e^{-\mathscr{N}_m^{\mathrm{cam}}\int_{\Delta p}\overline{\mathrm{PSF}}([x_k,y_k]+\boldsymbol{d},\boldsymbol{c})d^2\boldsymbol{d}}, \tag{3.10}$$

and

$$p_{\mathrm{SMLM}}(\boldsymbol{N};\boldsymbol{\theta}) = \prod_k \frac{\left(\mathscr{N}_m^{\mathrm{cam}} \int_{\Delta p} \overline{\mathrm{PSF}}\left([x_k, y_k] + \boldsymbol{p}, \mathbf{0}\right) d^2\boldsymbol{p}\right)^{n_k}}{n_k!} e^{-\mathscr{N}_m^{\mathrm{cam}} \int_{\Delta p} \overline{\mathrm{PSF}}([x_k,y_k]+\boldsymbol{p},\mathbf{0}) d^2\boldsymbol{p}}, \tag{3.11}$$

where $\mathscr{N}_m^{\mathrm{cam}}$ denotes the maximal mean photon count detected across all pixels, $[x_k, y_k]$ is the starting position of the k-th pixel and Δp is the pixel size.

3.2.3 Detailed MCRB Derivation

Following the general derivation and the statistical models, the general MCRB for each transverse emitter location in SPLM is approximately given by, assuming that there is little to zero correlation among emitter coordinates,

$$\begin{aligned}
\mathrm{MCRB}(\tilde{\hat{p}}_0) = \frac{1}{4\,\pi^2 \mathscr{N}_m} \Bigg\{ \sum_k f_p^2(t_k) \Bigg[\left(\frac{\overline{I}_{\boldsymbol{\theta}_0}(t_k, \boldsymbol{c}_0)}{\overline{I}_{\tilde{\boldsymbol{\theta}}_0}(t_k, \mathbf{0})} - 1 \right) \cos\left(\Delta\Phi^p_{\tilde{\boldsymbol{\theta}}_0}(t_k, \mathbf{0})\right) \\
+ \frac{\overline{I}_{\boldsymbol{\theta}_0}(t_k, \boldsymbol{c}_0)}{\overline{I}^2_{\tilde{\boldsymbol{\theta}}_0}(t_k, \mathbf{0})} \sin^2\left(\Delta\Phi^p_{\tilde{\boldsymbol{\theta}}_0}(t_k, \mathbf{0})\right) \Bigg] \Bigg\}^{-1} \\
\times \sum_k f_p^2(t_k) \frac{\overline{I}_{\boldsymbol{\theta}_0}(t_k, \boldsymbol{c}_0) + \mathscr{N}_m \left(\overline{I}_{\boldsymbol{\theta}_0}(t_k, \boldsymbol{c}_0) - \overline{I}_{\tilde{\boldsymbol{\theta}}_0}(t_k, \mathbf{0})\right)^2}{\overline{I}^2_{\tilde{\boldsymbol{\theta}}_0}(t_k, \mathbf{0})} \sin^2\left(\Delta\Phi^p_{\tilde{\boldsymbol{\theta}}_0}(t_k, \mathbf{0})\right) \\
\times \Bigg\{ \sum_k f_p^2(t_k) \Bigg[\left(\frac{\overline{I}_{\boldsymbol{\theta}_0}(t_k, \boldsymbol{c}_0)}{\overline{I}_{\tilde{\boldsymbol{\theta}}_0}(t_k, \mathbf{0})} - 1 \right) \cos\left(\Delta\Phi^p_{\tilde{\boldsymbol{\theta}}_0}(t_k, \mathbf{0})\right) \\
+ \frac{\overline{I}_{\boldsymbol{\theta}_0}(t_k, \boldsymbol{c}_0)}{\overline{I}^2_{\tilde{\boldsymbol{\theta}}_0}(t_k, \mathbf{0})} \sin^2\left(\Delta\Phi^p_{\tilde{\boldsymbol{\theta}}_0}(t_k, \mathbf{0})\right) \Bigg] \Bigg\}^{-1},
\end{aligned} \tag{3.12}$$

where $\Delta\Phi^p_{\tilde{\boldsymbol{\theta}}_0}$ denotes the overall modulation phase for each transverse p-axis. The general MCRB for the axial emitter location in SPLM takes a similar form but has information contributed through

both transverse modulations. Its expression is approximately given by

$$\begin{aligned}\mathrm{MCRB}(\tilde{\hat{z}}_0) =& \frac{1}{4\,\pi^2\,\mathscr{N}_m}\left\{\sum_k\sum_p f_{z,p}^2(t_k)\left[\left(\frac{\overline{I}_{\boldsymbol{\theta}_0}(t_k,\boldsymbol{c}_0)}{\overline{I}_{\tilde{\boldsymbol{\theta}}_0}(t_k,\mathbf{0})}-1\right)\cos\left(\Delta\Phi^p_{\tilde{\theta}_0}(t_k,\mathbf{0})\right)\right.\right.\\ &\left.\left.+\ \frac{\overline{I}_{\boldsymbol{\theta}_0}(t_k,\boldsymbol{c}_0)}{\overline{I}^2_{\tilde{\boldsymbol{\theta}}_0}(t_k,\mathbf{0})}\sin^2\left(\Delta\Phi^p_{\tilde{\boldsymbol{\theta}}_0}(t_k,\mathbf{0})\right)\right]\right\}^{-1}\\ &\times\sum_k\sum_p f_p^2(t_k)\,\frac{\overline{I}_{\boldsymbol{\theta}_0}(t_k,\boldsymbol{c}_0)+\mathscr{N}_m\left(\overline{I}_{\boldsymbol{\theta}_0}(t_k,\boldsymbol{c}_0)-\overline{I}_{\tilde{\boldsymbol{\theta}}_0}(t_k,\mathbf{0})\right)^2}{\overline{I}^2_{\tilde{\boldsymbol{\theta}}_0}(t_k,\mathbf{0})}\sin^2\left(\Delta\Phi^p_{\tilde{\boldsymbol{\theta}}_0}(t_k,\mathbf{0})\right)\\ &\times\left\{\sum_k\sum_p f_{z,p}^2(t_k)\left[\left(\frac{\overline{I}_{\boldsymbol{\theta}_0}(t_k,\boldsymbol{c}_0)}{\overline{I}_{\tilde{\boldsymbol{\theta}}_0}(t_k,\mathbf{0})}-1\right)\cos\left(\Delta\Phi^p_{\tilde{\theta}_0}(t_k,\mathbf{0})\right)\right.\right.\\ &\left.\left.+\frac{\overline{I}_{\boldsymbol{\theta}_0}(t_k,\boldsymbol{c}_0)}{\overline{I}^2_{\tilde{\boldsymbol{\theta}}_0}(t_k,\mathbf{0})}\sin^2\left(\Delta\Phi^p_{\tilde{\boldsymbol{\theta}}_0}(t_k,\mathbf{0})\right)\right]\right\}^{-1}\end{aligned} \tag{3.13}$$

Further simplification and implications of the MCRB needs to be assessed with specific aberration power mismatches.

Due to the lack of general closed-form expression for the PSF with all orders of aberrations, the general expression of the MCRB in SMLM does not exist.

Tilt and Defocus in SPLM

When tilt and defocus aberrations are present in optical measurements, the true signal model in SPLM has an aberration phase as $\varphi_{\mathrm{ab},p}(\boldsymbol{c}_0,t) = e^{i\,2\,\pi\left(c_0^{1p}\,f_p(t)+c_0^2\,f_p^2(t)\right)}$ for each transverse p-axis. Therefore, the overall modulation phase for each transverse p-aixs without considering the Gaussian beam profile becomes

$$\Delta\Phi_p(\boldsymbol{\theta},t)+\varphi_{\mathrm{ab},p}(\boldsymbol{c},t) = 2\pi\left(\nu_{c,p}\,t+f_p(t)\left(p^{e0}+c_0^{1p}\right)-f_p^2(t)\left(\frac{z^{e0}}{f}-c_0^2\right)\right). \tag{3.14}$$

Assuming that there is no aberration in the data collected, $\varphi_{\mathrm{ab},p}(\mathbf{0},t)=0$, the KL divergence between the true and presumed PDFs, following Eq. 3.6, is minimized when $\nu_k(\boldsymbol{\theta}_0,\boldsymbol{c}_0)=\nu_k(\tilde{\boldsymbol{\theta}}_0,\mathbf{0})$ for all k, or equivalently, $\Delta\Phi_p(\boldsymbol{\theta}_0,t)+\varphi_{\mathrm{ab},p}(\boldsymbol{c}_0,t) = \Delta\Phi_p(\tilde{\boldsymbol{\theta}}_0,t)$ overlooking the effect of the

illumination Gaussian beam profiles for simplicity. The pseudo-true parameter values $\tilde{\theta}_0$ can be found at $\left[x^{e0} + c_0^{1x}, y^{e0} + c_0^{1y}, z^{e0} - 2\,f\,c_0^2\right]$. Since the tilt and defocus aberrations induce relative shifts in the illumination pattern relative to the detector, the phases and amplitudes resulted from the propagation of the Gaussian beams become matched in the true and presumed signal models with the same amount of shift in the pseudo-true parameter values as well. Therefore, the MCRB can be simplified as

$$\mathrm{MCRB}_{\mathrm{SPLM}}(\tilde{\hat{p}}_0) = \frac{1}{4\,\pi^2\,\mathscr{N}_m} \sum_k \frac{f_p^2(t_k)}{\overline{I}_{\tilde{\boldsymbol{\theta}}_0}(t_k, \mathbf{0})} \sin^2\left(\Delta\Phi^p_{\tilde{\boldsymbol{\theta}}_0}(t_k, \mathbf{0})\right) \approx \frac{2\,\mathrm{NA}^2\,t_c}{3\,\lambda_{\mathrm{ex}}^2\,\mathscr{N}_m}, \tag{3.15}$$

and

$$\mathrm{MCRB}_{\mathrm{SPLM}}(\tilde{\hat{z}}_0) = \frac{1}{4\,\pi^2\,\mathscr{N}_m} \sum_k \sum_p \frac{f_{z,p}^2(t_k)}{\overline{I}_{\tilde{\boldsymbol{\theta}}_0}(t_k, \mathbf{0})} \sin^2\left(\Delta\Phi^p_{\tilde{\boldsymbol{\theta}}_0}(t_k, \mathbf{0})\right) \approx \frac{4\,\mathrm{NA}^4\,t_c}{5\,\mathrm{RI}^2\,\lambda_{\mathrm{ex}}^2\,\mathscr{N}_m}, \tag{3.16}$$

They are the same as the conventional CRLB without any model mismatch, which are given by

$$\mathrm{CRLB}_{\mathrm{SPLM}}(\hat{p}_0) = \frac{1}{4\,\pi^2\,\mathscr{N}_m} \sum_k \frac{f_p^2(t_k)}{\overline{I}_{\boldsymbol{\theta}_0}(t_k, \boldsymbol{c}_0)} \sin^2\left(\Delta\Phi^p_{\boldsymbol{\theta}_0}(t_k, \boldsymbol{c}_0)\right), \tag{3.17}$$

and

$$\mathrm{CRLB}_{\mathrm{SPLM}}(\hat{z}_0) = \frac{1}{4\,\pi^2\,\mathscr{N}_m} \sum_k \sum_p \frac{f_p^2(t_k)}{\overline{I}_{\boldsymbol{\theta}_0}(t_k, \boldsymbol{c}_0)} \sin^2\left(\Delta\Phi^p_{\boldsymbol{\theta}_0}(t_k, \boldsymbol{c}_0)\right), \tag{3.18}$$

as $\overline{I}_{\boldsymbol{\theta}_0}(t_k, \boldsymbol{c}_0) = \overline{I}_{\tilde{\boldsymbol{\theta}}_0}(t_k, \mathbf{0})$ for all k.

However, the lower bound for the mean square error takes into the consideration of the bias as

$$\mathrm{MSE}_{\mathrm{SPLM}}(\tilde{\hat{p}}_0, p_0^{e0}) \geq \mathrm{CRLB}_{\mathrm{SPLM}}(\hat{p}_0) + \left(c_0^{1p}\right)^2, \tag{3.19}$$

$$\mathrm{MSE}_{\mathrm{SPLM}}(\tilde{\hat{z}}_0, z_0^{e0}) \geq \mathrm{CRLB}_{\mathrm{SPLM}}(\hat{z}_0) + 4\,f^2\left(c_0^2\right)^2. \tag{3.20}$$

Thus, the degradation in the lower bound for MSE results from the estimation bias introduced from the mismatched statistical models.

Tilt and Defocus in SMLM

Similarly, the PSF in SMLM when tilt and defocus aberrations are present is given by

$$\overline{\mathrm{PSF}}_{\boldsymbol{\theta}}(\boldsymbol{\rho}, \boldsymbol{c}_0) = \frac{1}{\pi \left(\frac{1}{4\,\pi^2\,f_c^2} + f_c^2 \left(\frac{z^{e0}}{f} - 2\,c_0^2 \right)^2 \right)} e^{-\frac{(x - x^{e0} - c_0^{1x})^2 + (y - y^{e0} - c_0^{1y})^2}{\frac{1}{4\,\pi^2\,f_c^2} + f_c^2 \left(\frac{z^{e0}}{f} - 2\,c_0^2 \right)^2}}. \tag{3.21}$$

When assuming there is no aberration, the KL divergence between the true and presumed statistical models is minimized when $\nu_k^{\mathrm{cam}}(\boldsymbol{\theta}_0, \boldsymbol{c}_0) = \nu_k^{\mathrm{cam}}(\tilde{\boldsymbol{\theta}}_0, \mathbf{0})$ for all k, or equivalently, $\overline{\mathrm{PSF}}_{\boldsymbol{\theta}_0}(\boldsymbol{\rho}, \boldsymbol{c}_0) = \overline{\mathrm{PSF}}_{\tilde{\boldsymbol{\theta}}_0}(\boldsymbol{\rho}, \mathbf{0})$. The pseudo-true parameter values $\tilde{\boldsymbol{\theta}}_0$ are found at $[x^{e0} + c_0^{1x}, y^{e0} + c_0^{1y}, z^{e0} - 2\,f\,c_0^2]$ as well. Therefore, the transverse MCRB becomes

$$\mathrm{MCRB}_{\mathrm{SMLM}}(\tilde{\hat{p}}) = \frac{1}{\pi\,N_m} \left(\sum_k \int_{\Delta\,p} \frac{2(p_k - \tilde{p}_0^{e0} + d_p)}{\frac{1}{4\,\pi^2\,f_c^2} + f_c^2 \left(\frac{\tilde{z}^{e0}}{f} \right)^2} \times \exp - \frac{(x_k - \tilde{x}_0^{e0} + d_x)^2 + (y_k - \tilde{y}^{e0} + d_y)^2}{\frac{1}{4\,\pi^2\,f_c^2} + f_c^2 \left(\frac{\tilde{z}^{e0}}{f} \right)} d^2\boldsymbol{d} \right)^{-1}, \tag{3.22}$$

while the axial MCRB also has a similar closed-form expression but is more complex. Since both expressions do not carry significant insights to the dependency of MCRB on experimental parameters, only the transverse MCRB formula is provided.

Like the MCRB in SPLM, since the true and presumed PSFs coincide, the MCRB is the same as the CRLB. However, the lower bound for the mean squared error accounts for the bias and thus,

$$\mathrm{MSE}_{\mathrm{SMLM}}(\tilde{\hat{p}}_0, p_0^{e0}) \geq \mathrm{CRLB}_{\mathrm{SMLM}}(\hat{p}_0) + \left(c_0^{1p} \right)^2, \tag{3.23}$$

$$\mathrm{MSE}_{\mathrm{SMLM}}(\tilde{\hat{z}}_0, z_0^{e0}) \geq \mathrm{CRLB}_{\mathrm{SMLM}}(\hat{z}_0) + 4\,f^2\left(c_0^2\right)^2. \tag{3.24}$$

The degradation in the lower bound for MSE is also characterized by the bias alone.

3.3 Illustration of MCRB via Defocus in SMLM

To further elucidate the MCRB, we begin with the CRLB, which provides an MSELB between any unbiased estimator $\hat{\boldsymbol{\theta}}$ of the true parameters $\boldsymbol{\theta}_0$ [56]. The CRLB is asymptotically attained by the maximum likelihood (ML) estimator as sample size increases.

Unlike the CRLB that assumes the statistical model matching the experiment perfectly, the MCRB accounts for mismatch between the presumed and true statistical models —– common in practice due to misalignment, aberrations, or calibration errors. Fig. 3.1 summarizes three estimation scenarios: fully characterized (data and true model matched with aberrations), realistic (data with aberrations but ideal model without aberrations), and ideal (data and model matched without aberrations).

In the ideal and fully characterized cases, data and model match —- unbiased estimators such as ML converge to the true parameter value, and the CRLB defines the MSE limit. However, a full characterization is rarely feasible in practice.

In the mismatchedcase, data are acquired from the actual system (filled circle), but estimation is performed using the presumed model (unfilled square). Here, an unbiased estimator is one whose expected mean equals to the pseudo-true parameter $\tilde{\boldsymbol{\theta}}_0$, which minimizes the Kullback-Leibler (KL) divergence between the true and presumed models. The bias $\boldsymbol{b} = \tilde{\boldsymbol{\theta}}_0 - \boldsymbol{\theta}_0$ quantifies the deviation from the true value and contributes to the increase in MSELB.

Despite the model mismatch, the notion of unbiasedness relative to $\tilde{\boldsymbol{\theta}}_0$ allows for the derivation of a CRLB-like lower bound on the error covariance for any misspecified-unbiased (MS-unbiased) estimator $\hat{\tilde{\boldsymbol{\theta}}}$ [15, 18–20, 54, 55].

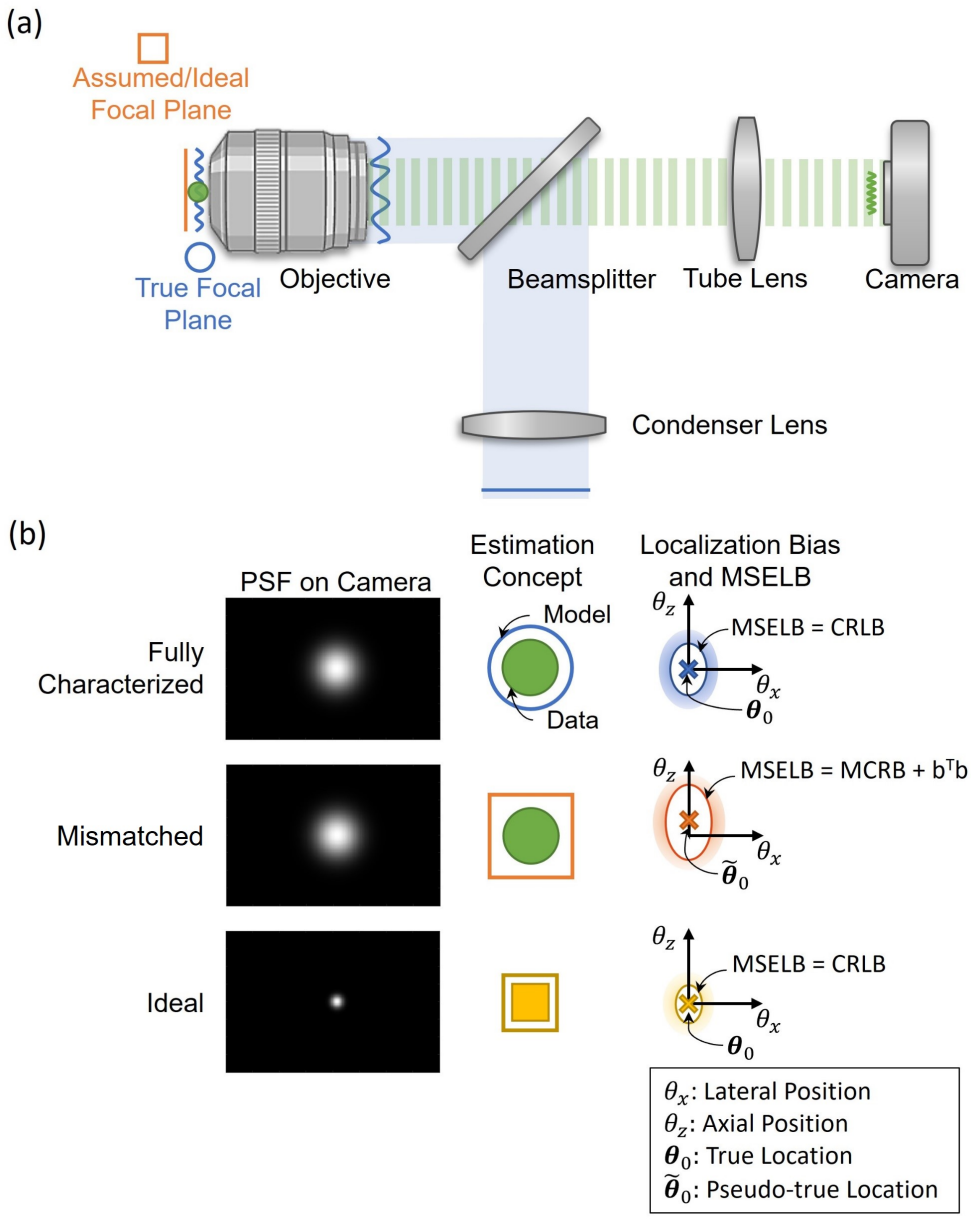

Figure 3.1: Illustration of a mismatch in defocus aberration power between the data collected and the presumed statistical model in SMLM (a) and its effect on the PSF, localization estimates, and the MSELB (b).

When $\tilde{\boldsymbol{\theta}}_0 = \boldsymbol{\theta}_0$, the estimator is consistent and the MSELB under misspecification reduces to the MCRB [18]. Generally, both variance and bias contribute to the MSELB,

$$\mathrm{MSE}(\hat{\tilde{\boldsymbol{\theta}}}, \boldsymbol{\theta}_0) \geq \mathrm{MCRB}(\tilde{\boldsymbol{\theta}}_0) + \boldsymbol{b}^T \boldsymbol{b}, \tag{3.25}$$

which provides a direct comparison to the CRLB as the difference between the pseudo-true and true parameters is bridged.

3.4 Numerical Evaluations of MCRB

To further investigate the implications of statistical model mismatch in practical imaging scenarios, we extend the analysis beyond the illustrative case of defocus in SMLM to systematic numerical evaluations of the MCRB in both SPLM and SMLM under a range of representative aberration conditions. Specifically, we examine how mismatches in optical models due to unmodeled tilt, defocus, and astigmatism affect the achievable localization precision. These aberrations, commonly encountered in experimental systems, introduce distortions in the illumination or detection model that deviate from the assumptions used during estimation. By quantifying the resulting degradation in precision via the MCRB, we aim to understand the relative sensitivity of SPLM and SMLM to such model inaccuracies and provide guidance on the robustness of each method in the presence of imperfect system knowledge.

While high NA objectives (≥ 1.2) are standard in super-resolution localization microscopy due to their superior photon collection and resolution capabilities, there are instances where lower NA objectives have been employed for cost-effective platforms [57] or deep tissue imaging [58]. In our study, we employ an objective of $\mathrm{NA} = 0.60$ in the MCRB and CRLB calculations primarily to illustrate how the lower bound of the error covariance changes under different aberration conditions. The excitation intensity is chosen so that the total expected photon detected is around 270. The broader PSF associated with a lower NA enhances the observable impact of statistical mismatches, making it well-suited for demonstrating differences between ideal and misspecified models in both transverse and axial dimensions.

3.4.1 Tilt and Defocus

Aberrations such as tilt and defocus can induce a relative shift in the modulation pattern or PSF with respect to the detector, resulting in biased emitter localization. However, under proper

definitions of unbiasedness in the context of model misspecification, the lower bound of the error variance should remain unchanged. This is because the signal models become matched —– only the emitter position at which the KL divergence between the true and presumed models is minimized shifts. This intuition is confirmed through MCRB calculations for model mismatch in first- and second-order pupil phase terms of the form, $e^{i2\pi\left[c_{1x}f_x+c_{1y}f_y+c_2\left(f_x^2+f_y^2\right)\right]}$.

In SPLM, the pseudo-true parameter vector is shifted relative to the ground truth as $\tilde{\boldsymbol{\theta}}_0 = \boldsymbol{\theta}_0 + \begin{bmatrix} c_{1x} & c_{1y} & -2fc_2 \end{bmatrix}$, yielding identical Poisson rates in the true and presumed models under the Fresnel approximation. This shift, while introducing bias, does not violate the model-based unbiasedness definition. Consequently, the generalized FIMs reduces to the classical FIM, making the MCRB coincide with the CRLB,

$$\begin{aligned} \mathrm{MCRB}(\tilde{\boldsymbol{\theta}}_0) &= \left[\sum_k \frac{\mathcal{N}_m}{\overline{I}_{\boldsymbol{\theta}}(t_k,\mathbf{0})}\nabla_{\boldsymbol{\theta}}\overline{I}_{\boldsymbol{\theta}}(t_k,\mathbf{0})\nabla_{\boldsymbol{\theta}}^T\overline{I}_{\boldsymbol{\theta}}(t_k,\mathbf{0})\Big|_{\boldsymbol{\theta}=\tilde{\boldsymbol{\theta}}_0}\right]^{-1} \\ &= \left[\sum_k \frac{\mathcal{N}_m}{\overline{I}_{\boldsymbol{\theta}}(t_k,\boldsymbol{c}_0)}\nabla_{\boldsymbol{\theta}}\overline{I}_{\boldsymbol{\theta}}(t_m,\boldsymbol{c}_0)\nabla_{\boldsymbol{\theta}}^T\overline{I}_{\boldsymbol{\theta}}(t_k,\boldsymbol{c}_0)\Big|_{\boldsymbol{\theta}=\boldsymbol{\theta}_0}\right]^{-1} = \mathrm{CRLB}(\boldsymbol{\theta}_0). \end{aligned} \tag{3.26}$$

The equivalence in (3.26) stems from the unchanged signal models, $\overline{I}_{\boldsymbol{\theta}}(t_k,\boldsymbol{c}_0)|_{\boldsymbol{\theta}=\boldsymbol{\theta}_0} = \overline{I}_{\boldsymbol{\theta}}(t_k,\mathbf{0})|_{\boldsymbol{\theta}=\tilde{\boldsymbol{\theta}}_0}$ for all k. Thus, the Fisher score is preserved and the error covariance lower bound remains unaffected under model-based unbiasedness. However, the MSELB increases due to the induced estimation bias,

$$\mathrm{MSELB} = \mathrm{CRLB}(\boldsymbol{\theta}_0) + \begin{bmatrix} c_{1x} & c_{1y} & -2fc_2 \end{bmatrix}^T \begin{bmatrix} c_{1x} & c_{1y} & -2fc_2 \end{bmatrix}, \tag{3.27}$$

as demonstrated in Fig. 3.2 (panel a) via the root mean square error lower bounds (RMSELB) with defocus aberration power mismatch.

Relative to the ideal CRLB, degradation in localization precision depends not only on the method's sensitivity to the emitter position, e.g., how defocus broadens the effective PSF and reduces spatial sensitivity, but also on the estimation bias. In SPLM, which maintains a nearly

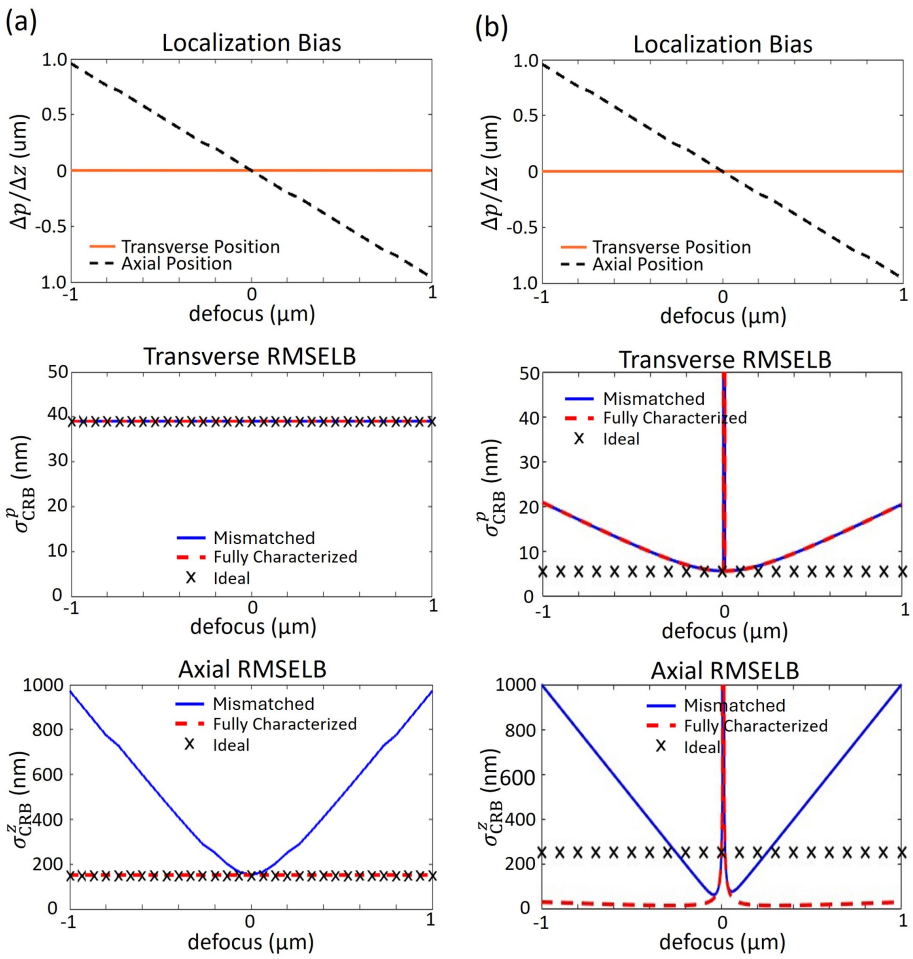

Figure 3.2: Systematic localization bias and RMSELB degradation in SPLM (a) and SMLM (b) with model mismatch in defocus aberration power. Lower bound for localization RMSE or precision in the ideal scenario is also plotted to highlight the expected performance change in localization.

uniform localization precision across a large FOV [14], the degradation is primarily driven by the introduced bias alone.

A parallel analysis applies to SMLM. Under identical experimental conditions, the KL divergence is minimized at the same biased parameter $\tilde{\boldsymbol{\theta}}_0$, yielding MCRB equal to CRLB under the fully characterized model. Their expressions mirror (3.26), with the normalized PSF replacing the illumination pattern and summation over the detector pixels instead of the time intervals. Since $\overline{\mathrm{PSF}}_{\boldsymbol{\theta}}(p_k, \boldsymbol{c}_0)|_{\boldsymbol{\theta}=\boldsymbol{\theta}_0} = \overline{\mathrm{PSF}}_{\boldsymbol{\theta}}(p_k, \mathbf{0})|_{\boldsymbol{\theta}=\tilde{\boldsymbol{\theta}}_0}$ for all pixels, the (misspecified) FIM remains unchanged when evaluated at the (pseudo-)true parameters. Nonetheless, the MSELB increases, analogously to (3.27), due to bias. Compared to the baseline, defocus broadens the transverse PSF width and

enhances axial sensitivity, resulting in reduced transverse precision but improved axial precision when the model captures the defocus correctly. This leads to a non-monotonic MCRB trend: the expected precision improves at first when bias is negligible, but degrades once the bias dominates.

In both SPLM and SMLM, tilt/defocus mismatch primarily introduces estimation bias, increasing the MSELB. There is no change between the MCRB and the CRLB in the fully characterized case because the difference between the true and presumed probability distributions vanishes with an appropriate shift in the emitter location.

3.4.2 Astigmatism

Astigmatism typically arises from asymmetries in the shape or curvature of the optical components, such as lenses or mirrors, leading to different focal planes and resulting in image blur and distortion. It can be modeled as either oblique astigmatism, $e^{i2\pi c_2^{xy}\kappa_x\kappa_y}$, or vertical astigmatism, $e^{i2\pi(c_2^x\kappa_x^2+c_2^y\kappa_y)}$, where $c_2^x \neq c_2^y$.

Oblique astigmatism contributes no aberration phase to SPLM when assuming that diffracted planewaves forming the structured illumination remain on-axis. As a result, no localization bias or change in precision is introduced. In contrast, SMLM lacks a closed-form expression for the KL divergence minimizer under oblique astigatism, necessitating numerical evaluation of the MCRB. This increases computational burden and, more importantly, implies that if the statistical gap between the true and presumed models cannot be closed by introducing a bias, the lower bound of error covariance inevitably deteriorates.

The same numerical approach is required for vertical astigmatism in both SPLM and SMLM, as no analytic expression exists for the pseudo-true parameter. For demonstration purpose, Fig. 3.3 shows the MCRB under mismatch along x-axis, i.e. $c_0^{2y} = 0$.

For both methods, estimation bias induced by vertical astigmatism manifests primarily in the axial position, driving the observed RMSELB change along that axis. While no bias is introduced for the estimation of emitter's transverse coordinates, the MCRB increases in SPLM due to the residual model mismatch at the pseudo-true location. In contrast, SMLM achieves a closer statisti-

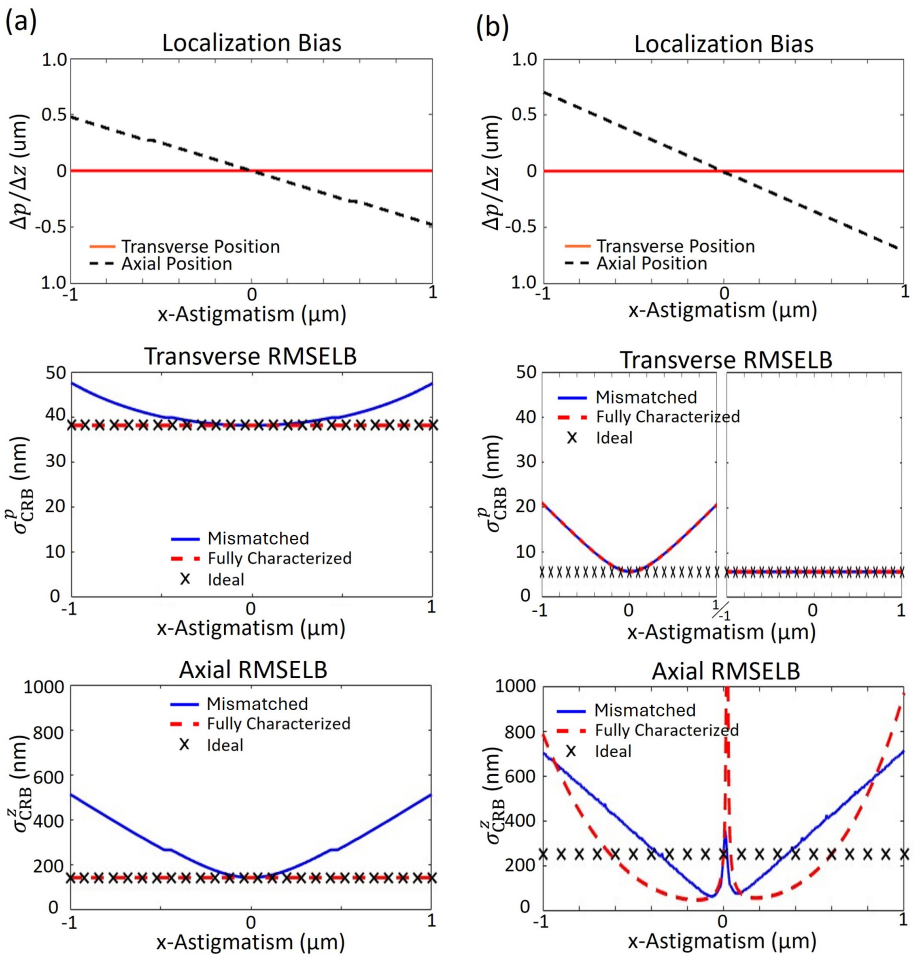

Figure 3.3: Systematic localization bias and RMSELB degradation in SPLM (a) and SMLM (b) with model mismatch in vertical astigmatism aberration power along x-axis. Lower bound for localization RMSE or precision in the ideal scenario is also plotted to highlight the expected performance change in localization.

cal match at the pseudo-true location, limiting MCRB degradation or even yielding improved axial precision under moderate mismatch. This effect is especially pronounced when the pseudo-true emitter position $\tilde{z}_0$ shifts significantly from the ground truth under large aberration power, due to the classical trade-off: moderate astigmatism initially improves axial localization precision by increasing sensitivity to depth-dependent PSF shape changes, reaching a minimum CRLB. Beyond a critical astigmatism power, however, further elongation of the PSF reduces its sharpness, leading to degraded axial precision.

Importantly, defocus-dependent ellipticity is used to infer emitter depth, forming the basis of astigmatism-based z-localization microscopy [31]. However, in the presence of misspecified astigmatism, the increased axial sensitivity also amplifies bias and increases MSELB in the axial direction.

In summary, aberrations influence localization performance through two distinct mechanisms. First, PSF broadening reduces the Fisher information along the affected axis, increasing the CRLB and degrading precision. Second, when the presumed model fails to capture aberrations present in the data, model mismatch introduces a statistical divergence between the true and presumed distributions. This can lead to systematic bias in localization and, in some cases, increased error variance. Together, these effects raise the overall MSELB relative to the ideal scenario —— even if the MCRB itself remains unchanged.

3.5 Conclusion

The MCRB provides a principled framework for analyzing localization precision under realistic experimental conditions, where model mismatch is inevitable. This work derives the MCRB for Poisson processes and demonstrates its use in SPLM and SMLM under mismatched aberration powers. We show that tilt and defocus introduce localization bias without degrading the lower bound on the error covariance, provided the signal models remain equivalent under a shift in the emitter position estimation. In contrast, mismatches in astigmatism and higher-order aberrations

may lead to both bias and increased error variance due to non-negligible statistical divergence between the presumed and true models.

By quantifying performance degradation from both bias and increased error covariance, the MCRB complements the classical CRLB and enables more robust precision analysis. This dual-framework approach offers practical guidance for optimizing PSFs and illumination strategies in advanced microscopy platforms, ultimately supporting the development of more accurate and resilient localization methods.

Chapter 4

SPLM Simulation and Location Estimation in Transverse Plane

4.1 Introduction

To identify an optimal localization strategy for SPLM with STM illumination, we conduct numerical simulations that mimic the system's data acquisition process. The simulated data applied with practical estimation algorithms may confirm the achievability of the CRLB under ideal conditions and assess the effect of experimental imperfections on localization precision.

In our simulation, we model an SPLM system in which an SLM projects a sequence of STM illumination patterns across the sample plane, synchronized with a pulsed laser source. Upon excitation at each pulse, each emitter may emit a photon with probability proportional to the illumination intensity and the fluorescent quantum yield. The emitted photons are collected in the pupil plane by a Single-Photon Avalanche Diode (SPAD) array, with detection efficiency governed by the condenser lens NA and the quantum efficiency of the detector. The strategy to detect in the pupil plane is to disassociate the emitted photon locations at where they are detected from the emitter locations so that each SPAD pixel has an equal probability to detect each emitted photon.

A first-order signal associated with a particular illumination pattern is computed by aggregating the photon counts across the SPAD array and averaging over multiple pulses. This process yields a compact temporal signal that encodes spatial information through the structured illumination and the spatially varying emitter distribution.

To infer emitter positions from the simulated measured signal, we formulate an inverse problem based on a statistical forward model of the imaging process. Estimation is performed using optimization frameworks that include a ℓ_1-norm penalty to induce sparsity in the estimated solution, reflecting the assumption that only a small number of emitters are present in the field of view

(FOV). In particular, we explore solvers based on proximal gradient methods, such as the Fast Iterative Shrinkage-Thresholding Algorithm (FISTA) followed with a line search method, more specifically, BFGS-based, to improve the precision of estimates. No additional prior information about emitter locations or brightnesses is assumed.

This chapter provides an overview of the simulation and estimation framework. We begin by describing the statistical model governing the data acquisition process. We then present the inverse problem formulation and discuss the numerical optimization method used to solve it. Finally, we evaluate the empirical localization performance of the estimation algorithm and compare it with theoretical bounds such as the CRLB, highlighting the effectiveness of the estimation algorithm and the effects of model mismatch on estimator precision.

4.2 Background

In this section, we formulate the forward model that governs the photon detection process under structured excitation. This model describes how illumination patterns, fluorophore distributions, and system optics collectively determine the detected photon counts at a single-pixel or pupil-plane detector.

Following the forward model, we formalize the inverse problem of estimating the spatial distribution of fluorescent emitters from the recorded signals along with their brightness. This reconstruction task is posed as an optimization problem over a high-dimensional parameter space, where sparsity is a key structural property of the solution. The estimation challenge is compounded by measurement noise, discretization errors, and potential mismatch between the physical system and the assumed model.

To solve the inverse problem efficiently, we empoly optimization techniques for solving ℓ_1-regularized inverse problems to promote solution sparsity. A widely used approach is FISTA due to its computational efficiency, simplicity of implementation, and ability to handle large-scale problems [59, 60]. We reivew the FISTA algorithm in the context of localization, with emphasis on its convergence behavior, sparsity-promoting properties, and adpatiation to Poisson noise model.

4.2.1 Measurement Model

We model the formation of the measured SPLM signal as a stochastic process slightly different than that described in CRLB chapter in preparation for calculation of higher-order signals. At each illumination pulse, each emitter behaves as a probabilistic source of a single photon, and the detection of emitted photons is governed by a uniform Poisson-binomial point process. That is, at each SPAD pixel, the number of detected photons is a Poisson0binomial random vector.

For simplicity, let there be J fluorescent emitters in the transverse plane, sparsely located at $\{(x_j, y_j)\}_{j=1}^{J}$. To account for the orientation-dependent excitation and emission efficiencies of the emitters, we introduce a scaling parameter c_j, for emitter brightness and assume it range from 0 to 1. At each pulse indexed by q, the emitters are excited by the illumination pattern at time $t_q = q/\nu_r$, where ν_r is the pulse train repetition rate. The duration of the pulse is assumed to be sufficiently short as compared to the emitter excited state lifetime, i.e., $\tau_p \ll \tau_e$. The rate of stimulated absorption, which is the probability per unit time that an atom or molecule in a lower energy state will absorb a photon and transition to a higher energy state, for each emitter is given by

$$k_{\mathrm{st}}^{(j,q)} = \frac{c_j \, I_{\mathrm{ill}}\left(\boldsymbol{r}_j, t_q\right)}{\tau_e \, I_{\mathrm{sat}}} = \alpha_{\mathrm{sat}} \, c_j \, \overline{I}_{\mathrm{ill}}\left(\boldsymbol{r}_j, t_q\right) \frac{I_{\mathrm{pu}}(t)}{\tau_e}. \tag{4.1}$$

Here I_{sat} is the saturation intensity, $\alpha_{\mathrm{sat}} = I_{\max}/I_{\mathrm{sat}}$ is the saturation parameter defined as the ratio between the maximum illumination intensity and the saturation intensity, $\overline{I}$ denotes the illumination intensity normalized throughout space and time so that its peak is unity, and $I_{\mathrm{pu}}(t)$ is the pulse temporal envelope normalized to peak value of unity.

Under the assumption of weak excitation, the probability of the peak excited state population for each emitter j at pulse q is given by

$$e_m^{(j,q)} \approx \int k_{\mathrm{st}}(\boldsymbol{r}_j, q) \, dt = \alpha_{\mathrm{sat}} \, c_j \frac{T_{\mathrm{pu}}}{\tau_e} \overline{I}_{\mathrm{ill}}\left(\boldsymbol{r}_j, t_q\right) = \gamma_{\mathrm{pu}} \, c_j \, \overline{I}_{\mathrm{ill}}(\boldsymbol{r}_j, t_q), \tag{4.2}$$

where $T_{\mathrm{pu}} = \int I_{\mathrm{pu}}(t) \, dt$ is the pulse duration. Following excitation, the probability of the emission rate follows $k_r \, \exp\left(-t/\tau_e\right)$, where the exponential function accounts for the decay of the excited

state population. Since the excitation and emission are considered independent and therefore, the probability of photon emission from the j^{th} emitter under the excitation of q^{th} pulse is given by

$$p_e^{(j,q)} = \int_0^\infty k_r \, e_m^{(j,q)} \, \exp\left(-t/\tau_e\right) dt \approx k_r \, \tau_e \, e_m^{(j,q)} = \Phi \, e_m^{(j,q)} = \Phi \, \gamma_{\text{pu}} \, c_j \, \overline{I}_{\text{ill}}(\boldsymbol{r}_j, t_q), \tag{4.3}$$

where k_r denotes emitter radiative emission rate and $\Phi = k_r \, \tau_e$ is the fluorescent quantum yield.

Each emitted photon has a finite probability of being detected, determined by the optical collection geometry and the SPAD detector efficiency. Let each SPAD pixel subtend a solid angle $\Omega_c^{(1)}$ defined as a fraction of the collection cone imposed by the system's numerical aperture, $\Omega_c^{(1)} = 2\,\pi\left(1 - \cos\left[\arcsin(\text{NA}/\text{n})\right]\right)/D$, where D is the total number of detectors. The detection probability given that an electron is excited and a photon is emitted shall be $\eta_c^{(1)} \, \eta_d$, where $\eta_c^{(1)} = \Omega_c^{(1)}/4\,\pi$ is the collection efficiency and η_d is the detector quantum efficiency. The probability that a photon is detected by a SPAD given emission from emitter j and excited by pulse q is then

$$p_d^{(j,q)} = \eta_c^{(1)} \, \eta_d \, p_e^{(j,d)} = \gamma^{(1)} \, c_j \, \overline{I}_{\text{ill}}(\boldsymbol{r}_j, t_q), \tag{4.4}$$

where we define a global scaling constant $\gamma^{(1)} = \eta_c^{(1)} \, \eta_d \, \Phi \, \gamma_{pu}$ and across all pixels, $\gamma = D \, \gamma^{(1)}$.

This framework naturally leads to a binomial point process interpretation: over a single pulse, each of the emitted photons from emitter j falling on a SPAD pixel represents a Bernoulli trial, with the detection event being a success with probability $p_d^{(j,q)}$. With Q pulses, there are n Bernoulli trials with the same success probability, which bring us to the binomial distribution. Furthermore, with J emitters, there are J binomial trials with different success probabilities. Thus, for each pulse q, the total SPLM signal as the sum of all detected photons from all emitters, assuming no background, is given by $y_q \sim \text{Poisson} - \text{Binomial}\left(\left\{\gamma \sum_{j=1}^{J} c_j \, \overline{I}_{\text{ill}}(\boldsymbol{r}_j, t_q)\right\}_{j=1}^{J}\right)$.

The simulated measured SPLM signal is then computed at each pulse q via the following steps:

— Calculate the success probability of detecting a photon from each emitter across all SPAD pixels, $\left\{\gamma \, c_j \, \overline{I}_{\text{ill}}(\boldsymbol{r}_j, t_q)\right\}_{j=1}^{J}$.

— Run a Bernoulli trial using each success probability, yielding y_q successful trials for y_q photons detected

— Uniformly distribution each of the y_q photons across D SPAD pixels

For now, we assume the SPAD array behaves more like a photomultiplier tutbe (PMT), meaning that the number of photons falling on each pixel is precisely captured rather than capping at one photon per detection period. For each illumination pattern m, we assume Q pulse excitation cycles and a first-order signal, proportional to the sum of the illumination pattern at emitter locations, can be calculated by taking the sample mean of Q realizations,

$$y_m = \frac{1}{Q} \sum_{i=0}^{Q-1} y_{mq+i}. \tag{4.5}$$

Due to the different success probabilities, y_m does not follow any distribution with a closed-form expression. Instead, we know its mean as $\gamma \sum_{j=1}^{J} c_j \, \overline{I}_{\text{ill}}(\boldsymbol{r}_j, t_q)$ and variance as $\sum_{j=1}^{J}(1 - \gamma \, c_j \, \overline{I}_{\text{ill}}(\boldsymbol{r}_j, t_q))\gamma \, c_j \, \overline{I}_{\text{ill}}(\boldsymbol{r}_j, t_q)$. Since the success probability of each photon detected is small, $\gamma \, c_j \, \overline{I}_{\text{ill}}(\boldsymbol{r}_j, t_q) \ll 1$, the distribution of the sample mean can be further approximated by a Poisson distribution via Le Cam's theorem [61, 62], i.e. $y_m \sim \text{Poisson}\left(\gamma \sum_{j=1}^{J} c_j \, \overline{I}_{\text{ill}}(\boldsymbol{r}_j, t_q)\right)$.

4.2.2 Formulation of Inverse Problem

When discretizing the image domain into N candidate grid points for matrix operation, we assign the scaled STM illumination pattern with a matrix $\boldsymbol{A} \in \mathbb{R}^{M \times N}$, where M is the number of illumination samples. Each row $\boldsymbol{A}_m \in \mathbb{R}^N$ contains the scaled illumination pattern for the m^{th} sample mean. Specifically, the matrix entry for the j^{th} grid point under the m^{th} illumination is given by $\boldsymbol{A}_{m,j} = \gamma \, c_j \, \overline{I}_{ill}(\boldsymbol{r}_j, t_{mq})$.

Let $\boldsymbol{x} \in \boldsymbol{R}_+^N$ represent the unknown brightness vector, where $\boldsymbol{x}_j$ is nonzero only at or near true emitter locations. The first-order photon counts $\boldsymbol{y} \in \mathbb{N}^M$ are modeled as

$$\boldsymbol{y} \sim \text{Poisson}\left(\boldsymbol{A}\,\boldsymbol{x}\right) \tag{4.6}$$

via distribution approximation.

The first objective is to recover a sparse estimate $\hat{\boldsymbol{x}}$ of the emitter brightness vector over the grid. Due to the inherent sparsity of active emitters in the sample, regularized optimization technique, such as ℓ_1-penalized reconstruction, is employed to promote sparse solutions. The mathematical formulation of the inverse problem is, thus, given by

$$\hat{\boldsymbol{x}} = \underset{\boldsymbol{x}}{\operatorname{argmin}} \frac{1}{2} \|\boldsymbol{A}\,\boldsymbol{x} - \boldsymbol{y}\|_2^2 + \varepsilon_0 \,\|\boldsymbol{x}\|_1. \tag{4.7}$$

Since the derivative of the ℓ_1-norm vanishes at 0, standard gradient-based methods are not directly applicable. Instead, proximal gradient methods are typically used to solve this class of composite optimization problems [59]. One such efficient method is FISTA, where the estimate is updated as follows,

1. Initialize $\boldsymbol{x}^{(0)} = \boldsymbol{z}^{(0)}$ =random matrix and set $t^{(0)} = 1$,

2. For each iteration $k = 1, 2, \cdots$ when extended with additional regularization such as non-negativity constraints,

$$\begin{aligned}
\boldsymbol{x}^{(k)} &= \operatorname{prox}^{+}_{\varepsilon_0 \eta}\left(\boldsymbol{z}^{(k-1)} - \eta \nabla f(\boldsymbol{z}^{(k-1)})\right), \\
t^{(k)} &= \frac{1 + \sqrt{1 + 4(t^{(k-1)})^2}}{2}, \\
\boldsymbol{z}^{(k)} &= \boldsymbol{x}^{(k)} + \left(\frac{t^{(k-1)} - 1}{t^{(k)}}\right)(\boldsymbol{x}^{(k)} - \boldsymbol{x}^{(k-1)}),
\end{aligned}$$

   where η is the step size, and $\operatorname{prox}^{+}_{\varepsilon_0\,\eta}(\cdot)$ denotes the proximal operator for the ℓ_1-norm, defined elementwise as soft-thresholding, $\operatorname{prox}^{+}_{\varepsilon_0\,\eta}(z_j) = \max\left(|z_j| - \varepsilon_0\,\eta, 0\right)$.

In this context, FISTA is capable of recovering sparse emitter locations with high fidelity under experimentally realistic signal-to-noise ratios (SNR). Its accerlated convergence rate of $\mathcal{O}(1/k^2)$, where k is the iteration index, ensures computational efficiency.

The second objective is to refine the estimates obtained from the initial sparse reconstruction. While the FISTA-based solution provides a coarse, grid-based approximation of emitter locations,

it is fundamentally limited by the discretization of the image domain. To overcome this limitation and achieve sub-pixel localization precision, a grid-free continuous-domain refinement is performed.

Specifically, the non-zero components in the FISTA estimate $\hat{\boldsymbol{x}}$ are treated as initial seeds for the emitter locations and brightness. These candidate positions and brightness are then refined by solving a continuous optimization problem using a line-search-based method, considering that the loss function in the local neighborhoods of the inital estimates becomes relatively convex. We adopt the BFGS method to optimize the ℓ_2-norm associated with the forward model,

$$\{\hat{c}_j, \hat{\boldsymbol{r}}_j\}_{j=1}^{J} = \underset{\boldsymbol{c},\boldsymbol{r}}{\operatorname{argmin}} \frac{1}{2} \| \sum_{j=1} J\gamma \, c_j \, \overline{I}_{ill}(\boldsymbol{r}_j, t_{mq}) - y_m \|_2^2, \tag{4.8}$$

given that the error in the spatial frequencies projected between the model and data is relatively small or negligible. The BFGS method balances curvature information and efficient step directions, offering superlinear convergence in practice, as follows:

1. Set initial estimates of emitter locations and brightness from the FISTA result, $\boldsymbol{\theta}^{(0)} = \{x_j^{(0)}, y_j^{(0)}, c_j^0\}_{j=1}^{J}$. Initialize the inverse Hessian approximation $\boldsymbol{H}^{(0)}$ as identity,

2. Compute the gradient of the loss function $\mathcal{L}$ with closed-form expressions, $\nabla_{\boldsymbol{\theta}} \mathcal{L}$,

3. Use the inverse Hessian approximation to compute the descent direction given by $\boldsymbol{p}^{(k)} = -\boldsymbol{H}^{(k)} \nabla \mathcal{L}(\boldsymbol{\theta}^{(k)})$, and perform a line search to find a step size $\alpha^{(k)}$ satisfying Wolfe conditions,

4. Update parameters, $\boldsymbol{\theta}^{(k+1)} = \boldsymbol{\theta}^{(\boldsymbol{k})} + \alpha^{(k)} \, \boldsymbol{p}^{(k)}$

5. Update the inverse Hessian, $\boldsymbol{H}^{(k+1)} = \left(\boldsymbol{I} - \dfrac{\boldsymbol{s}^{(k)} \, \boldsymbol{y}^{(k)^T}}{\boldsymbol{y}^{(k)^T} \, \boldsymbol{s}^{(k)}} \right) \boldsymbol{H}^{(k)} \left(\boldsymbol{I} - \dfrac{\boldsymbol{y}^k \, \boldsymbol{s}^{(k)^{(T)}}}{\boldsymbol{y}^{(k)^T} \, \boldsymbol{s}^{(k)}} \right) + \dfrac{\boldsymbol{s}^{(k)} \, \boldsymbol{s}^{(k)^T}}{\boldsymbol{y}^{(k)^T} \, \boldsymbol{s}^{(k)}}$, where $\boldsymbol{s}^{(k)} = \boldsymbol{\theta}^{(k+1)} - \boldsymbol{\theta}$ and $\boldsymbol{y}^{(k)} = \nabla \mathcal{L}(\boldsymbol{\theta}^{(k+1)}) - \nabla \mathcal{L}(\boldsymbol{\theta}^{(k)})$.

The optimization proceeds until convergence criteria are met, such as the norm of the gradient falling below a small threshold or relative change in objective being sufficiently small.

This two-stage approach —– first using FISTA for robust, sparse grid-based localization, followed by BFGS-based gradient descent for precise, grid-free refinement —– enables emitter recovery with better precision.

4.2.3 Aberration Correction

We assume the aberrations can be captured via a nonlinear frequency sweep. For each of the transverse axis, the total phase with the correction polynoimal is given by, when using CHIRPT-inspired masks,

$$\Delta\Phi_p(t) = 2\,\pi \left(\nu_{c,p} t + \frac{\mathrm{NA}}{\lambda_{\mathrm{ex}}\, t_c} t\, p + \frac{\mathrm{NA}}{\lambda_{\mathrm{ex}}\, t_c} \sum_i \beta_i\, t^i \right) \circledast \mathrm{III}\left(\frac{t}{T_p} \right), \tag{4.9}$$

where $\{\beta_i\}_i$ is a small set of coefficients. To generate realistic aberrations in simulation, we use a small number of Zernike polynomial terms to represent common optical aberrations such as defocus, astigmatism, and coma. Random coefficients with small magnitudes are assigned to each Zernike mode to ensure the aberrations remain within the weak regime, where the reconstructed image under ideal (aberration-free) conditions still closely resembles the ground truth object. The resulting aberrated pupil phase is shown in Fig. 4.1(a). Since the CHIRPT-like illumination scheme involves scanning a first-order diffracted beam across the pupil plane for each transverse axis, the additional phase introduced to the signal is not the entire 2D aberrated pupil, but rather a 1D trace across it over time. Specifically, the beam samples a path through the pupil that evolves along the scanning axis (e.g., the x-axis), effectively modulating the illumination with a time-dependent phase distortion. This temporal phase sweep — overlaid with the designed frequency chirp and carrier frequency —– defines the total phase term in Eq. 4.9. The corresponding aberrated phase trajectory sampled during the scan is illustrated in Fig. 4.1(b).

To evaluate the performance of the aberration correction algorithm, we first simulate a 1D calibration experiment using a known bright test object so that the SNR is relatively high. Specifically, we assume perfect knowledge of the object, a Ronchi-ruling-like object with ideal binary contrast, known spatial frequency, and controlled duty cycle. This serves as a controlled baseline scenario,

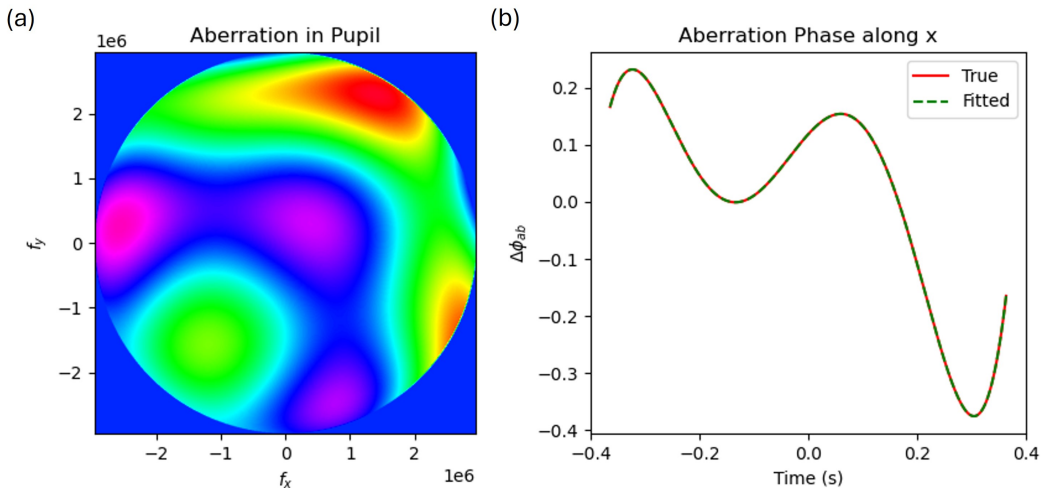

Figure 4.1: Simulation of optical aberrations in structured illumination. (a) 2D aberrated pupil phase map generated using 20 orders of Zernike polynomials. (b) Corresponding 1D slice of the pupil phase along the x-axis, representing the effective additional phase modulation in the time trace during the CHIRPT-like scan.

where the only source of measurement discrepancy arises from the distortion in the projected structured illumination. The choice of a Ronchi ruling is intentional: such an object acts as a diagnostic tool to directly sample the temporal frequency modulation at resonance spatial frequencies projected. Any curvature or deviation in the modulation, induced by aberrations, leads to predictable distortions in the measured image. By analyzing how the known

The ideal Ronchi pattern for this purpose contains moderate spatial frequency content (e.g., 100–200 line pairs per millimeter in the object region) and a very low duty cycle (1–10%). Sparse, narrow bars in such a pattern enhance the decomposition of the object into a broad spectrum of spatial frequencies, including higher-frequency components that are more sensitive to subtle phase distortions. This makes the Ronchi ruling especially well suited for probing the fidelity of spatial frequency modulation and mapping the effective curvature that must be compensated to restore accurate illumination modulation.

Moreover, slightly restricting the analysis to a reduced FOV significantly improves the convergence behavior of the aberration coefficient estimation. A smaller FOV reduces spatial averaging over aberrated regions, allowing optimization to more tightly fit the local distortion. This improves

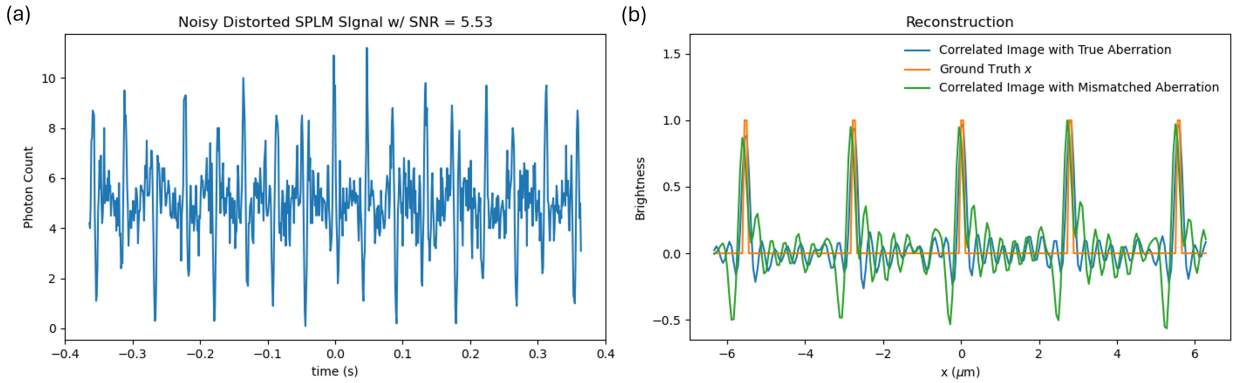

Figure 4.2: (a) First-order aberrated SPLM signal with SNR ≈ 5. (b) Comparison among the correlated image from signal model with true aberration phase (blue), the ground truth Ronchi ruling (orange), and the correlated image from aberration-free signal model (green).

both the stability and accuracy of the estimated correction terms and enables reliable compensation of aberrations using a compact polynomial basis.

In the forward model, we generate a first-order signal resulting from the modulation of the Ronchi ruling by aberrated spatio-temporal illumination patterns. A fluctuating signal is calculated by subtracting the empirical mean so that an image may be reconstructed via correlation,

$$\hat{\boldsymbol{x}}_{\text{corr}} = \frac{\boldsymbol{A}(\hat{\boldsymbol{\beta}})^{\dagger}\left(\boldsymbol{y} - \|\boldsymbol{y}\|_1\right)}{\max\left(\boldsymbol{A}(\hat{\boldsymbol{\beta}})^{\dagger}\left(\boldsymbol{y} - \|\boldsymbol{y}\|_1\right)\right)}. \tag{4.10}$$

A comparison among the ground truth and the correlated images using true and uncorrected signal models is plotted in Fig. 4.2, along with an example of the distorted SPLM signal. Deviations in peak locations and widths illustrate the effect of aberrations on reconstruction fidelity and motivate the need for calibration.

We define a loss function based on the discrepancy between the reconstructed image and a ground-truth reference. The reference is generated by convolving the known Ronchi ruling with the system's effective PSF, $\boldsymbol{x}_{\text{ref}} = \boldsymbol{H}\,\boldsymbol{x}$, where $\boldsymbol{H}$ is a Toeplitz matrix where each row contains a shifted version of the PSF kernel, $h_i = \text{PSF}(x - x_i) = \dfrac{\sin\left(2\,\pi\,\text{NA}\,(x - x_i)/\lambda\right)}{\pi\,\text{NA}\,(x - x_i)/\lambda}$. The loss function is defined as the ℓ_2-norm of the difference between the reconstructed image and this ideal

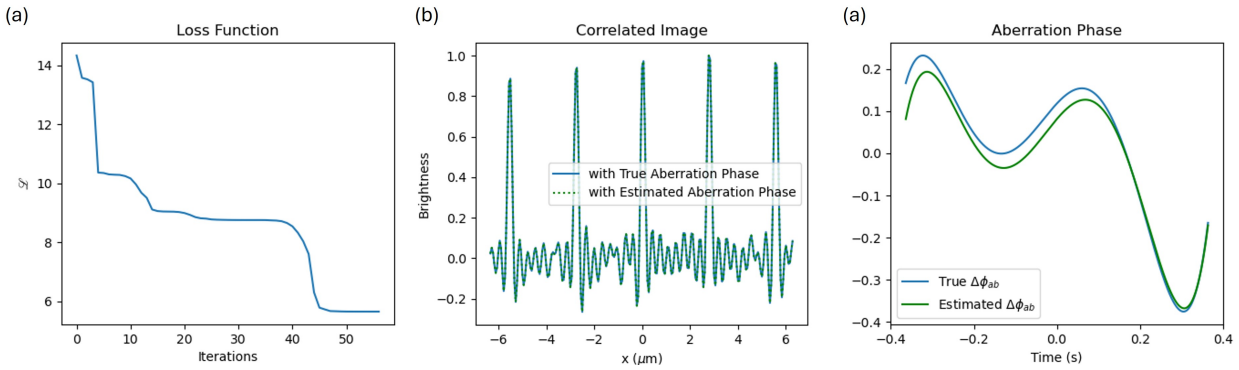

Figure 4.3: (a) Decrease of the loss function with respect to iterations during the optimization. (b) Reconstructed image from correlation using estimated distortion parameters (orange dotted) overlaid with that using true distortion (blue solid). (c) Comparison of initial distortion (blue) and residual distortion after correction (orange).

reference,

$$\mathcal{L}(\boldsymbol{\beta}) = \frac{1}{2}\|\hat{\boldsymbol{x}}_{\text{corr}} - \boldsymbol{x}_{\text{ref}}\|_2^2 + \alpha\|\boldsymbol{\beta}\|_2^2. \tag{4.11}$$

While any displacement or frequency mismatch in the Ronchi ruling degrades the accuracy of distortion recovery, this idealized simulation provides a clean testbed to effectiveness of the calibration algorithm. We solve this nonlinear optimization using the L-BFGS-B algorithm with approximated inverse Hessian. This approach enables rapid convergence and the computational speed can be improved by providing an analytical form of the gradient of the loss function with respect to the illumination distortion parameters.

As shown in Fig. 4.3, the loss function decreases with iterations, confirming the effective convergence. The comparison between the reconstructed image using the estimated aberration coefficients and that using the ground-truth shows close agreement. Finally, the residual distortion after correction demonstrates that most of the aberrations has been mitigated.

4.3 Simulation and Discussions

To evaluate the practical impact of spatial frequency distortion on emitter localization, we perform a set of simulations under controlled conditions. In our setup, we assume the distortion is introduced along a single spatial axis "seen" by the diagonally scanning beam in the pupil plane,

consistent with the unidirectional frequency shift addressed in the calibration procedure described earlier. This distortion is representative of optical aberrations or misalignment errors that perturb the effective spatial frequency content of the modulated illumination patterns. Such deviations can significantly impair the estimation precision, leading to localization artifacts such as missing emitters, spatial bias, or underestimated brightness. Our goal is to assess the degradation in performance due to uncorrected distortion and the degree of improvement achieved through calibration. By comparing the results across different conditions, including uncorrected and corrected distortion, as well as ideal (undistorted) scenarios. We demonstrate how spatial frequency fidelity directly influences localization precision. We further benchmark these results against the CRLB to understand how close practical estimation approaches the theoretical limit under each condition.

We begin by establishing a baseline for localization performance under ideal conditions — - specifically, in the absence of any aberrations. In this configuration, 20 fluorescent emitters are simulated with a mean photon count of approximately 5000 photons per emitter. The initial

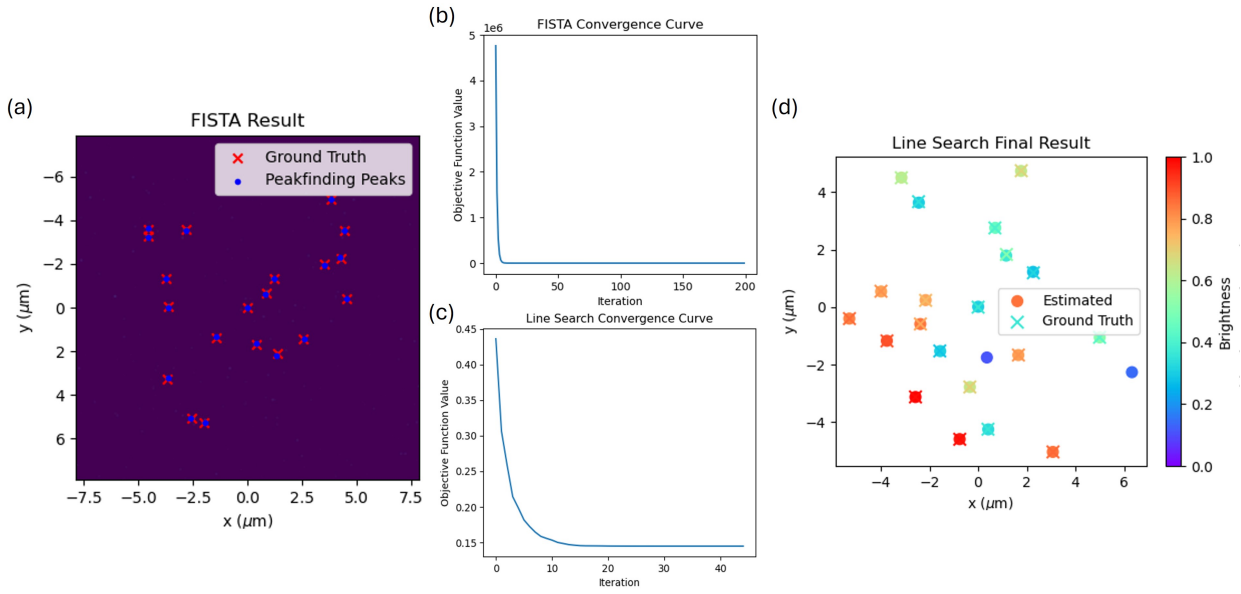

Figure 4.4: Localization results under distortion-free conditions. (a) Estimated emitter brightness and positions from FISTA, showing accurate recovery of all 20 emitters. (b) Convergence of the FISTA algorithm, demonstrating rapid decrease in objective function value. (c) Refined emitter estimates from subsequent grid-free BFGS-based line search, further reducing localization error. (d) Convergence curve of the line search method, showing fast convergence after FISTA initialization.

reconstruction using FISTA successfully identifies all 20 emitters with high fidelity, providing accurate seeds for subsequent grid-free refinement via line search, as shown in Fig. 4.4. The final estimates achieve a root mean squared error (RMSE) of 22.11 nm in position and 0.04 in brightness. The total processing time is 3.56 s, which is ideal for real-time imaging processes.

To highlight the impact of spatial frequency distortion, we then apply an uncorrected distortion along one spatial axis. In this case, FISTA is able to resolve 18 of the 20 emitters with 3 false detections, reflecting both degraded contrast and reduced spatial resolution. The subsequent line search refinement is hindered by the poor initialization, resulting in significantly worse performance: 206.40 nm RMSE in position and 0.14 in brightness for the matched emitters. However, when distortion is corrected, the quality of the initial estimate improves ——- FISTA recovers 20 emitters with 1 false detection, and the final localization precision is enhanced. The corrected results yield 44.11 nm RMSE in position and 0.06 in brightness for the matched emitters, which approaches the ideal performance and validates the efficacy of the calibration strategy. Fig. 4.5 illustrates this improvement through side-by-side comparison of the localization results under each scenario.

To further assess the estimation performance under various conditions, we benchmark the achieved localization precision against the CRLB, which sets a theoretical limit on the minimum

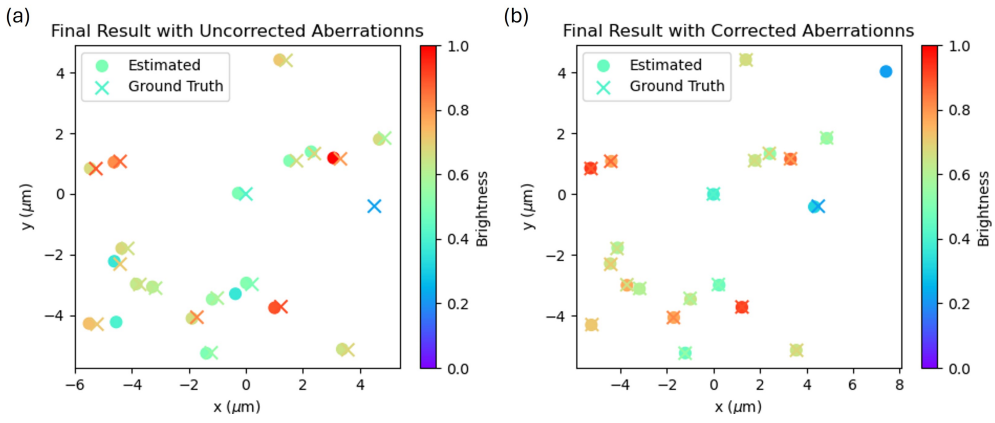

Figure 4.5: Impact of spatial frequency distortion and correction on emitter localization. (a) Localization results under distortion without correction. Only 15 emitters are localized. (b) Localization results under distortion with calibration correction applied. 17 emitters are localized.

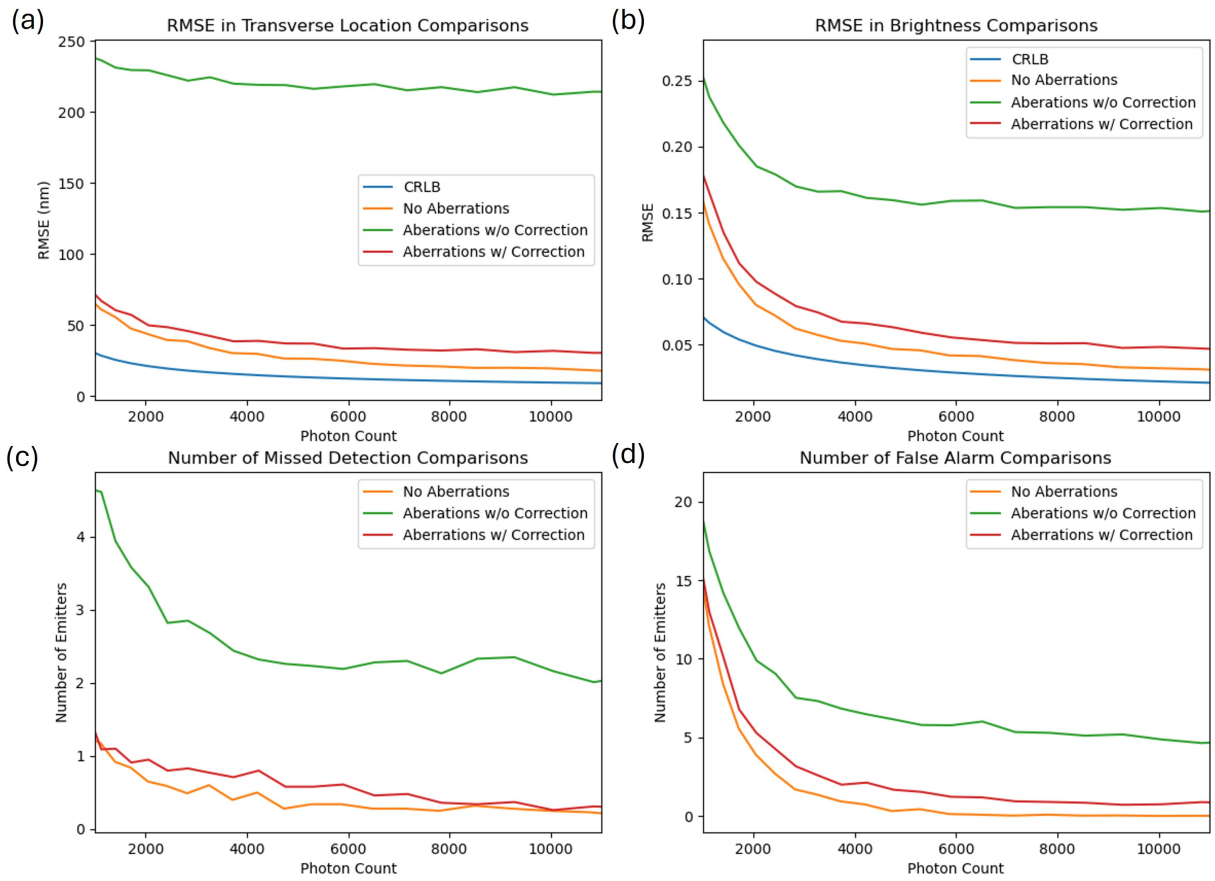

Figure 4.6: Comparisons of (a) RMSE in emitter transverse locations and (b) RMSE in emitter brightness plotted as functions of mean photon count detected under the scenarios with no aberration (orange), unaccounted aberrations (green), and corrected aberrations (red) to the squared root of the CRLB (blue). Also plotted are the (c) Number of missed detections, and (d) Number of false alarm.

achievable variance for unbiased estimators. Specifically, we evaluate the empirical RMSE in position and brightness from 100 trails of 20 emitters as a function of the total photon count per emitter. These results are compared to the square root of the approximated CRLB curve, the single emitter CRLB scaled by N, derived under the same imaging model assumptions.

As shown in Fig. 4.6, under ideal, aberration-free conditions, the RMSE approaches $\sqrt{\text{CRLB}}$ as the expected photon count per emitter increases, demonstrating improved estimator efficiency. However, a noticeable gap remains, likely due to practical limitations such as seeding accuracy and non-convex optimization effects. In the presence of uncorrected aberrations, the RMSE increases substantially, confirming the degraded sensitivity of localization precision to model mismatch.

Importantly, applying our aberration correction algorithm significantly mitigates this degradation, with RMSE values much closer to the ideal case. In addition to precision metrics, we assessed detection performance by measuring the number of missed detections and false alarms. The results indicate that when FISTA provides accurate initial seeds, both error types are minimized. This highlights the need to adapt peak detection thresholds based on signal-to-noise ratio (SNR). Nevertheless, at moderately high photon counts, the current approach consistently yields near-zero missed detections and false positives, confirming the robustness of the full estimation pipeline.

4.4 Future Research

Building on the proposed simulation and estimation framework, a natural next step is to evaluate the performance and limitations of the aberration correction algorithm under real experimental conditions. While the current study uses an arbitrary 1D Ronchi-ruling-like object to simulate calibration and correction performance, experimental validation is required to assess the robustness of the approach to real-world noise, fabrication imperfections, and system drift.

Initial efforts will involve applying the calibration and correction pipeline to imaging data acquired from a fabricated Ronchi-ruling-like object with well-defined spatial frequency and duty cycle. However, such test objects cannot be assumed to be perfectly known in practice. To address this limitation and to create a more flexible and biologically relevant calibration strategy, we propose transitioning to randomly spaced quantum dots as the calibration object. These emitters naturally encode a rich set of spatial frequency content due to their stochastic pairwise spacing. When structured illumination sweeps through known spatial frequencies, the resulting modulated signals can be used to infer local phase errors, effectively mapping out the aberration-induced distortions across frequency space.

As an initial step, we will assume known quantum dot locations and assess the ability of the correction algorithm to recover aberration coefficients from their modulated signals. This enables testing under more realistic spatial variability while maintaining control over ground truth. The longer-term objective is to develop a joint estimation algorithm that simultaneously solves for

the aberration parameters and the emitter positions. This requires extending the inverse problem formulation to jointly model spatial sparsity and temporal-frequency-domain phase errors, and implementing an alternating or gradient-based solver capable of converging.

A complementary direction is to optimize the design of STM illumination patterns based on object priors and information-theoretic metrics. Specifically, the FIM can be expressed in closed-form matrix operations under the shot-noise-limited detection model,

$$J_{\boldsymbol{A}}(\boldsymbol{x}) = \sum_{m} \frac{1}{\boldsymbol{A}_m \boldsymbol{x}} \cdot \boldsymbol{A}_m^T \boldsymbol{A}_m. \tag{4.12}$$

While its inverse, the CRLB, does not have a closed-form expression, if we define $\boldsymbol{D} = \mathrm{diag}(\boldsymbol{A}\boldsymbol{x})$, then the FIM can be written as $J_{\boldsymbol{A}}(\boldsymbol{x}) = \boldsymbol{A}^T \boldsymbol{D}^{-1} \boldsymbol{A}$ and the CRLB becomes $\mathrm{CRLB}_{\boldsymbol{A}}(\boldsymbol{x}) = \left(\boldsymbol{A}^T \boldsymbol{D}^{-1} \boldsymbol{A}\right)^{-1}$, where the trace defines the lower bound of error covariance for each parameter in $\boldsymbol{x}$.

Chapter 5

Quantitative Scattering Microscopy (QSCAT)

5.1 Introduction

Differential Phase Contrast (DPC) microscopy is an optical imaging technique that enables the quantitative reconstruction of phase information from transparent or weakly absorbing specimens. In electrochemical systems, this phase shift is directly related to the spatial distribution of optical susceptibility, which encodes key information about material composition, refractive index variations, and local concentration changes. For example, quantitative phase measurements can be used to identify different chemical species and even estimate the number of ions inserted into host materials during intercalation reactions, offering non-invasive insights into ion transport, electrochemical activity, and material response.

Traditional widefield microscopy, however, is inherently insensitive to phase because the phase fluctuations of the optical field occur on timescales much faster than the camera's exposure time. As a result, only intensity —– the squared magnitude of the optical field —– is recorded, discarding crucial information about the object's spatial phase profile.

To recover phase information, DPC introduces asymmetry in the illumination of the microscope's pupil. By selectively shifting the angular distribution of illumination light, phase gradients in the object plane are translated into measurable intensity differences in the image plane. This directional sensitivity to phase gradients forms the basis of DPC contrast.

In this chapter, we present QSCAT, a system that implements DPC microscopy using a digital light processing (DLP) projector to dynamically modulate the illumination at the pupil plane. This structured pupil illumination allows for programmable, high-speed switching between asymmetric patterns, enabling flexible and precise probing of spatial phase variations in electrochemical samples.

We describe the alignment and calibration procedure necessary to project pupil patterns more accurately onto the back focal plane of the objective lens. Preliminary results from a USAF resolution target demonstrate the system's capability to retrieve quantitative phase maps, which are validated by converting the measured phase gradients into absolute height profiles of chromium structures to be compared with the nominal height provided by the manufacturer.

The chapter begins by introducing the forward imaging model for DPC with structured pupil illumination and the algorithmic framework used to reconstruct phase. The results demonstrate QSCAT's potential for label-free, quantitative imaging of electrochemical systems at sub-wavelength sensitivity.

5.2 Background

To enable DPC, a clear understanding of both the optical configuration and the underlying image formation model is essential. This section provides the necessary experimental and theoretical background to support the implementation and analysis of the QSCAT system. We begin by detailing the optical setup, including the alignment and calibration of the DLP at the conjugate pupil plane, which is critical for an accurate mapping between the projected patterns and their intended pupil positions. The section then introduces the DPC imaging model, which relates the measured intensity images to phase gradients in the sample, and reviews the algorithmic steps required to reconstruct quantitative phase maps from multiple asymmetric illuminations. Together, these components form the foundation for robust phase retrieval in electrochemical imaging applications.

5.2.1 Experiment Alignment and Calibration

The experimental setup for QSCAT is designed to enable structured pupil illumination using a DLP. The illumination is provided by a green LED centered at 505 nm, which is relayed through two sequential 4f systems onto the object region. The DLP is placed one focal length away from the first lens, positioning it at a plane conjugate to the back pupil of the objective. The focal length of this lens is chosen so that the spatial coherence area at the DLP is smaller than the DLP pixel

size, minimizing the possibility of speckle noise due to interference. The coherence area A_c is estimated from the van Cittert–Zernike theorem as,

$$A_c \approx \left(\frac{\lambda f_1}{D}\right)^2, \tag{5.1}$$

where f_1 is the focal length and D is the diameter of LED source. With $1mm$ LED source size, the focal length must not exceed 25.8 mm. Due to the physical constraints in the system, however, the shortest focal length can be implemented is 30 mm. Ideally, the coherence area can be further modified by a magnifying 4f system. Since the illumination from the first lens is already collimated to the size of the 1-in optics, to reduce the spatial coherence, 2-in optics would be required. However, since the spatial coherence is already approximately the size of individual pixels on the the DLP, we inserted a glass diffuser a small distance away from the LED to help reduce the spatial coherence.

Zeiss 40× 0.65 NA A-plan objective is used for imaging. The tube lens (100 mm) on the illumination side is a bit smaller than the nominal Zeiss tube lens to maintain optical compatibility and proper magnification as well as to reduce the energy apodization through propagation. The remaining relay optic (75 mm) is chosen so that the DLP, when fully turned on, projects an image that fills the back focal plane of the objective, allowing the maximal amount of light to enter the objective. A bandpass filter centered around 515 nm is placed in front of the DLP to minimize the angular dispersion of colors introduced by diffraction. The collection path is arranged in an epi-direction configuration, using a tube lens (150 mm) for image relay onto a Thorlabs' TSI CMOS camera. A schematic diagram and two implementations of the system layout are provided in Fig. 5.1

To align the optical system, a diode laser centered at 520 nm is mounted atop the objective and routed backward through the optical path. All components except for the first lens are mounted on Thorlabs' 30 mm capge system to ensure the optical axis is properly centered relative to all components. All lenses preceding the DLP are arranged in 4f relay pairs. Proper 4f spacing is

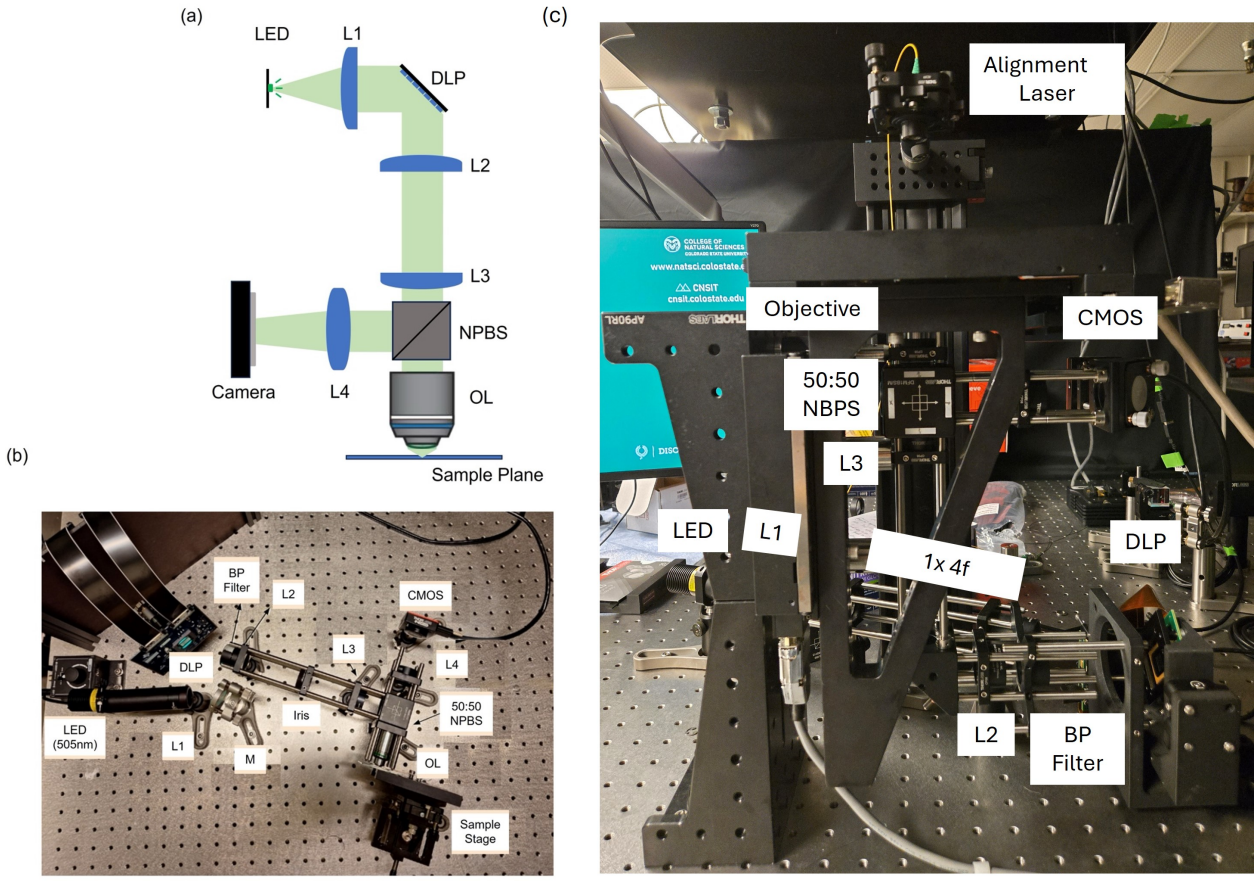

Figure 5.1: (a) Schematic diagram of the optical system used for quantitative phase microscopy, highlighting key components including LED source, relay lenses, DLP, objective, tube lens, and camera. (b) and (c) Two practical implementations of the system with component shorthand notations, demonstrating alternative layouts used during the alignment and data acquisition phases.

verified using a Thorlabs shearing interferometer to confirm beam collimation between conjugate planes.

A critical component requiring careful alignment is the DLP. Since no optics or mechanical holders can obstruct the micro-mirror area, it is mounted via a 60 mm cage system. A 30mm-to-60mm cage adapter plate is employed to align the DLP center with the central beam path. The device must be mounted at a $45\,\mathrm{deg}$ angle as each micro-mirror on the DLP tilts along a diagonal axis. This simplifies alignment and ensures efficient coupling into downstream optical elements since both the incoming beam and the brightest diffracted beam remain parallel to the optical table. The DLP is then positioned perpendicular to the incoming laser beam and we scan the incident

angle to minimize the power on diffracted beams [63]. To verify the perpendicularity, we examed the reflection of the alignment beam when the DLP is inactive (mirrors not tilted) and ensured it goes through the center of the cage system. Once verified, the DLP is activated to show a uniform pattern, and once the incident angle is set to where the main diffracted beam is maximized. We then set the first lens of the 4f system that relays the partially incoherent pupil illumination by ensuring the beam passes through the front center of the lens and the center of the cage system on which the lens is mounted. The rest of the lenses to follow are all set in 4f configuration along the cage system. And the LED is placed in front of the last lens with a glass diffuser.

To ensure a more accurate pupil plane modulation, we calibrate the DLP so that the projected half-pupil masks are correctly imaged onto the back focal plane of the objective lens. This step is critical to achieve reliable phase-gradient contrast. The calibration begins by placing a mirror in the object region and translating the sample stage axially to bring the illumination beam into focus onto the camera. For each principal axis of the DLP, row and column, we sweep the dividing line of a binary mask across from one edge to the other. At each dividing line position, we capture two images: one using the positive version of the mask and the other using its inverse (i.e., flipped bright and dark regions). The sum of intensities, normalized by the sum of intensity with the full pupil, is computed for each pair of images and plotted as functions of the dividing line position as shown in Fig. 5.2. The DLP is properly aligned when the intensities of the positive and negative images are relatively equal.

5.2.2 Imaging Model and Phase Reconstruction

The full model of the field arriving on the detector should consist of the reflected illumination, the forward-scattering field via the reflection illumination, and the back-scattered field via the illumination. However, because of the inherent nonlinearity of the rapidly oscillating back-scattering field even under the first Born approximation, the full model makes the phase recovery difficult [63]. To simplify the physical model, we consider only the forward-scattering field and with the assumption that the phase accumulated through the object is slow and can be linearized. There-

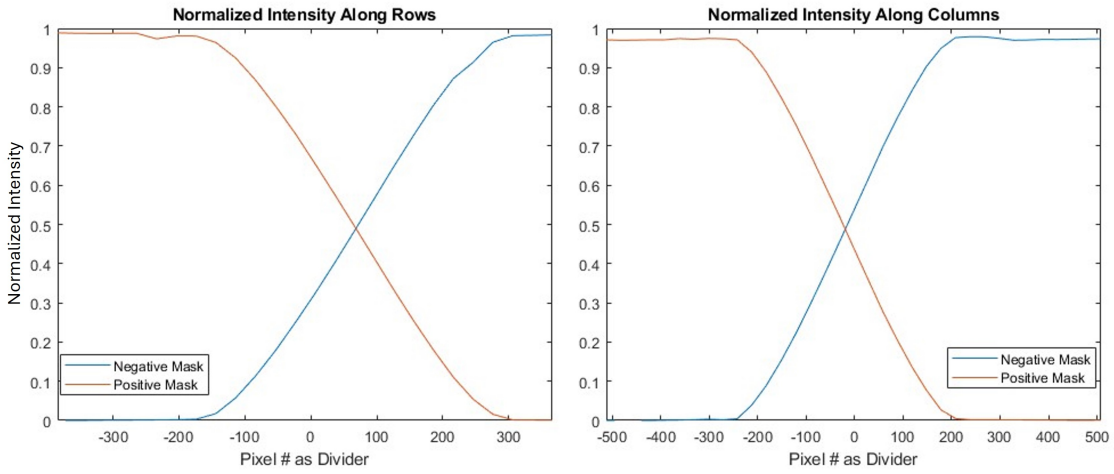

Figure 5.2: DLP calibration curves. For each axis, the dividing line of the half-pupil mask is swept across the DLP, and at each position, two complementary patterns are displayed. The normalized sum of the resulting image intensities produces a pair of sigmoidal-like curves that intersect near the true pupil center. The crossing point identifies the symmetric alignment of the mask relative to the objective pupil, enabling accurate spatial phase modulation.

fore, we model the absorption and scattering of an object as a complex transmission function, $o(\boldsymbol{r}) = \exp\left(-\mu(\boldsymbol{r}) + i\,\phi(\boldsymbol{r})\right)$. The intensity at the camera can be approximated by an incoherent sum [24, 64],

$$I(\boldsymbol{r}) = \iint S(\boldsymbol{u}')|o(\boldsymbol{r}) * h(\boldsymbol{r}, \boldsymbol{u}')|^2 d^2\boldsymbol{u}', \tag{5.2}$$

where $S(\boldsymbol{u}')$ is the intensity profile of the incident light in the source plane, and $h(\cdot)$ is the amplitude spread function. The reflected illumination is ignored as in DPC, the object transmission is recovered through the differences between a image pair of opposing half pupils.

To further simplify the model, we assume that the object is weak and thus, the complex transmission function can be further approximated by the first-order Taylor expansion, $o(\boldsymbol{r}) \approx 1 - \mu(\boldsymbol{r}) + i\,\phi(\boldsymbol{r})$. The forward model then simplifies to the real and imaginary parts independently [65, 66],

$$I(\boldsymbol{u}) = H_r(\boldsymbol{u})\mu(\boldsymbol{u}) + i\,H_i(\boldsymbol{u})\phi(\boldsymbol{u}), \tag{5.3}$$

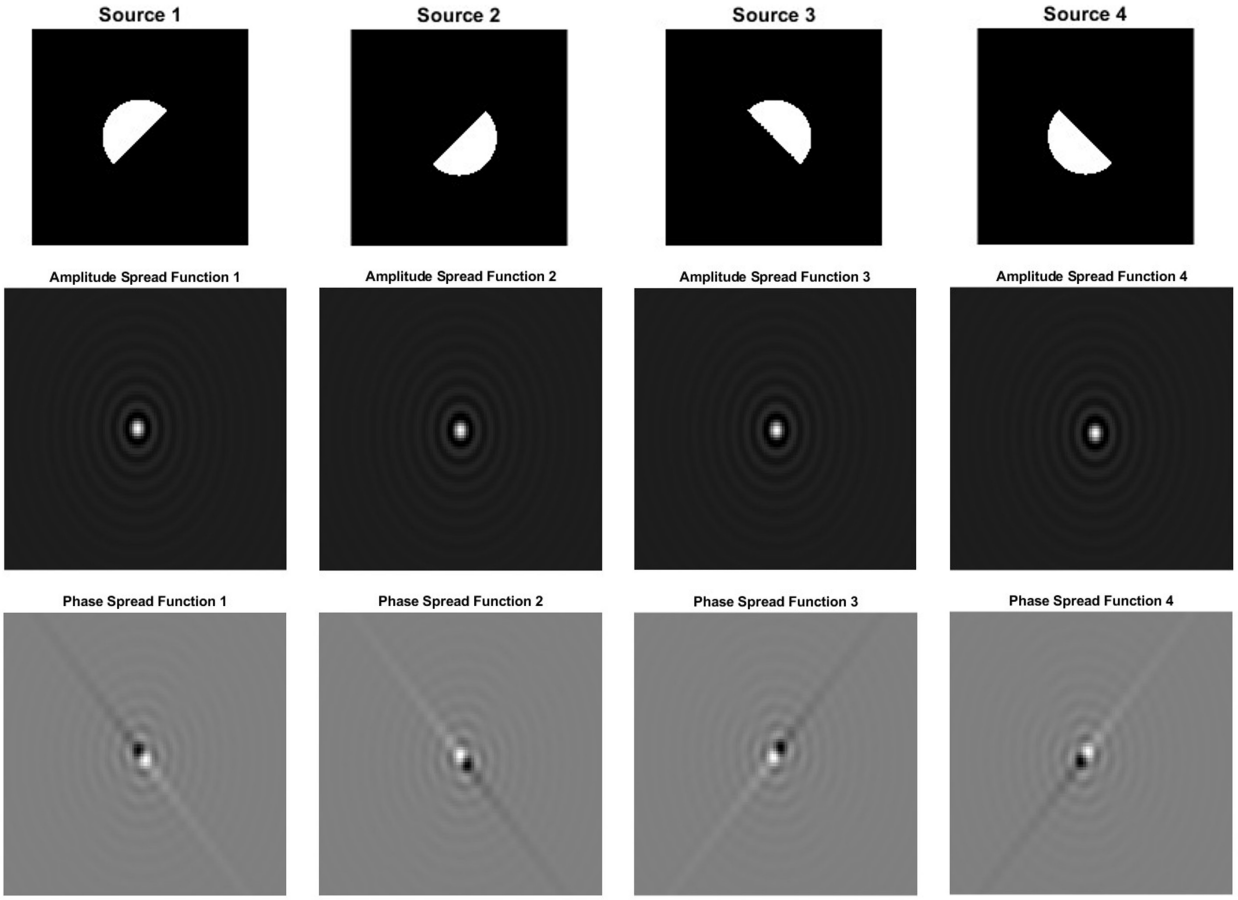

Figure 5.3: Real and imagrinary parts of the CSF that are termed the amplitude spread function and the phase spread function with their corresponding half pupil illuminations.

with

$$H_r = \iint P(\boldsymbol{u}+\boldsymbol{u}')P(\boldsymbol{u}')/\sqrt{\lambda^{-2}-|\boldsymbol{u}+\boldsymbol{u}'|^2}) + P(-\boldsymbol{u}+\boldsymbol{u}')P(\boldsymbol{u}')/\sqrt{\lambda^{-2}-|-\boldsymbol{u}+\boldsymbol{u}'|^2})d^2\boldsymbol{u}', \tag{5.4}$$

and

$$H_i = \iint P(\boldsymbol{u}+\boldsymbol{u}')P(\boldsymbol{u}')/\sqrt{\lambda^{-2}-|\boldsymbol{u}+\boldsymbol{u}'|^2}) - P(-\boldsymbol{u}+\boldsymbol{u}')P(\boldsymbol{u}')/\sqrt{\lambda^{-2}-|-\boldsymbol{u}+\boldsymbol{u}'|^2})d^2\boldsymbol{u}'. \tag{5.5}$$

Their inverse Fourier transform, which is the coherent spread function (CSF), is plotted in Fig. 5.3 to demonstrate how the phase information of the object is encoded into the intensity of the scattered field.

To retrieve the complex transmission of the object, the inverse problem is posed as

$$\{\hat{\mu}(\boldsymbol{r}), \hat{\phi}(\boldsymbol{r})\} = \text{argmin}_{\mu(\boldsymbol{r}),\phi(\boldsymbol{r})} \sum_{n=1}^{4} \|\tilde{I}_n(\boldsymbol{u}) - H_{n,r}(\boldsymbol{u})\mu(\boldsymbol{u}) + i\, H_{n,i}(\boldsymbol{u})\phi(\boldsymbol{u})\}\|_2^2, \tag{5.6}$$

where $\tilde{I}_n(\cdot)$ is subtracted and normalized by its mean. There exists a closed-form solution under Tikhonov regularization, $\|\mu\|_2^2$ and $\|\phi\|_2^2$, which is given by the inverse Fourier transform of their spatial frequency representations [63, 66]

$$\mu(\boldsymbol{u}) = \frac{\left(\sum_{n=1}^{4} \tilde{I}_n(\boldsymbol{u}) \cdot H_{n,r}^*(\boldsymbol{u})\right) \cdot \sum_{n=1}^{4} |H_{n,i}(\boldsymbol{u})|^2 - \left(\sum_{n=1}^{4} \tilde{I}_n(\boldsymbol{u}) \cdot H_{n,i}^*(\boldsymbol{r})\right) \cdot \sum_{n=1}^{4} H_r^*(\boldsymbol{u}) \cdot H_i(\boldsymbol{u})}{\sum_{n=1}^{4} |H_{n,r}(\boldsymbol{u})|^2 \cdot \sum_{n=1}^{4} |H_{n,i}(\boldsymbol{u})|^2 - \left(\sum_{n=1}^{4} H_r^*(\boldsymbol{u}) \cdot H_i(\boldsymbol{u})\right)\left(\sum_{n=1}^{4} H_r(\boldsymbol{u}) \cdot H_i^*(\boldsymbol{u})\right)}, \tag{5.7}$$

and

$$\phi(\boldsymbol{u}) = \frac{\left(\sum_{n=1}^{4} \tilde{I}_n(\boldsymbol{u}) \cdot H_{n,i}^*(\boldsymbol{u})\right) \cdot \sum_{n=1}^{4} |H_{n,r}(\boldsymbol{u})|^2 - \left(\sum_{n=1}^{4} \tilde{I}_n(\boldsymbol{u}) \cdot H_{n,r}^*(\boldsymbol{r})\right) \cdot \sum_{n=1}^{4} H_r(\boldsymbol{u}) \cdot H_i^*(\boldsymbol{u})}{\sum_{n=1}^{4} |H_{n,r}(\boldsymbol{u})|^2 \cdot \sum_{n=1}^{4} |H_{n,i}(\boldsymbol{u})|^2 - \left(\sum_{n=1}^{4} H_r^*(\boldsymbol{u}) \cdot H_i(\boldsymbol{u})\right)\left(\sum_{n=1}^{4} H_r(\boldsymbol{u}) \cdot H_i^*(\boldsymbol{u})\right)}. \tag{5.8}$$

5.3 Preliminary Results and Discussions

To validate the accuracy of phase measurements in QSCAT, especially considering that the modeling is incomplete, we imaged a test object with a known optical path length difference (ΔOPL) : a USAF resolution target with chromium deposited on a glass substrate. Specifically, we acquire four intensity images of the Group 7 elements under illumination using half-pupil masks, as illustrated in Fig. 5.4. The half-pupil images in the case of chromium features should be comparable in intensity.

The reconstructed phase, obtained using the closed-form expressions in Eqs. 5.7 and 5.8, is also shown in in Fig. 5.4. As expected from DPC microscopy under limited photon budget, the recovered phase exhibits notable background noise, a characteristic commonly observed in low-SNR regimes [67]. This noise primarily arises from the amplification of small intensity differences

during gradient computation, as well as imperfections in background normalization. Despite the presence of background fluctuations, the main features of the object are clearly resolved, indicating that the system is capable of capturing phase gradients with sufficient fidelity. Further denoising or regularized phase integration methods may be explored in future work to enhance phase quality without compromising resolution.

The main interest here is to recover the phase so that the OPL differerncec can be converted to the height of the chromium. The retrieved phase map is related to the OPL difference as

$$\Delta \mathrm{OPL} = \frac{\lambda}{2\pi}\phi((\boldsymbol{r}), \tag{5.9}$$

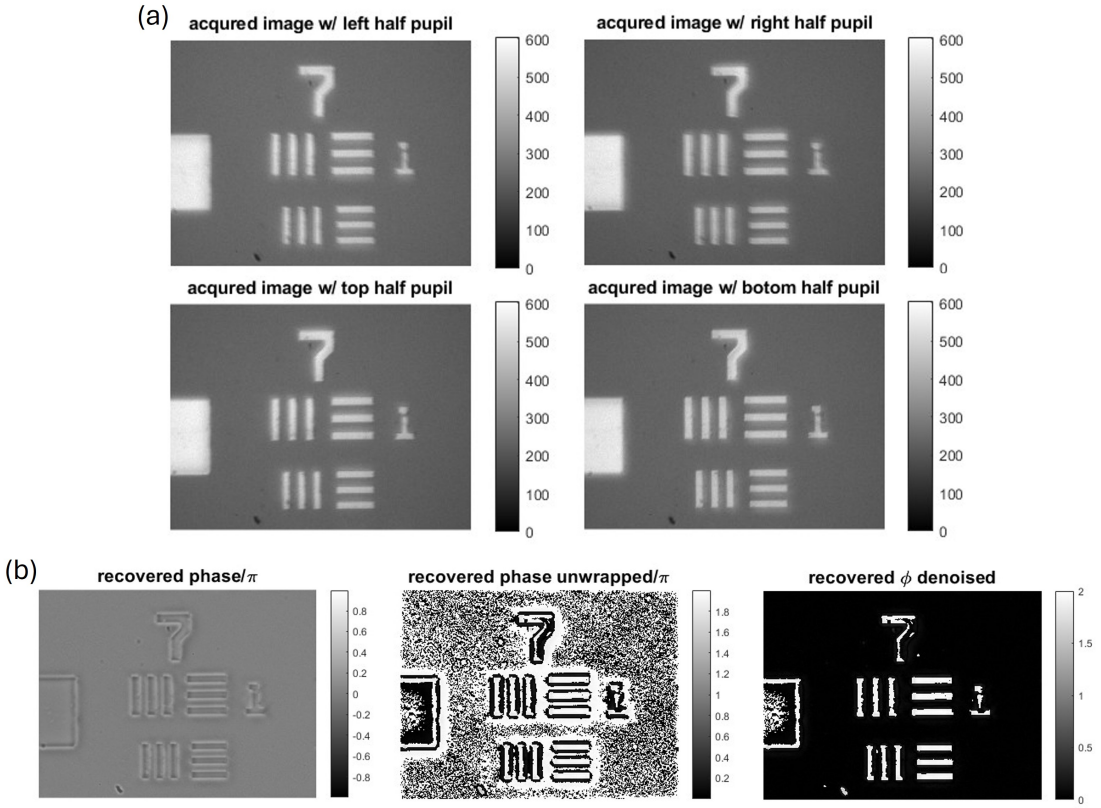

Figure 5.4: (a) Half pupil images of elements in Group 7 in a USAF resolution target. (b) Recovered raw phase unwrapped and then applied with denoising algorithm.

which, for a binary amplitude-phase object like the chromium pattern, corresponds to the physical height difference Δh between the glass substrate and the opaque chromium features through

$$\Delta h = \frac{\Delta \mathrm{OPL}}{n_{\mathrm{Cr}}}, \tag{5.10}$$

where n_{Cr} denotes the refractive indices of chromium. Fig.5.5 displays the extracted height profile of the chromium features recovered from the reconstructed phase map. From this data, we compute the mean and standard deviation of the measured bar heights in both orientations. The horizontal bars exhibit a mean height of 167.47nm with a standard deviation of 3.52nm, while the vertical bars show a mean height of 166.82nm with a standard deviation of 4.60nm. Both measurements are consistent with the nominal fabricated height of 160nm provided by the manufacturer, and the low standard deviations indicate good measurement stability. Notably, the horizontal bars are more fully resolved compared to the vertical ones, suggesting improved optical alignment or calibration along the horizontal axis.

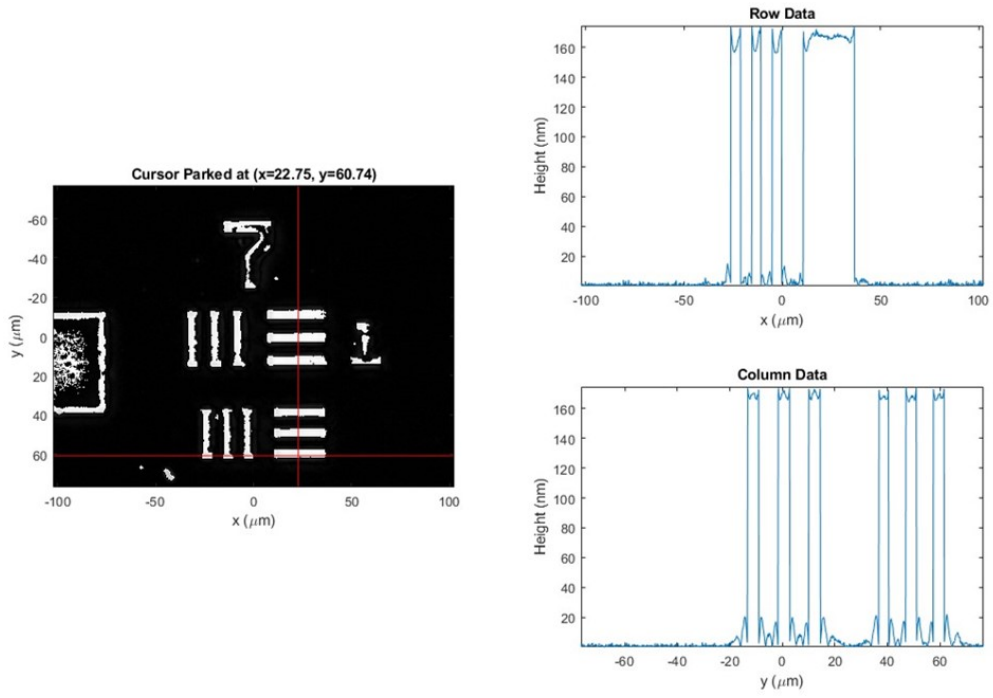

Figure 5.5: Height profiles of chromium features recovered from the reconstructed phase map. Extracted height measurements are shown for elements in Group 7 on a USAF resolution target.

However, in order to estimate the optical susceptibility of the object for future applications, we need to account for both the spatially varying incident field intensity and any residual background phase. Therefore, it is necessary to perform a reference measurement on an empty region of the sample. This reference is then processed using the same phase reconstruction algorithm. The reconstructed complex transmission function of the object is then normalized by the reference, effectively correcting for illumination inhomogeneity and subtracting the background phase offset. The retrieved complex transmission can be used to calculate the estimated optical susceptibility as

$$\alpha_r = \frac{\lambda_0\, n}{\pi} \iint \sqrt{|o(\boldsymbol{r})|}\, \sin\left(k_0\, \angle o(\boldsymbol{r})\right) d^2\boldsymbol{r}, \tag{5.11}$$

$$\alpha_i = \frac{\lambda_0\, n}{\pi} \iint [1 - \sqrt{|o(\boldsymbol{r})|}\, \cos\left(k_0\, \angle o(\boldsymbol{r})\right)] d^2\boldsymbol{r}. \tag{5.12}$$

5.3.1 Neural-Network-based Phase Reconstruction

We implemented a convolutional neural network (CNN) that directly maps raw QSCAT measurements to the object's complex transmission function utilizing the simplified linear scattering model. The network was designed to approximate the inverse scattering operator associated with the QSCAT forward model and was trained to reconstruct both amplitude and phase from the set of four intensity images acquired under half pupil illuminations.

The architecture of the proposed CNN is based on a fully convolutional encoder-decoder structure tailored for DPC data. The network takes as input a four-channel image formed by stacking the difference between and the sum of each pair of QSCAT measurements corresponding to opposite pupil half-illumination patterns. The encoder begins with a 3×3 convolutional layer that expands the input to 32 feature channels, followed by four additional convolutional layers that progressively extract higher-level features. All convolutions use replicate padding to mitigate edge artifacts and are followed by LeakyReLU activations to allow for nonlinear mapping. The decoder consists of a mirrored sequence of convolutional layers that refine and reconstruct the feature maps, culminating in a final convolutional layer that outputs two channels —- corresponding to the real and imaginary parts of the object's complex transmission function. These channels are combined into complex

values to produce the final estimate. To promote stable and effective training, the network weights are initialized using a custom scheme: each convolutional layer is initialized with Xavier normal initialization with gain calculated for linear activations, and biases are set to zero. This design allows the network to approximate the inverse scattering operator efficiently and robustly, enabling direct recovery of both amplitude and phase from QSCAT measurements without requiring explicit inversion of the forward model.

While the network effectively recovers the amplitude of the object's transmission function, reconstructing the phase proves to be significantly more challenging. Amplitude recovery benefits from the direct relationship between the measured intensity patterns and the object's attenuation characteristics, making it relatively robust and stable during training. In contrast, phase recovery is far more sensitive to the choice of learning rate and other optimization hyperparameters, as the phase information is encoded in subtle interference effects that are more difficult for the network to resolve. Despite various training attempts, the network has not consistently converged to the correct phase, suggesting that further architectural refinement, tailored loss functions, or learning rate scheduling strategies may be required. These observations highlight the inherent asymmetry in learning amplitude versus phase in inverse scattering problems, especially under photon-limited and noise-prone measurement conditions like those encountered in QSCAT.

5.4 Future Research

Future work will focus on improving phase accuracy through phase-sensitive loss functions, learning rate scheduling, and optimized network architectures. Incorporating regularization strategies, such as total variation loss or phase continuity priors, and exploring physics-informed or unrolled network designs may also enhance robustness. Additionally, incorporating aberration correction directly into the model architecture and training pipeline could enable the network to compensate for optical distortions. This would improve generalizability and accuracy, particularly in practical settings where experimental imperfections are present.

Chapter 6

Conclusions

This thesis presents a comprehensive study of SPLM with STM illumination, evaluating its theoretical limits, robustness to model mismatch, and practical feasibility through simulation. The work is grounded in the statistical framework of the CRLB, which quantifies the best achievable precision of unbiased estimators under ideal signal models. We derived the CRLB for SPLM with STM illumination with a single emitter, two emitters, and multiple emitters. The analyses demonstrated that, under practical constraints such as photon budget and spatial resolution, SPLM can achieve localization precision on par with conventional camera-based LM techniques, while offering benefits in DOF due to its single-pixel architecture.

To address practical challenges where model mismatch inevitably occurs, such as system misalignment or unmodeled aberrations, we extended the CRLB framework by incorporating the MCRB. The MCRB puts a lower bound on the estimation performance when the assumed model deviates from the true data-generating process, particularly relevant in optics where distortions are often nontrivial. We formulated the MCRB under Poisson statistics and demonstrated its application to both SPLM and SMLM under first- and second-order aberrations. The results show that while CRLB remains optimistic under mismatch, the MCRB provides a more realistic bound on estimator performance and reveals how bias, not just the statistical distance between the assumed and true measurement models, contributes to degradation in precision.

Building on this theoretical foundation, we implemented a complete simulation and inverse problem framework to validate the SPLM system and estimation strategy. Our FISTA-based sparse recovery algorithm, followed by a BFGS refinement step, demonstrates reliable localization of multiple emitters in the presence of aberrations. We showed that uncorrected aberrations significantly degrade estimation accuracy, whereas our aberration correction pipeline effectively restores performance, reducing RMSE and false detection rates. Furthermore, we benchmarked the simulation results against the CRLB to confirm that the proposed algorithm approaches theoretical

precision limits under favorable SNR conditions. These simulations not only validate the feasibility of SPLM but also provide a quantitative basis for system design and calibration strategies.

The second part of this thesis introduces QSCAT, a quantitative phase imaging system implemented via DPC microscopy using a DLP. By relaying arbitrary pupil-plane masks onto the back focal plane of the objective, QSCAT allows flexible control of the illumination, enabling spatial phase gradient measurements. We detailed the experimental setup, calibration procedures, and alignment strategies required to ensure accurate half-pupil projection. Preliminary results on known test targets, such as a chrome Air Force target, demonstrate QSCAT's ability to retrieve phase gradients and reconstruct optical path length differences with micron-scale height sensitivity.

Together, the contributions of this thesis advance both theoretical and practical aspects of optical imaging. The CRLB and MCRB analyses offer rigorous insight into estimation limits under both ideal and mismatched conditions, while the simulation and QSCAT implementations illustrate the translation of these principles into real-world measurement systems. This work lays the foundation for future developments in calibration-aware super-resolution imaging and adaptive structured illumination design.

Bibliography

[1] M. Ranjan Gartia, J. P. Eichorst, R. M. Clegg, and G. Logan Liu. Lifetime imaging of radiative and non-radiative fluorescence decays on nanoplasmonic surface. *Applied Physics Letters*, 101(023118), 2012.

[2] M. Y. Berezin and S. Achilefu. Fluorescence lifetime measurements and biological imaging. *Chem. Rev.*, 110(5):2641–2684, 2010.

[3] R Heintzmannj'O Cremer. Laterally modulated excitation microscopy: Improvement of resolution by using a diffraction grating. *Optical Biopsies and Microscopic Techniques*, page 185, 1999.

[4] M. G. L. Gustafsson. Surpassing the lateral resolution limit by a factor of two using structured illumination microscopy. short communication. *Journal of Microscopy*, 198(2):82–87, 2000.

[5] Eric Betzig, George H. Patterson, Rachid Sougrat, O. Wolf Lindwasser, Scott Olenych, Juan S. Bonifacino, Michael W. Davidson, Jennifer Lippincott-Schwartz, and Harald F. Hess. Imaging intracellular fluorescent proteins at nanometer resolution. *Science*, 313(5793):1642–1645, 2006.

[6] Samuel T. Hess, Thanu P.K. Girirajan, and Michael D. Mason. Ultra-high resolution imaging by fluorescence photoactivation localization microscopy. *Biophysical Journal*, 91(11):4258–4272, 2006.

[7] Michael J Rust, Mark Bates, and Xiaowei Zhuang. Sub-diffraction-limit imaging by stochastic optical reconstruction microscopy (storm). *Nature Methods*, 3(10):793–796, 2006.

[8] Mike Heilemann, Sebastian van de Linde, Mark Schüttpelz, Robert Kasper, Britta Seefeldt, Anindita Mukherjee, Philip Tinnefeld, and Markus Sauer. Subdiffraction-resolution fluorescence imaging with conventional fluorescent probes. *Angew.Chem.Int.Ed.*, 47(33):6172–6176, 2008.

[9] Stefan W. Hell and Jan Wichmann. Breaking the diffraction resolution limit by stimulated emission: stimulated-emission-depletion fluorescence microscopy. *Optics Letters*, 19(11):780, 1994.

[10] Francisco Balzarotti, Yvan Eilers, Klaus C. Gwosch, Arvid H. Gynnå, Volker Westphal, Fernando D. Stefani, Johan Elf, and Stefan W. Hell. Nanometer resolution imaging and tracking of fluorescent molecules with minimal photon fluxes. *Science*, 355(6325):606–612, 2016.

[11] Jeffrey J. Field, David G. Winters, and Randy A. Bartels. Plane wave analysis of coherent holographic image reconstruction by phase transfer (chirpt). *Journal of the Optical Society of America A*, 32(11):2156, 2015.

[12] Jeffrey J. Field, Keith A. Wernsing, Jeff A. Squier, and Randy A. Bartels. Three-dimensional single-pixel imaging of incoherent light with spatiotemporally modulated illumination. *Journal of the Optical Society of America A*, 35(8):1438, 2018.

[13] Jeffrey J. Field, David G. Winters, and Randy A. Bartels. Single-pixel fluorescent imaging with temporally labeled illumination patterns. *Optica*, 3(9):971, 2016.

[14] Maxine Xiu, Jeff Field, Randy Bartels, and Ali Pezeshki. Fisher information and the cramér-rao lower bound in single-pixel localization microscopy with spatiotemporally modulated illumination. *J. Opt. Soc. Am. A*, 40(1):185–203, Jan 2023.

[15] Quang H. Vuong. Cramer-rao bounds for misspecified models. Working Paper 652, Division of the Humanities and Social Sciences, Caltech, October 1986.

[16] Christ D. Richmond and Larry L. Horowitz. Parameter bounds on estimation accuracy under model misspecification. *IEEE Transactions on Signal Processing*, 63(9):2263–2278, 2015.

[17] C. Ren, M. N. El Korso, J. Galy, E. Chaumette, P. Larzabal, and A. Renaux. Performance bounds under misspecification model for mimo radar application. *2015 23rd European Signal Processing Conference (EUSIPCO)*, 2015.

[18] Stefano Fortunati, Fulvio Gini, and Maria S. Greco. The misspecified cramer-rao bound and its application to scatter matrix estimation in complex elliptically symmetric distributions. *IEEE Transactions on Signal Processing*, 64(9):2387–2399, 2016.

[19] Stefano Fortunati, Fulvio Gini, Maria S. Greco, and Christ D. Richmond. Performance bounds for parameter estimation under misspecified models: Fundamental findings and applications. *IEEE Signal Processing Magazine*, 34(6):142–157, 2017.

[20] Stefano Fortunati. Misspecified cramér-rao bounds for complex unconstrained and constrained parameters. *2017 25th European Signal Processing Conference (EUSIPCO)*, 2017.

[21] John D. Dixon. How good is hadamard's inequality for determinants? *Canadian Mathematical Bulletin*, 27(3):260–264, 1984.

[22] Jacques Hadamard. Résolution d'une question relative aux déterminants. *Bull. Sci. Math (2)*, 17:240–246, 1893.

[23] Michał Różański, Roman Wituła, and Edyta Hetmaniok. More subtle versions of the hadamard inequality. *Linear Algebra and its Applications*, 532:500–511, 2017.

[24] J. Mertz. *Introduction to optical microscopy*. Cambridge, MA: Cambridge University Press, 2019.

[25] Jeffery J. Field, Jeff A. Squier, and Randy A. Bartels. Fluorescent coherent diffractive imaging with accelerating light sheets. *Optics Express*, 27(9):13015, 2019.

[26] Patrick A. Stockton, Jeffery J. Field, Jeff A. Squier, Ali Pezeshki, and Randy A. Bartels. Single-pixel fluorescent diffraction tomography. *Optica*, 7(11):1617, 2020.

[27] Patrick Stockton, Gabe Murray, Jeffrey J. Field, Jeff Squier, Ali Pezeshki, and Randy A. Bartels. Tomographic single pixel spatial frequency projection imaging. *Optics Communications*, 520:128401, 2022.

[28] Alyssa M. Allende Motz, John Czerski, Daniel E. Adams, Charles Durfee, Randy Bartels, Jeff Field, Christopher L. Hoy, and Jeff Squier. Two-dimensional random access multiphoton spatial frequency modulated imaging. *Optics Express*, 28(1):405, 2020.

[29] David G. Winters and R. A. Bartels. Two-dimensional single-pixel imaging by cascaded orthogonal line spatial modulation. *Optics Letters*, 40(12):2774, 2015.

[30] U. Kubitscheck. *Fluorescence microscopy: From principles to biological applications*. Wiley-Blackwell, 2013.

[31] B. Huang, W. Wang, M. Bates, and X. Zhuang. Three-dimensional super-resolution imaging by stochastic optical reconstruction microscopy. *Science*, 319(5864):810–813, 2008.

[32] H.P. Kao and A.S. Verkman. Tracking of single fluorescent particles in three dimensions: use of cylindrical optics to encode particle position. *Biophysical Journal*, 67(3):1291–1300, 1994.

[33] Sripad Ram, Prashant Prabhat, E. Sally Ward, and Raimund J. Ober. Improved single particle localization accuracy with dual objective multifocal plane microscopy. *Opt. Express*, 17(8):6881–6898, Apr 2009.

[34] M. F. Juette, T. J. Gould, M. D. Lessard, M. J. Mlodzianoski, B. S. Nagpure, B. T. Bennett, S. T. Hess, and J. Bewersdorf. Three-dimensional sub–100 nm resolution fluorescence microscopy of thick samples. *Nature Methods*, 5(6):527–529, 2008.

[35] Sri Rama Prasanna Pavani and Rafael Piestun. Three dimensional tracking of fluorescent microparticles using a photon-limited double-helix response system. *Opt. Express*, 16(26):22048–22057, Dec 2008.

[36] S. R. Pavani, M. A. Thompson, J. S. Biteen, S. J. Lord, N. Liu, R. J. Twieg, R. Piestun, and W. E. Moerner. Three-dimensional, single-molecule fluorescence imaging beyond the diffraction limit by using a double-helix point spread function. *Proceedings of the National Academy of Sciences*, 106(9):2995–2999, 2009.

[37] Yoav Shechtman, Steffen J. Sahl, Adam S. Backer, and W. E. Moerner. Optimal point spread function design for 3d imaging. *Phys. Rev. Lett.*, 113:133902, Sep 2014.

[38] Yoav Shechtman, Lucien E. Weiss, Adam S. Backer, Steffen J. Sahl, and W. E. Moerner. Precise three-dimensional scan-free multiple-particle tracking over large axial ranges with tetrapod point spread functions. *Nano Letters*, 15(6):4194–4199, 2015. PMID: 25939423.

[39] S. M. Kay. *Fundamentals of Statistical Signal Processing: Estimation Theory*. Upper Saddle River, NJ: Prentice-Hall PTR., 2010.

[40] L.L. Scharf and L.T. McWhorter. Geometry of the cramer-rao bound. In *[1992] IEEE Sixth SP Workshop on Statistical Signal and Array Processing*, pages 5–8, 1992.

[41] Mickaël Lelek, Melina T. Gyparaki, Gerti Beliu, Florian Schueder, Juliette Griffié, Suliana Manley, Ralf Jungmann, Markus Sauer, Melike Lakadamyali, and Christophe Zimmer. Single-molecule localization microscopy. *Nature Reviews Methods Primers*, 1(1), 2021.

[42] A. Tahmasbi, S. Ram, J. Chao, A. V. Abraham, F. W. Tang, E. S. Ward, and R. J. Ober. Designing the focal plane spacing for multifocal plane microscopy. *Optics Express*, 22(14):16706, 2014.

[43] B. Zhang, J. Zerubia, and J.-C. Olivo-Marin. Gaussian approximations of fluorescence microscope point-spread function models. *Applied Optics*, 46(10):1819, 2007.

[44] R. J. Ober, S. Ram, and E. S. Ward. Localization accuracy in single-molecule microscopy. *Biophysical Journal*, 86(2):1185–1200, 2004).

[45] Sripad Ram, Prashant Prabhat, Jerry Chao, E. Sally Ward, and Raimund J. Ober. High accuracy 3d quantum dot tracking with multifocal plane microscopy for the study of fast intracellular dynamics in live cells. *Biophysical Journal*, 95(12):6025–6043, 2008.

[46] J. Chao, E. S. Ward, and R. J. Ober. Fisher information theory for parameter estimation in single molecule microscopy: Tutorial. *Journal of the Optical Society of America A*, 33(7):B36–B57, 2016.

[47] Kim I Mortensen, L Stirling Churchman, James A Spudich, and Henrik Flyvbjerg. Optimized localization analysis for single-molecule tracking and super-resolution microscopy. *Nature methods*, 7(5):377–381, 2010.

[48] Yi Sun. Localization precision of stochastic optical localization nanoscopy using single frames. *Journal of Biomedical Optics*, 18(11):111418, 2013.

[49] Yi Sun and Yue Guan. Effect of unknown emitter intensities on localization accuracy in stochastic optical localization nanoscopy using single frames. *Journal of the Optical Society of America A*, 38(12):1830, 2021.

[50] Phaneendra Yalavarthy, Rajesh Langoju, Brian Pogue, Hamid Dehghani, Abhijit Patil, and Keith Paulsen. Cramer-rao estimation of error limits for diffuse optical tomography with spatial prior information. *SPIE Proceedings*, 2007.

[51] Ling Chen and Nanguang Chen. Optimization of source and detector configurations based on cramer–rao lower bound analysis. *Journal of Biomedical Optics*, 16(3):035001, 2011.

[52] Siavash Yazdanfar, Changhuei Yang, Marinko V. Sarunic, and Joseph A. Izatt. Frequency estimation precision in doppler optical coherence tomography using the cramer-rao lower bound. *Opt. Express*, 13(2):410–416, Jan 2005.

[53] Xukang Wei, H. Paul Urbach, and Wim M. Coene. Cramér-rao lower bound and maximum-likelihood estimation in ptychography with poisson noise. *Physical Review A*, 102(4), 2020.

[54] Lucien M. Le Cam and Jerzy Neyman, editors. *The behavior of maximum likelihood estimates under nonstandard conditions*. Berkley: University of California Press, January 1967.

[55] Halbert White. Maximum likelihood estimation of misspecified models. *Econometrica*, 50(1):1, 1982.

[56] M. S. Kay. *Fundamentals of Statistical Signal Processing. estimation theory*. Prentice-Hall, 1993.

[57] Hongqiang Ma, Rao Fu, Jianquan Xu, and Yang Liu. A simple and cost-effective setup for super-resolution localization microscopy. *Scientific Reports*, 7(1), May 2017.

[58] Aljaž Kavčič, Maja Garvas, Matevž Marinčič, Katrin Unger, Anna Maria Coclite, Boris Majaron, and Matjaž Humar. Deep tissue localization and sensing using optical microcavity probes. *Nature Communications*, 13(1), Mar 2022.

[59] Amir Beck and Marc Teboulle. A fast iterative shrinkage-thresholding algorithm for linear inverse problems. *SIAM Journal on Imaging Sciences*, 2(1):183–202, 2009.

[60] Oliver Lylloff, Efrén Fernández-Grande, Finn Agerkvist, Jørgen Hald, Elisabet Tiana Roig, and Martin S. Andersen. Improving the efficiency of deconvolution algorithms for sound source localization. *The Journal of the Acoustical Society of America*, 138(1):172–180, Jul 2015.

[61] Lucien Le Cam. An approximation theorem for the poisson binomial distribution. *Pacific Journal of Mathematics*, 10(4):1181–1197, Dec 1960.

[62] J. Michael Steele. Le cam's inequality and poisson approximations. *The American Mathematical Monthly*, 101(1):48–54, Jan 1994.

[63] Sébastien M Popoff, Rodrigo Gutiérrez-Cuevas, Yaron Bromberg, and Maxime W Matthés. A practical guide to digital micro-mirror devices (dmds) for wavefront shaping. *Journal of Physics: Photonics*, 6(4):043001, aug 2024.

[64] Max Born, Emil Wolf, A. B. Bhatia, P. C. Clemmow, D. Gabor, A. R. Stokes, A. M. Taylor, P. A. Wayman, and W. L. Wilcock. *Principles of Optics: Electromagnetic Theory of*

Propagation, Interference and Diffraction of Light. Cambridge University Press, 7 edition, 1999.

[65] Lei Tian and Laura Waller. Quantitative differential phase contrast imaging in an led array microscope. *Opt. Express*, 23(9):11394–11403, May 2015.

[66] Michael Chen, Zachary F. Phillips, and Laura Waller. Quantitative differential phase contrast (dpc) microscopy with computational aberration correction. *Opt. Express*, 26(25):32888–32899, Dec 2018.

[67] Patrick C. Chaumet, Pierre Bon, Guillaume Maire, Anne Sentenac, and Guillaume Baffou. Quantitative phase microscopies: Accuracy comparison. *Light: Science & Applications*, 13(1), Oct 2024.

Appendix A

License

Colorado State University LaTeX Thesis Template

by Elliott Forney – 2017

This is free and unencumbered software released into the public domain.

Anyone is free to copy, modify, publish, use, compile, sell, or distribute this software, either in source code form or as a compiled binary, for any purpose, commercial or non-commercial, and by any means.

In jurisdictions that recognize copyright laws, the author or authors of this software dedicate any and all copyright interest in the software to the public domain. We make this dedication for the benefit of the public at large and to the detriment of our heirs and successors. We intend this dedication to be an overt act of relinquishment in perpetuity of all present and future rights to this software under copyright law.

THE SOFTWARE IS PROVIDED "AS IS", WITHOUT WARRANTY OF ANY KIND, EXPRESS OR IMPLIED, INCLUDING BUT NOT LIMITED TO THE WARRANTIES OF MERCHANTABILITY, FITNESS FOR A PARTICULAR PURPOSE AND NONINFRINGEMENT. IN NO EVENT SHALL THE AUTHORS BE LIABLE FOR ANY CLAIM, DAMAGES OR OTHER LIABILITY, WHETHER IN AN ACTION OF CONTRACT, TORT OR OTHERWISE, ARISING FROM, OUT OF OR IN CONNECTION WITH THE SOFTWARE OR THE USE OR OTHER DEALINGS IN THE SOFTWARE.